Non universality and kinetics in soft matter systems : phase separation of proteins and sonication of carbon nanotubes

Citation for published version (APA):
Stegen, J. (2015). *Non universality and kinetics in soft matter systems : phase separation of proteins and sonication of carbon nanotubes*. [Phd Thesis 1 (Research TU/e / Graduation TU/e), Applied Physics and Science Education]. Technische Universiteit Eindhoven.

Document status and date:
Published: 21/05/2015

Document Version:
Publisher’s PDF, also known as Version of Record (includes final page, issue and volume numbers)

Please check the document version of this publication:

• A submitted manuscript is the version of the article upon submission and before peer-review. There can be important differences between the submitted version and the official published version of record. People interested in the research are advised to contact the author for the final version of the publication, or visit the DOI to the publisher's website.
• The final author version and the galley proof are versions of the publication after peer review.
• The final published version features the final layout of the paper including the volume, issue and page numbers.

Link to publication

General rights
Copyright and moral rights for the publications made accessible in the public portal are retained by the authors and/or other copyright owners and it is a condition of accessing publications that users recognise and abide by the legal requirements associated with these rights.

- Users may download and print one copy of any publication from the public portal for the purpose of private study or research.
- You may not further distribute the material or use it for any profit-making activity or commercial gain
- You may freely distribute the URL identifying the publication in the public portal.

If the publication is distributed under the terms of Article 25fa of the Dutch Copyright Act, indicated by the “Taverne” license above, please follow below link for the End User Agreement:

www.tue.nl/taverne

Take down policy
If you believe that this document breaches copyright please contact us at:

openaccess@tue.nl

providing details and we will investigate your claim.

Download date: 16. Nov. 2023

Non universality and kinetics in soft matter systems: phase separation of proteins and sonication of carbon nanotubes

Joris Stegen

Non universality and kinetics in soft matter systems: phase separation of proteins and sonication of carbon nanotubes

Joris Stegen

Druk: GVO drukkers & vormgevers B.V. | Ponsen & Looijen
Omslagontwerp: GVO drukkers & vormgevers B.V. | Ponsen & Looijen

The layout of this thesis is based on the Thesis Template by Alfred de Wijn, which is inspired in part by several other templates. It is distributed under the Creative Commons Attribution-ShareAlike license. `http://creativecommons.org/licenses/by-sa/3.0/`

A catalogue record is available from the Eindhoven University of Technology Library.
ISBN: 978-90-386-3832-4

This work is part of the research programme of the Foundation for Fundamental Research on Matter (FOM), which is part of the Netherlands Organisation for Scientific Research (NWO).

Non universality and kinetics in soft matter systems: phase separation of proteins and sonication of carbon nanotubes

PROEFSCHRIFT

ter verkrijging van de graad van doctor aan de
Technische Universiteit Eindhoven, op gezag van de
rector magnificus, prof.dr.ir. F.P.T. Baaijens, voor een
commissie aangewezen door het College voor
Promoties in het openbaar te verdedigen
op donderdag 21 mei 2015 om 16.00 uur

door

Joris Stegen

geboren te Venray

Dit proefschrift is goedgekeurd door de promotoren en de samenstelling van de promotiecommissie is als volgt:

voorzitter: prof.dr.ir. G.M.W. Kroesen
1e promotor: prof.dr. H.J.H. Clercx
2e promotor: prof.dr.ir. P.P.A.M. van der Schoot
leden: prof. M. Pasquali (Rice University)
prof.dr. R. van Roij (Universiteit Utrecht)
dr. J.D.R. Harting
prof.dr. M.A.J. Michels

Contents

1 Introduction 9
1.1 Statistical Mechanics and Soft Matter 10
1.2 What is a protein? 12
1.3 Protein-Protein interactions 14
1.4 Protein phase behaviour 16
1.5 Kinetic processes in protein dispersions 18
1.6 Carbon nanotubes 20
1.7 Ultrasonic cavitation 22
1.8 Aim and outline of the thesis 23

I Protein polymorphism and protein phase behaviour 25

2 The dimerisation of beta-lactoglobulin 27
2.1 Introduction 28
2.2 Materials and Methods 29
2.3 Two-state analysis of IR spectra 30
2.4 Dimerisation model 33
2.5 Results 36
2.6 Discussion 39

3 Implications of protein polymorphism on protein phase behaviour 43
3.1 introduction 44
3.2 Two-state protein model 46
3.3 A first-order conformational phase transition 48
3.4 Solution model 50
3.5 Phase diagrams for the weak-coupling regime 53
3.6 Phase diagrams for the strong-coupling regime 57
3.7 Discussion 62

4 Self-crowding induced phase separation 65
4.1 Introduction 66
4.2 Free energy model 67

4.3 Stabilization of the native state at high concentrations 69
4.4 Self-crowding induced phase separation 75
4.5 Discussion 79

5 Anomalous kinetic processes in a model two-state protein dispersion 81
5.1 Introduction 82
5.2 Model 83
5.3 Linear stability analysis 84
5.4 Eigenmodes 86
5.5 Phase and stability behaviour in the weak-coupling regime 90
5.6 Phase and stability behaviour in the strong-coupling regime 94
5.7 Discussion 98

II Ultrasonication of carbon nanotubes 101

6 Scission mechanics of carbon nanotubes by analytic theory 103
6.1 Introduction 104
6.2 Bubble dynamics 107
6.3 Fluid-Nanotube interaction 112
6.4 Mechanics for a radially aligned nanotube during bubble collapse . . . 116
6.5 Implications for scission kinetics 120
6.6 Discussion 126

7 Scission mechanics of carbon nanotubes by Brownian dynamics simulations 131
7.1 Introduction 132
7.2 Bubble dynamics & Rayleigh-Plesset equation 133
7.3 Brownian dynamics of a bead-rod chain 136
7.4 Results 137
7.5 Discussion 142

III General discussion 145

8 Discussion 147
8.1 Aim of the thesis 148
8.2 The coupling of conformational in proteins to their phase behaviour . . 148
8.3 Outlook (part I) 152
8.4 The scission and exfoliation of carbon nanotubes under sonication . . 155
8.5 Outlook (part II) 156

Bibliography 159

Summary 165

List of publications 167

Dankwoord 169

Curriculum vitae 171

Chapter 1

Introduction

Summary

This chapter is a first introduction for the non-expert to the topics that are covered in this thesis. A general introduction to the theoretical framework of statistical mechanics and soft matter physics is given. This is followed by an introduction of the two topics to which this theoretical framework is applied, the field of protein physics, and the ultrasonic dispersion of carbon nanotubes. We end this chapter by giving an outline of the work presented in this thesis.

1.1 Statistical Mechanics and Soft Matter

Statistical mechanics[1] deals with large physical systems that are comprised of a large number of interacting degrees of freedom and aims to find statistical averages, laws, that govern the properties of these large and complex systems. A classic example is the behaviour of a macroscopic volume of for example 1 liter of sufficiently dilute gas. Such a system contains of the order of $N = 10^{22}$ atoms, each having atleast 6 degrees of freedom, being the position (x, y, z) and the velocity (v_x, v_y, v_z) of the particle. In principle the value of these $6N$ parameters must be specified to define the microscopic state of this system and the time evolution of the system can be determined by solving $3N$ coupled differential equations. Unfortunately, this is a task beyond the capabilities of any person or computer. Fortunately, the derivation of the laws governing the macroscopic properties of such a system are not beyond the capabilities of statistical mechanics.

By statistical mechanical methods it can be shown that the state of a macroscopic volume of sufficiently dilute gas is fully specified by just 3 parameters, being any three of pressure (p), volume (V), the number of particles (N) and the temperature (T) and that these quantities are related to each other through the ideal gas law,

$$pV = Nk_BT, \tag{1.1}$$

where k_B is the Boltzmann constant, and where we note that this law was derived form empirical observations well before it was derived by statistical mechanical methods. Nonetheless, this law is of interest to us because it teaches us that the macroscopic state and properties of a macroscopic volume of dilute gas must be determined by the statistical average of the behaviour of the individual gas molecules. Furthermore, this law is a universal law that holds for any gas that is sufficiently dilute. This is a consequence of coarse-graining, meaning that atomistic details are unimportant for this system and need not be included in the theory. The power of statistical mechanics is such, that instead of having to specify the value of of the order of 10^{22} parameters, the values of just 3 parameters are sufficient to specify the macroscopic state of the system. Or perhaps more accurately, it is the very nature of systems such as an ideal gas that allows for this greatly simplified statistical description. It is due to the work of, among others, Ludwig Boltzmann, whose famous entropy formula is engraved in his tombstone, see fig. 1.1, and Josiah Willard Gibbs that we are nowadays able to use statistical mechanics to describe these complex systems.

It was Pierre-Gilles de Gennes who received the Nobel prize in physics in 1991 for the application of statistical mechanical methods to study in particular the behaviour of liquid crystals and polymers.[3] Nowadays both topics are part of the field of soft matter research. Soft matter systems[4] are called soft because they are easily deformed, and moreover, because they are susceptible to thermal fluctuations. Examples of soft matter systems include almost all living materials, foams (shaving cream), emulsions (mayonnaise), granular materials (cereals) and liquid crystals (LCD televisions). In nearly all of these systems, interactions between the degrees of freedom and the coupling of these degrees of freedom to an external field have energies associated

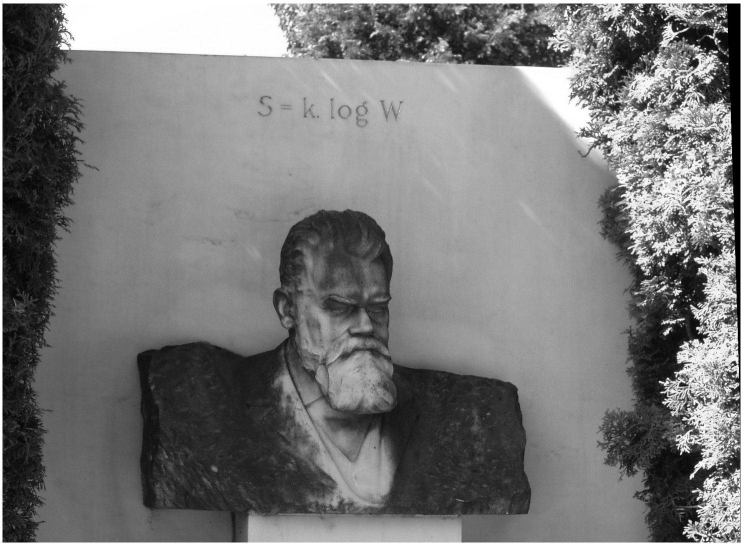

Figure 1.1: The tombstone of Ludwig Boltzmann at the Zentralfriedhof in Vienna. Boltmann's famous entropy formula is engraved in it.[2]

with them that are of the order of thermal energy. As a consequence fluctuations are important and a statistical approach is necessary. The behaviour of these systems is often governed by the temperature-dependent balance between energetic interactions, which typically favour an ordered state, and entropy, which typically favours a disordered state. This gives rise to a temperature-dependent degree of ordering on the microscopic scale, which in turn determines the macroscopic equilibrium properties of the material.

Equilibrium statistical mechanics allows for the determination of the equilibrium properties of the system. These properties are independent of time and of the initial state of the system. Non-equilibrium statistical mechanics allows for the derivation of the manner in which an equilibrium state is reached (or not reached) and is necessarily time dependent. For example, it is possible to calculate how two immiscible fluids phase separate, such calculations show how fast this process is, i.e., what the typical time scale is, and how large the domains of the two coexisting phases are, i.e., what the length scale of this process is.

Ultimately, being able to understand the equilibrium and non-equilibrium properties of soft matter systems is of significant importance from an industrial, social and scientific point of view. Soft matter physics has made important contributions to our understanding of a number of diseases, such as Alzheimer's disease, type 2 diabetes and Parkinson's disease that are related to protein aggregation.[5] Soft matter physics is being used in food physics to develop low fat food products with a similar texture as the non-diet product.[6,7] Other examples include the development of LCD technology, and polymer-carbon nanotube composites[8] that function as a transparent electrode (solar cells, touchscreens).[9,10] Moreover, soft matter physics is nowadays ubiquitously employed to study biological systems,[11] including but certainly not limited to, proteins,[12] neuron functioning, the formation of fibrillar scaffolding within the cell, and stem cell differentiation.[13]

Clearly, soft matter physics is a very broad field of research, and in this thesis two industrially relevant soft matter systems are studied by employing statistical mechanical methods. The non-equilibrium behaviour of both systems is studied and we shall show that this is non-universal for both systems, implying that the observed non-equilibrium behaviour depends strongly on the initial state of the system. In the first system, which is a model protein dispersion, we investigate the kinetics by which relaxation to an equilibrium state occurs after the system has been brought out of equilibrium by a quench, i.e., a sudden change in solution conditions such as the temperature. In the second system, in which carbon nanotubes are exposed to ultrasound, the applied ultrasound drives the system out of equilibrium and we investigate the manner in which the nanotubes undergo scission, when a steady state is reached, and especially what the non-universal kinetic aspects of this process are.

In the following, in section 1.2 an introduction to the role, the production and the properties of proteins in living organisms is given. In section 1.3 an introduction to the different types of interactions between proteins is given and in section 1.4 an introduction to the phase behaviour of a large collection of proteins dispersed in an aqueous solvent is given. In section 1.5 an introduction to the kinetic mechanisms by which phase separation occurs is given. In section 1.6 an introduction to the field of carbon nanotube science is given, and in section 1.7 an introduction to ultrasonic cavitation is given. Finally, in section 1.8 the aim of the work presented in this thesis is introduced and an outline of the remainder of this thesis is given.

1.2 What is a protein?

Proteins[12,14] are large molecules that can be found and are produced by each and every living organism. There are many different proteins, but all of them have some task. Some proteins are responsible for the transport of chemicals in and out of a cell, other proteins form the scaffolding that supports the structure of a cell, other proteins “walk” over these structures to relay signals or transport molecules, there are proteins that are responsible for muscle activity, enzymes are a class of proteins that catalyze chemical reactions and there are proteins that facilitate the construction of other proteins. In summary, proteins are the machinery of life.

Proteins are synthesised in every cell and the building plans for all proteins can be found in the DNA that is present in the cell. A portion of the DNA that encodes for a single protein is called a gene, it consists of a specific sequence of the four different nucleic acids that are linked in the characteristic long polymeric double helical structure. Each cell has the machinery to translate the sequence of nucleic acids that make up a single gene into a protein. It does so by translating each triplet of nucleic

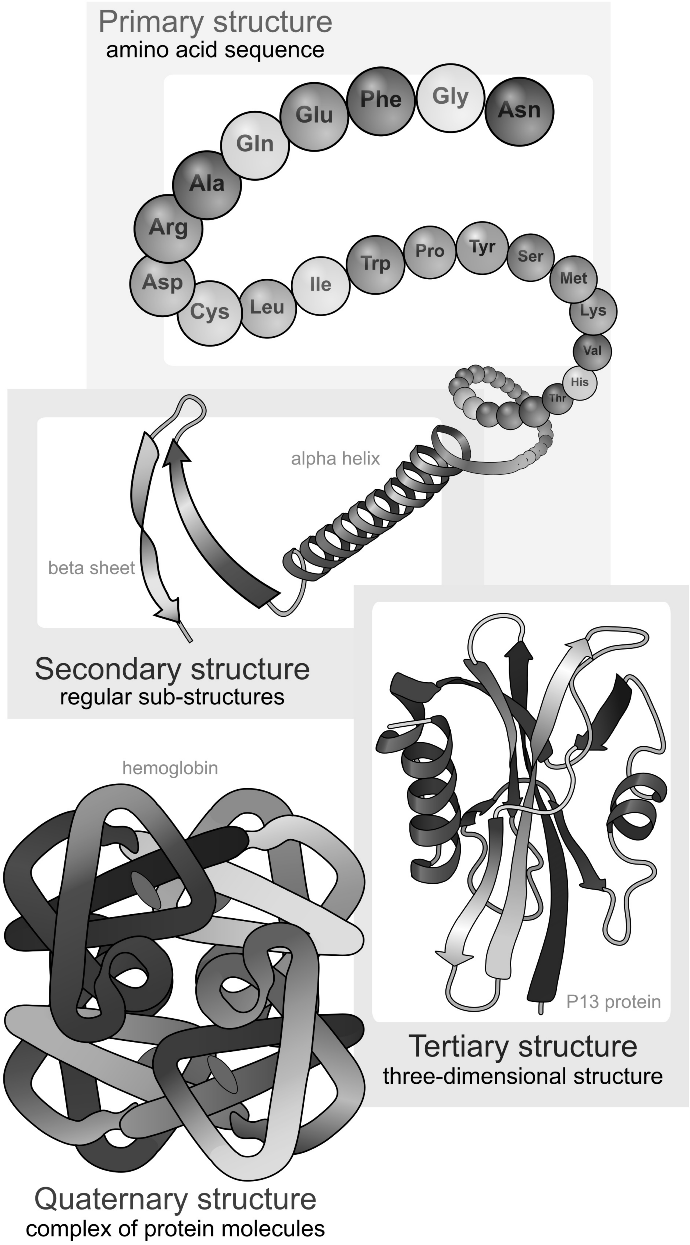
Primary structure
amino acid sequence
Glu
Phe
Gly
Asn
Gln
Ala
Arg
Asp
Cys
Leu
Ile
Trp
Pro
Tyr
Ser
Met
Lys
Val
His
Thr
alpha helix
beta sheet
Secondary structure
regular sub-structures
P13 protein
Tertiary structure
three-dimensional structure
hemoglobin
Quaternary structure
complex of protein molecules

Figure 1.2: An illustration of the four levels of structure in a protein. See the main text for more details.[15]

acids, a codon, to a specific amino acid. All of these amino acids consist of an identical backbone and an amino acid specific residue, of which our DNA encodes for 20 different variants. During the translation of the gene, the backbones of the subsequent amino acids are covalently bonded by peptide bonds and the resulting chain-like polymeric structure forms the primary structure of the protein. It is the specific sequence of amino acids in this chain that specifies the identity of the protein.

This protein specific sequence of amino acids has remarkable properties, for most proteins it specifies a unique three dimensional native conformation of the chain with structure on two additional levels. These levels are the secondary structure of the protein, which results from interactions between different parts of the backbone that gives rise to structural motifs that are found in all proteins, most notably alpha-helical and beta-sheet structure. The tertiary structure of the protein defines in which manner the elements of secondary structure fold into a dense three-dimensional structure. If multiple proteins together form a supramolecular structure, this is known as the quaternary structure of the protein. An overview of these four levels of structure is shown in fig. 1.2.

Interestingly, the native conformation is not at all times the equilibrium conformation of the protein. The native conformation is the equilibrium conformation under the physiological conditions at which the protein has to function. Changes in the local environment, including changes in temperature, pH, or the presence of certain chemical compounds, including large amounts of salt can destabilise the native state and cause a non-native state to become the minimum free energy conformation, which differs in atleast either its secondary, tertiary or quaternary structure from the native conformation.[12] A well known example of this is the amyloid fibrillation of proteins, where after (partial) unfolding, the proteins assemble into a quaternary structure that is rich in beta-sheet structure.[5,16] In chapter 2 we give another example and show that the dimerisation of beta-lactoglobulin leads to changes in the secondary structure of this small water soluble globular protein and in chapters 3, 4 and 5 we study the coupling of conformational changes in proteins to phase separation in a dispersion of these proteins.

In summary, proteins are chain-like molecules that consist of a protein-specific sequence of amino acids. It is the sequence of these amino acids that determines the three-dimensional native structure of the protein and thereby its function. In the next section, the nature of protein-protein interactions are discussed and in section 1.4 the different phases that can be formed in a protein dispersion are discussed.

1.3 Protein-Protein interactions

When a large number of globular water soluble proteins, the type of protein to which the work in this thesis is restricted, are dissolved in an aqueous solvent, the resulting phase behaviour of the protein dispersion is determined by the properties of the single proteins and their interaction with themselves and the solvent. These interactions can be regulated by the addition of salt that sets the ionic strength of the dispersion, and a buffer that sets the pH of the dispersion. Hence, a protein dispersion is characterised by parameters such as its pH, ionic strength, the temperature and the protein concentration. The interactions between the individual proteins are dependent on the values of these parameters. Depending on their values and the protein concentration, the proteins in the dispersion can remain in a single liquid phase, phase separate into two liquid phases of different composition, form a gel state, a crystalline phase or form a variety of supramolecular aggregates. A brief introduction to each of these phases is given in the next section.

All of these phases have a different degree of ordering on the microscopic scale. Changes in the phase of the protein dispersion reflect changes in the interactions between the proteins themselves and the solvent as well as changes in the entropy of the dispersion. The balance between energetic and entropic contributions to the free energy is determined by the temperature, and typically transitions to a different phase can be induced by changes in the temperature. Moreover, different phases typically have different densities, hence changes in the protein concentration can cause a phase transition. Finally, changes in the interactions between the proteins, which include electrostatic interactions, hydrophobic interactions, and excluded-volume interactions, can also cause changes in the phase of the dispersion.

The electrostatic interactions between the proteins are strongly affected by the pH and the ionic strength of the dispersion. The pH of the dispersion determines the probability that ionisable amino acids are charged and hence the pH regulates the total charge on the protein. At an amino acid and protein specific pH equal to the $\mathrm{pK_a}$ the probability that an ionisable group is ionised is 0.5. At a low pH all amino acids that can be positively charged are positively charged and amino acids that can become negatively charged are neutral, however at high pH the opposite holds true.[12] This has two important consequences, firstly the composition of the chemically heterogeneous surface of a protein varies with changes in the pH, which affects the anisotropic, i.e., orientation-dependent, interactions between the proteins. Secondly, the pH of the dispersion regulates the total charge present on a protein and as a consequence the strength of the repulsive electrostatic interactions between them. Indeed, when a protein is highly charged, it repels other proteins due to Coulombic repulsion. However, at the isoelectric point, where the pH equals the so-called pI of the protein, the net charge on the protein equals zero and the Coulombic repulsion between the proteins disappears.

The electrostatic interactions between proteins can be further regulated by manipulation of the ionic strength of the dispersion. When the pH of the solution is far from the isoelectric point and the proteins are highly charged, the Coulombic repulsion between the proteins can be reduced by electrostatic screening if a sufficient amount of salt is added. Hence, in this situation the addition of salt increases the effective strength of the attractive interactions between proteins. An important type of interaction between proteins, which is essentially electrostatic in nature, is the hydrogen bond. In a hydrogen bond, a hydrogen atom which is covalently bonded to an electronegative atom engages in an attractive dipole-dipole interaction with another electronegative atom.

Hydrogen bonding also gives rise to the hydrophobic interaction, which is an effective attractive interaction between non-polar parts of the chemically heterogeneous surface of the protein. This interaction leads to the minimisation of the amount of hydrophobic surface area of the protein that is exposed to the surrounding water molecules. This in turn leads to an increase in the orientational entropy of the water molecules and hence a decrease in the free energy of the dispersion. This is the case because near a hydrophobic, non-polar surface, the orientation of the water molecules must be such that they remain fully hydrogen bonded to the surrounding molecules. However, hydrogen bonding to the non-polar surface is not possible and this restricts the orientational freedom of the water molecules. Hence, non-polar parts of the surface of a protein are hydrophobic.

Excluded-volume interactions are also entropic in nature, and these interactions reflect changes in the amount of free volume in the dispersion that is accessible to proteins. An increase in the free volume leads to an increase in the translational freedom of the proteins and hence in the entropy of the dispersion. At high concentrations, where the free volume is limited due to the large number of proteins present, excluded-volume effects shift the equilibrium state of the dispersion to a state where its free volume is maximised. In other words, these effects promote, for example, the folding of proteins to more compact conformations and the formation of aggregates.[17–19] This is a well known consequence of so-called macromolecular crowding and in chapter 4 we shall see that it can cause liquid-liquid phase separation in a protein dispersion.

In the next section the different phases that are observed in a protein dispersion for different solution conditions are introduced.

1.4 Protein phase behaviour

The proteins in a dispersion can, depending on the solution conditions, form a number of different phases and states. These include, a homogeneous liquid phase, a liquid-liquid phase separated phase, a gel state, or a crystalline phase.[20] Furthermore, proteins can self-assemble into a variety of different supramolecular aggregates. The work presented in this thesis focuses on liquid-liquid phase separation, and in particular on the influence of changes in the conformation of the protein on the conditions under which such phase separation occurs and finally the kinetic mechanism by which a phase separated state is obtained.

A protein dispersion phase separates into two liquid phases of different composition because this decreases the overall free energy of the dispersion. This is the case because there are often multiple conflicting contributions to the free energy that minimise the free energy of the dispersion at different compositions of the dispersion. For example, if the proteins are modeled as attractive hard spheres, the entropy associated with their translational freedom is maximised at low concentrations, where there is a large free volume in the dispersion, while the reduction of free energy due to attractive interactions is maximised at high concentrations where many proteins are engaged in attractive interactions with neighbouring proteins. As a consequence, the protein dispersion will phase separate into two coexisting phases when it has a concentration that is neither low, nor high. These phases are in equilibrium with each other and in one of the phases the protein concentration is low and the entropic contribution to the free energy, which reflects the translational degrees of freedom of the proteins, is optimised, while in the second phase the protein concentration is high and the contribution to the free energy of the attractive interactions is optimised. In chapters 3 and 4 we shall consider under which conditions liquid-liquid phase separation occurs when there is a coupling to changes in the conformation of the proteins. In the models presented in these chapters, the competition between translational freedom and attractive interactions as described in the above is an important factor which underlies phase separation in the model dispersion.

Interestingly, if the solution conditions allow for liquid-liquid phase separation, the fully phase separated state is typically not the thermodynamic equilibrium state of the protein dispersion. For most proteins, phase separation is meta-stable with respect to crystallisation of the proteins and in equilibrium a solid crystalline and a fluid phase of the proteins coexist. This is a consequence of the small length scale, relative to their own size, over which proteins interact,[21,22] and hence it is general property of most proteins. For most proteins of which the structure is known, it has been resolved by x-ray crystallography experiments on protein crystals. Unfortunately it is not straightforward to crystallize proteins and it is presumed that crystallization is nucleated in dense protein clusters formed by phase separation or aggregation.[23] Hence, an understanding of how proteins crystallise is a relevant topic that is of importance for determining the structure of proteins, however this topic is not addressed in this thesis.

Even if liquid-liquid phase separation is not meta-stable with respect to crystallization, it is not guaranteed that the fully phase separated state is reached. If the concentration in one of coexisting phases is high, the phase separation can become kinetically arrested. This results in either a glass-like or gel state of the proteins. The underlying microscopic structure of these gels varies from small spherical aggregates to fibers, formed by the polymerisation of the proteins into these fibers, that form a system spanning networks.[24] The formation of a gel state in protein dispersions is not addressed in this thesis.

Both aggregation and the polymerisation of proteins, for example into amyloid fibrils, are examples of supramolecular assembly of proteins. The precise manner in which proteins self-assemble, presuming that they remain in their native state, depends on the geometric distribution of hydrophobic and hydrophilic areas over their chemically heterogeneous surface. For example, if the protein has two small opposing hydrophobic patches, this will lead to the polymerization of these proteins into a fiber due to the anisotropic interactions between the proteins. With an increase in the number of patches more complex supramolecular assemblies become available. The precise manner in which so-called patchy colloids self-assemble has attracted significant scientific interest and numerous patchy colloid models exist.[25] Self-assembly of proteins in their non-native state is also possible. Of course the formation of amyloid fibrils, in which proteins polymerise through the formation of large amounts of interprotein beta-sheet is a well known example of this.[5,16] In chapter 2 we study the self-assembly of beta-lactoglobulin, which is a small globular protein, into a dimeric state and show that the dimerisation of these proteins induces changes in the secondary structure of this protein.

In summary, the proteins in a dispersion can undergo phase transitions towards a number of different phases depending on protein concentration and solution conditions such as the pH and the ionic strength of the dispersion. In the next section we briefly discuss the manner in which such phase transition occur, specifically we focus on the kinetics by which liquid-liquid phase separation in a protein dispersion occurs.

1.5 Kinetic processes in protein dispersions

The transition from a homogeneous liquid phase to a phase separated phase is inherently a kinetic process that can be characterised by a typical time and length scale. By which kinetic process the phase separation occurs depends on the thermodynamic stability of the dispersion, which is determined by the local geometry of the free energy landscape. When the local free energy landscape is concave,the dispersion is thermodynamically unstable and phase separation proceeds by spinodal decomposition. The dispersion is stable when the local free energy landscape is convex, in this case phase separation must occur by nucleation and growth. In the first case, any fluctuation in the local protein concentration leads to a reduction of the free energy, while the same fluctuations lead to an increase in the free energy in the latter case. Hence, fluctuations in a protein concentration grow spontaneously during spinodal decomposition while these fluctuations are suppressed when phase separation must occur by nucleation and growth.

During the initial stages of spinodal decomposition domains of a well defined size are randomly formed, in these domains differences in the local protein concentration grow exponentially over time at a single characteristic time scale, see fig. 1.3. The length scale at which the demixing occurs is determined by a compromise between two competing effects, 1) the time scale at which very large domains grow is limited by diffusion, and 2) the growth of very small domains is suppressed because it results in an increase in the free energy due to the large amounts of interface that is created. In the later stages of spinodal decomposition the latter effect causes coarsening of the domains, which means that the domains merge and grow in size until finally the system consists of two distinct macroscopic phases that are fully separated from each other.

The mechanism by which phase separation occurs changes when fluctuations no longer decrease the free energy of the system and are suppressed. In this situation phase separation must occur by nucleation and growth. According to classical nucleation theory, a nucleus of a critical size and composition equal to one of the coexisting phases must be formed by spontaneous fluctuations in the nucleation step.

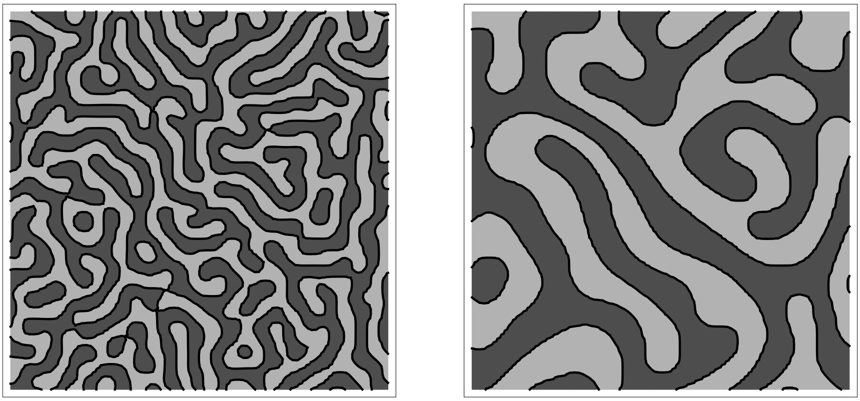

Figure 1.3: The distribution of the two phase of a binary mixture at two different times during spinodal decomposition. The light and dark domains are each rich in one of the two components of the mixture respectively. These figures were obtained following the simulation methods of Rogers et al.[26]

Any nucleus of a smaller size is unstable and disappears while any nucleus larger than the critical size will grow. This critical size again results from two competing effects, 1) the favourable decrease in free energy due to the formation of the coexisting phases, which is a bulk effect and scales with the volume of the nucleus, and 2) the unfavourable increase in free energy due to the formation of an interface between the nucleus and the bulk, which is a surface effect and scales with the surface area of the nucleus.

For a small nucleus the surface effects predominate and a nucleus cannot grow, while for a nucleus larger than the critical radius bulk effects predominate and the nucleus grows spontaneously. The nucleation barrier is then the free energy required to nucleate a nucleus of the critical size, which incidentally corresponds to the size for which nucleation leads to a maximum increase in the free energy barrier. The time scale at which such nucleation occurs is proportional to a Boltzmann factor of this free energy. Hence, the nucleation time grows exponentially with an increasing free energy barrier and can be very large if a significant nucleation barrier is involved. Finally, once a nucleus has been formed it grows spontaneously until the system is fully phase separated. If this growth phase is sufficiently slow relative to the nucleation step, it is possible that multiple nuclii are formed, each of which grow until the system is fully phase separated.

In chapters 3 and 5 we shall see that the concepts of spinodal decomposition and nucleation and growth remain useful even if phase separation is coupled to changes in the conformation of the proteins. However, an important difference with the situation where this coupling is not present, is that the protein diffusion time is no longer the only time scale involved in non-equilibrium processes. A second time scale which represents the time scale at which changes in the conformation of a protein occur enter in the non-equilibrium behaviour. As we shall see in chapters 3 and 5 the ratio of the protein self-diffusion time to the conformational relaxation time of the proteins affects the precise mechanisms by which non-equilibrium processes occur.

1.6 Carbon nanotubes

Carbon nanotubes[27,28] are very thin tubes of carbon atoms, with a diameter varying between approximately a nanometer up to tens of nanometers, and lengths varying from several tens of nanometers up to several centimeter.[29] Carbon nanotubes are essentially a long sheet of graphene, which is a single sheet of carbon atoms, that is rolled into a thin tube, see fig. 1.4. The thinnest nanotubes, which are single-wall carbon nanotubes consist of a single layer of graphene while thicker carbon nanotubes consist of multiple concentrically ordered layers of graphene. The geometric manner in which the graphene sheet is formed into a thin cylinder is denoted by its chirality and the properties of a carbon nanotube are dependent on this.[28]

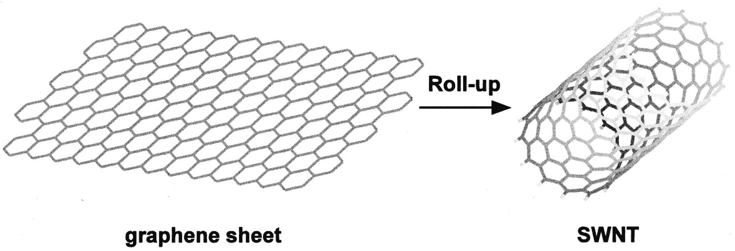

Figure 1.4: An illustration of the structure of graphene and a single wall carbon nanotube. Adapted with permission from “Structure and Electronic Properties of Carbon Nanotubes” by Teri Wang Odom, Jin-Lin Huang, Philip Kim, and Charles M. Lieber, J. Phys. Chem. B, **104**:2794 (2000). Copyright (2000) American Chemical Society.

Aside from carbon nanotubes there are a number of other materials that are entirely build up of carbon atoms, these materials differ in the manner in which the carbon atoms are arranged. In amorphous carbon, carbon atoms are not bonded in a regular lattice. Graphite consists of a large number of graphene layers stacked on top of each other, while a diamond consists of a very large number of carbon atoms that are bonded in a regular three dimensional lattice. An interest in different carbon structures on the nanometer scale was incited by the discovery of the C_{60} buckminsterfullerene molecule, or buckyball, which is a football-shaped molecule that consists of 60 carbon atoms, by Richard Smalley and colleagues in 1985. They were rewarded the Nobel prize in chemistry for this discovery in 1996.[30] This was followed by the discovery of the carbon nanotube in 1991 by Sumio Iijima.[31] Even though carbon nanotubes had been observed previously,[28] it is the work of Ilijima that truly started the field of carbon nanotube science. Finally, graphene, which is a single sheet of carbon atoms, was first famously isolated in 2004 by Andre Geim and Konstantin Novoselov who reduced the thickness of a graphite flake down to a single layer of carbon atoms by repeated splitting of the graphite flake with adhesive tape. They were rewarded the Nobel prize in physics in 2010 for their work on graphene.[32]

The reason that carbon nanotubes have attracted so much scientific interest lies in the fact that they have remarkable properties. Depending on the chirality of the nanotube it is either semiconducting, where the size of the band gap also depends on the chirality, or metallic and highly conductive. Metallic carbon nanotubes can be used to create for example transparent electrodes,[9,10] while semiconducting nanotubes have been used to create a single molecule transistor.[33] The mechanical properties of nanotubes are equally impressive, a tensile strength of 63 GPa has experimentally been observed for multi-wall carbon nanotubes,[34] which makes carbon nanotubes significantly stronger than for example stainless steel and no material matches the specific strength, which is the ratio of strength to weight, of carbon nanotubes. The high tensile strength of carbon nanotubes has been used to create very strong electrically conductive fibers of neatly aligned nanotubes,[35] and polymer-nanotube composites with excellent mechanical properties.[36] Finally, the thermal conductivity of carbon nanotubes is also high.

Unfortunately, the production and development of carbon nanotube-based materials is significantly hindered by the difficulties in processing the nanotubes. Carbon nanotubes are extremely difficult to dissolve and as-produced nanotubes are typically a mixture of nanotubes of different chiralities meaning that a single batch of nanotubes contains both metallic and semiconducting nanotubes. Clearly, the quality of for example nanotube-based transparent electrodes would benefit if only conductive nanotubes are used. While suitable solvents for carbon nanotubes have been found,[37] their poor solubility remains a significant problem. As-produced single-wall carbon nanotubes come in bundles in which the nanotubes are aligned along a common axis and held together by van der Waals interactions. Even though multi-wall nanotubes do not form such bundles, van der Waals interactions between multi-wall nanotubes still lead to the formation of large and insoluble networks of these nanotubes.

The dispersion of nanotubes and the exfoliation of bundles of nanotubes is typically achieved by either of two methods. Carbon nanotubes can be fully dissolved in a superacid such as chlorosulphonic acid, in this acid the surface of the nanotubes becomes protonated and highly charged, the resulting Coulombic repulsion between the nanotubes is stronger than the van der Waals forces keeping the nanotubes in a bundle and they are exfoliated.[37] One problem with this method is that carbon nanotubes dissolved in this manner have so far not been succesfully incorporated in a polymer matrix to produce composite materials because the polymers are often incompatible with the superacid. In this case, dispersion of the carbon nanotubes either by high shear mixing or sonication in an aqueous solvent is preferable.[38] In both processes fluid flows with high shear rates are produced that are sufficiently strong to overcome the van der Waals forces that cause the bundling of the nanotubes. The final stabilisation of the nanotubes in the dispersion is achieved by the addition of a surfactant.[39]

In this thesis we investigate the ultrasonic dispersion of carbon nanotubes and in particular we investigate the manner in which carbon nanotubes undergo scission during this process. The scission of the nanotubes is often unwanted because the quality of carbon nanotube based materials decreases with decreasing length of the nanotubes. In the next section a brief introduction to ultrasonic cavitation, the process responsible for the exfoliation and scission of nanotubes during sonication, is given.

1.7 Ultrasonic cavitation

Ultrasonic cavitation occurs when a sufficiently strong harmonic acoustic field is applied to a liquid.[40] Small bubbles that are present within the liquid interact with the acoustic field: the applied oscillating pressure causes the bubbles to grow and shrink as the pressure in the fluid that surround the bubbles decreases and increases. The precise dynamics by which the bubble responds to the applied acoustic field falls in either of two categories, stable cavitation or transient cavitation. Small bubbles undergo stable cavitation while larger bubbles undergo transient cavitation.

For small bubbles, the surface tension and associated Laplace pressure strongly inhibit the growth of the bubble during the negative pressure peak of the applied acoustic field. As a consequence, these small bubbles undergo small amplitude oscillations in their size. However, because the Laplace pressure varies inversely with the radius of the bubble it fails to contain the growth of sufficiently large bubbles. These bubbles grow explosively during the negative pressure peak of the applied acoustic field and this is the first stage of transient, unstable, cavitation. In chapters 6 and 7 we shall see that the growth of the bubble is indeed explosive. During the ultrasonication of carbon nanotubes, acoustic fields with a typical frequency of 20 kHz are applied, and during 25 μs long negative pressure peak bubbles with an initial radius of 1 μm grow up to a radius of over 700 μm. This corresponds to an incredible increase in the volume of the bubble by a factor of 343×10^6 in just 25 μs, so it is indeed quite an explosive process.

Bubbles that are sufficiently large to undergo transient cavitation are continuously produced by two different processes in the sonication liquid. The coalescence of multiple bubbles can lead to the formation of a bubble that is sufficiently large to undergo transient cavitation. However, this process is suppressed when surfactants are present in the sonication fluid,[41] as is the case during ultrasonication of carbon nanotubes. In this case, the growth of bubbles undergoing stable cavitation occurs primarily by rectified diffusion.[42] In this process the net diffusion of gas molecules dissolved in the liquid into the bubble causes the slow growth of the bubble over many pressure cycles. This process continues until the bubble is sufficiently large and it becomes unstable and transient cavitation is initiated by the explosive growth of the bubble during the negative pressure peak of the applied acoustic field.

In the final stage of transient cavitation, the bubble collapses violently as the applied acoustic pressure is positive and compresses it. During the collapse, the fluid quickly moves in to fill the space previously occupied by the bubble and as the collapse progresses the momentum of the fluid flow increases. At the same time, the decreasing size of the bubble leads to an ever faster decrease in the radius of the bubble to accommodate the inflow of fluid. The energy generated by the collapse of the bubble is focused into an ever smaller volume. As a consequence the final stages of the collapse of the bubble are extremely violent. During this stage the bubbles can produce light in a process known as sonoluminescence and when the collapse of the bubble occurs close to a surface, high speed jets are generated that damage the surface.

It is also during the final stages of the collapse of a transiently cavitating bubble that scission and exfoliation of nanotubes occurs. In this stage, the nanotubes are exposed to fluid flows with extremely high shear rates that generate large forces on the nanotube that are responsible for their scission and exfoliation. In chapters 6 and 7 we investigate the mechanics by which scission occurs.

1.8 Aim and outline of the thesis

The aim of this thesis is to gain an understanding of the non-universal aspects of the equilibrium and the non-equilibrium behaviour of two different soft matter systems. For both of these systems we show that within a highly coarse-grained description, which normally leads to universality in the behaviour of the system, non-universal aspects appear when additional degrees of freedom are included in the theory that are usually neglected. For the first system, a model two-state protein dispersion, we study the coupling of changes in the conformation to the phase behaviour of the proteins and in particular how it affects and leads to non-universality in the conditions and kinetic mechanism by which the transition from a homogeneous to a heterogeneous phase occurs. The second system, is an ultrasonic dispersion system for carbon nanotubes, which is permanently driven out of equilibrium by an applied acoustic field. For this system we investigate the mechanics by which the scission of the nanotubes occurs and in particular what the non-universal aspects of the scission kinetics are.

In chapter 2 we investigate the dimerisation of beta-lactoglobulin, which is a small water soluble protein that is present in cow milk, by interpreting a number of IR spectra measured at different protein concentrations in terms of a two-state protein model. In chapter 3 we present a model two-state protein dispersion in which proteins can reversibly switch between the native and a high-energy non-native conformation and upon transition to the non-native state the proteins can engage in attractive interactions with other proteins in the non-native state. We investigate the phase behaviour of this model dispersion and show that under certain circumstances there is a first-order conformational phase transition that underlies the phase separation of the model dispersion. We show that the phase behaviour is non-universal and argue that the kinetics by which phase separation occur is strongly dependent on the conformation of the proteins and non-universal.

In chapter 4 we extend this model to also include changes in the effective size of the protein upon transition to the non-native conformation. We show that this leads to stabilisation of the native conformation of the protein at high concentrations due to self-crowding effects. These same effects stabilise a homogeneous dispersion of proteins in the non-native state. Furthermore we show that these two phases, at intermediate and high concentrations respectively, are separated by a regime of phase separation with again an underlying first-order conformational phase transition. Finally, in section 5 we perform a linear stability analysis on the model two-state protein dispersion and identify a number of anomalous relaxation modes. Furthermore, we speculate on the precise kinetics by which relaxation to equilibrium occurs under a number of different circumstances.

In chapter 6, we present an analytical model for the scission of carbon nanotubes under tension. In particular we show that the length-dependent motion of the nanotubes during the collapse of the bubble should lead to non-universal scission kinetics that depend on the tensile strength of the nanotube, the sonication conditions and the initial length of the nanotube. In chapter 7, we further investigate the mechanics of nanotube scission by performing Brownian dynamics simulations. These simulations allow for investigation of the effects of bending and buckling of the nanotube. In particular we investigate the competition between scission under tension and scission due to bending and buckling of the nanotube and show that if the nanotube is sufficiently long, it can undergo multiple scissions during the interaction with a single collapsing bubble.

Part I

Protein polymorphism and protein phase behaviour

Chapter 2

The dimerisation of beta-lactoglobulin

Summary

In this chapter we study the dimerisation of beta-lactoglobulin (BLG) type A by fitting a two-state model to a number of IR spectra measured at protein concentrations ranging from 1 mg/ml up to 200 mg/ml. We show that the concentration-dependent degree of dimerisation can be determined from the coherent change in the IR spectrum due to changes in secondary structure of the proteins induced by their dimerisation. This approach allows us to determine the IR spectrum of monomeric BLG and the dimerisation constant, for which we find a value of $K = 193 \pm 15$ M^{-1}. Furthermore, we show that at high concentrations self-crowding effects must be included to account for the concentration-dependent degree of dimerisation.

The contents of this chapter has been submitted for publication as: J. Stegen, J.C. Ioannou, R.H. Tromp, A.M. Donald and P. van der Schoot, Mass-action driven conformational switching of proteins: investigation of beta-lactoglobulin dimerisation by infrared spectroscopy.

2.1 Introduction

In the food industry, there is strong demand for increasing the protein content of both fluid and solid food products. Consequently, within the dairy industry there is a practical interest in understanding the fundamental physical interactions between hydration water molecules and whey proteins, which are widely used as ingredients in foods because of their functional properties, i.e., their emulsification, gelation, thickening, foaming and water-binding capacity.[43, 44] A fundamental problem that the food industry faces in formulating high-protein products, is that the stability and sensory qualities of these products irreversibly deteriorate when the protein content exceeds a certain percentage, the precise value of which depends on the application. Presumably, the process underlying this problem is a mass-action driven stabilisation of a dominant non-native protein conformation that self-associates to form poorly soluble aggregates that lead to the deterioration of the sensory qualities of food products with increasing protein content.

In this chapter we investigate this process by fitting a two-state model to IR spectra of beta-lactoglobulin (BLG) Type A measured at a number of different concentrations. This protein is not only a common ingredient of high-protein foods,[45] but is also the major whey protein of cow and goat's milk.[46] BLG is a widely studied protein; however, most research has either focused on structural transitions of BLG induced by changes in pH,[47] heat treatment,[48, 49] or the effects of ionic shielding with the addition of various salts.[50] Moreover, many previous studies focus on aggregation while aggregation-induced structural changes are ignored. In this chapter we investigate aggregation by the characterisation of the induced structural changes in BLG at a fixed pH of 3, away from the isoelectric point of BLG pI ≈ 5.3,[51] at fixed ionic strength of 1.2 M, and without any heat treatment involved.

As experiments were performed at a fixed pH of 3, we expect a concentration-dependent equilibrium between BLG in the monomeric and dimeric state. Higher levels of aggregation are extremely unlikely, the dimer-octamer equilibrium for BLG (type A) occurs at pH 4.7 and the monomer-dimer equilibrium occurs at pH 2.5.[51, 52] Only around pH 4.7 have larger oligomeric structures been reported to form, enhanced by a decrease in temperature and a decrease in ionic strength.[53] Consequently, this model system allows us to investigate the mass-action driven dimerisation and the corresponding changes in secondary structure. Even though the dimerisation of BLG is not a significant contributor to the deterioration of the sensory quailities of high-protein food products, we believe that our analysis is more widely applicable, including to practically more relevant systems.

In the remainder of this chapter we first discuss sample preparation and details on the performed Attenuated Total Reflectance Fourier Transform InfraRed (ATR FTIR) spectroscopy measurements in section 2.2. In section 2.3 we show that the monomeric IR spectrum of BLG can be determined and subsequently determine the concentration-dependent degree of dimerisation by fitting a linear combination of the IR spectra of monomeric and dimeric BLG to the IR spectra measured at different concentrations. This contrasts with the conventional analysis of ATR FTIR measurements, where certain parts of the spectrum are associated with the presence of different types of secondary structure. In our approach, the coherent change in all types of secondary structure between two different dominant conformations, i.e., the conformation in the monomeric and dimeric state of BLG, is used to quantitatively determine the concentration-dependent equilibrium between these two conformations.

In section 2.4 we present a dimerisation model that accounts for self-crowding effects, i.e., it explicitly takes the decrease of excluded volume upon dimerisation into account, and we fit this to the concentration-dependent degree of dimerisation to determine the dimerisation constant and an effective hard-sphere radius that accounts for electrostatic interactions between the proteins. Furthermore, we show that excluded-volume interactions must be taken into account because the high degree of dimerisation at the highest concentrations for which experiments were performed is underestimated by a model that does not account for these effects. A model that does include self-crowding effects can explain this, for it is well known that crowding shifts the equilibrium of any reaction towards the state with the smallest excluded volume, i.e., for a monomer-dimer equilibrium towards the dimer.[17–19] In section 2.5 we compare the obtained dimerisation constant with values previously reported in literature and show that the obtained effective hard-sphere radius is consistent with theoretical predictions for the value of this parameter. In section 2.6 we summarise our finding and briefly discuss the accuracy of the performed analysis.

2.2 Materials and Methods

In this section we briefly describe the experiments by which the IR spectra of BLG were obtained. These experiments were performed by John Ioannou at the University of Cambridge. Here we give a brief overview of the manner in which these experiments were performed, full details on these experiments have been published.[54] In these experiments, freeze-dried and purified BLG (BLG, Type A) from bovine milk, as produced by NIZO food research bv (Ede, The Netherlands), was dissolved directly in a buffer solution at pH 2.5 in 5 ml vials at varying protein concentration ranging from 1 mg/ml (~ 54 μM) up to 200 mg/ml (~ 0.01 M). A citrate-phosphate buffer (i.e., a McIlvaine buffer) was added such that the protein solutions had a final pH 3. Furthermore, 3 M sodium azide (NaN_3) was added as an anti-bacterial agent.

The average secondary structure of the proteins in solution was characterised by attenuated total reflectance Fourier transform infrared (ATR FTIR) spectroscopy. It is a suitable and well documented technique for testing the secondary structure of many proteins, including BLG, dissolved in H_2O and D_2O buffer solutions.[55] In this work we focus on the amide I region of the spectrum, 1600 - 1700 cm^{-1}, which mainly reflects the C=O stretching vibration of the peptide group, and which consequently gives information on the proteins secondary structure.[56] Unfortunately, due to the detection limits of the instrumentation the lowest protein concentration at which accurate ATR FTIR measurements are possible is ~ 10 mg/ml; however, the benefit of this technique is that there is no upper concentration limit.

Subsequently, the 2nd derivative of the spectra was taken in order to enhance the less obvious differences between the spectra measured at different concentrations. The 2nd derivative of the spectra was buffer-corrected by subtracting out the buffer signal and background noise spectrum and then, presuming proportionality of the spectrum's intensity to the concentration, normalised for protein concentration. A protein concentration-normalised overlay of the 2nd derivative spectra in the amide I region is what is shown in fig. 2.1.

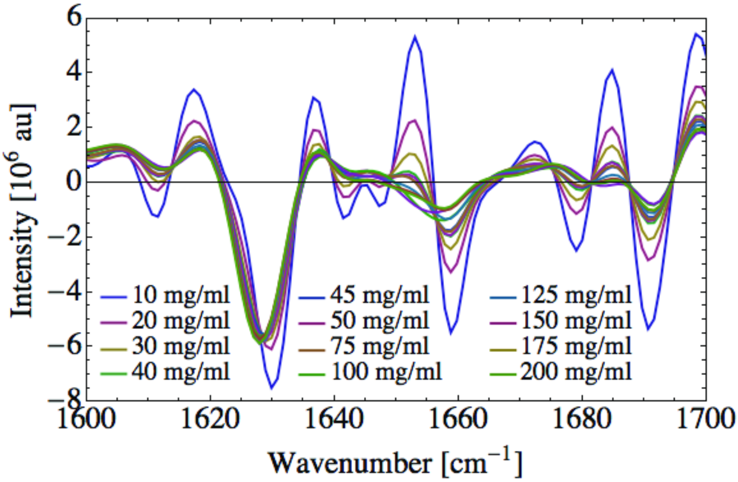

Figure 2.1: The protein concentration-normalised overlay of the 2nd derivative of the ATR FTIR spectra in the amide I region (1600 - 1700 cm^{-1}) for a range of protein solutions of increasing concentrations, buffered at pH 3 in a McIlvaine buffer (0.2 M $\mathrm{Na_2HPO_4}$ and 0.1 M Citric Acid).

In the next section we consider how the coherent change in all types of secondary structure induced by the monomer-dimer transition can be used to determine the concentration-dependent degree of dimerisation from the spectra shown in fig. 2.1. In section 2.5, we show that this approach corresponds well with an approach where changes in a single type of secondary structure are quantified by using the same method as discussed in the next section.

2.3 Two-state analysis of IR spectra

We determine the concentration-dependent degree of dimerisation by fitting a linear combination of the IR spectrum of monomeric and dimeric BLG to the spectra measured at a variety of BLG concentrations. In order to do this, we must first determine what the IR spectra of monomeric and dimeric BLG are. From fig. 2.1 it is clear that for high concentrations the 2nd derivative of the IR spectra converges towards a limiting spectrum, which we presume to be a good approximation of the spectrum of dimeric BLG. Unfortunately, for low concentrations we do not see a similar convergence, suggesting that even at the lowest concentrations for which measurements were performed, the degree of dimerisation must still be significant. Due to detection limits, measurements at concentrations below 10 mg/ml by ATR FTIR are not possible, and we cannot directly determine the spectrum of the BLG monomer from experiment.

Fortunately, the degree of dimerisation (i.e., the number fraction of BLG proteins that have dimerised) at the lowest concentration of 10 mg/ml that we denote as η_0 can readily be determined, and with this, the IR spectrum of monomeric BLG. As we shall see in section 2.4, for low concentrations the degree of dimerisation must increase linearly with concentration, while it must equal zero at a vanishing concentration. The value of η_0 is then that value for which the concentration-dependent degree of dimerisation, which we shall determine from the IR spectra, indeed increases linearly with concentration, while it equals zero at a vanishing concentration.

Given this value of η_0, the spectrum of monomeric BLG can be written as,

$$S_{\mathrm{M}} = \left(S^{10\ \mathrm{mg/ml}} - \eta_0 S_{\mathrm{D}_2}\right) / \left(1 - \eta_0\right), \tag{2.1}$$

where $S^{10\ \mathrm{mg/ml}}$ is the spectrum measured at 10 mg/ml and the spectrum of the BLG dimer equals the spectrum measured at 200 mg/ml, $S_{\mathrm{D}_2} = S^{200\ \mathrm{mg/ml}}$. At any concentration, the degree of dimerisation, η, is then determined by fitting the IR spectrum as measured at that concentration, S, to the following equation,

$$S = \left(1 - \eta\right) S_{\mathrm{M}} + \eta S_{\mathrm{D}_2}. \tag{2.2}$$

In principle, the value of η, as retrieved by fitting the previous equation to a measured IR spectrum, depends on the value of η_0 because S_{M} is a function of η_0. Fortunately, the fitting procedure only has to be performed once because the degree of dimerisation is an analytic function of η_0 and the fitted value of η as determined for, for example $\eta_0 = 0$. This must be so, because eq. (2.2) is a linear combination of $S^{10\ \mathrm{mg/ml}}$ and $S^{200\ \mathrm{mg/ml}}$ regardless of the value of η_0. The fitted value of η then changes in such way with changes in the value of η_0, such that the relative weight of $S^{10\ \mathrm{mg/ml}}$ and $S^{200\ \mathrm{mg/ml}}$ in the fitted spectrum remains identical. From this, it follows that the fitted value of $\eta(\eta_0)$ can be written as a function of η_0 and $\eta(\eta_0 = 0)$, which is the fitted value of η for $\eta_0 = 0$. This function is,

$$\eta\left(\eta_0\right) = \eta_0 + \left(1 - \eta_0\right) \eta\left(\eta_0 = 0\right). \tag{2.3}$$

In section 2.4 we use this equation to determine the value of η_0 for which the resultant concentration-dependent degree of dimerisation increases linearly at low concentrations, while it becomes zero at vanishing concentration. However, let us first consider an example of how eq. (2.2) can be used to determine the concentration-dependent degree of dimerisation.

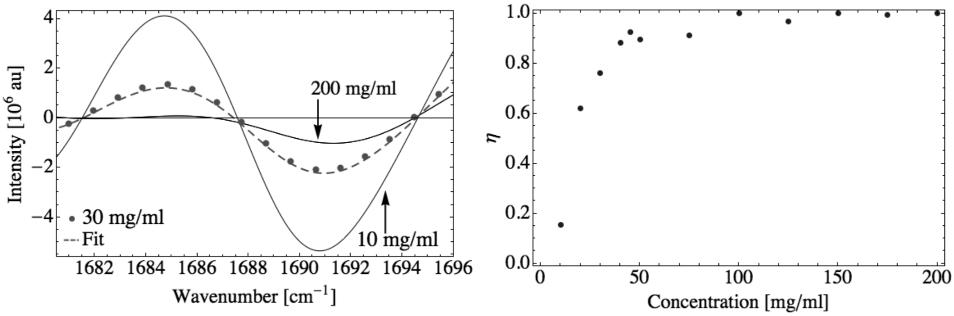

(a) (b)

Figure 2.2: a) The dashed line shows the two-state model fit, eq. (2.2), to the ATR FTIR spectrum measured at 30 mg/ml for wavenumber 1680.5 - 1696 cm^{-1} as shown by the dots. The fit results in $\eta = 0.76$ where $\eta_0 = 0.15$ and the coefficient of determination of this fit is $R^2 = 0.99$. b) For $\eta_0 = 0.15$ the concentration-dependent degree of dimerisation increases linearly at low concentrations and and equals zero at vanishing concentration. The degree of dimerisation at different concentrations is determined by fitting the two-state model, eq. (2.2), to the ATR FTIR spectrum measured at concentrations ranging from 10 - 200 mg/ml for wavenumber 1680.5 - 1696 cm^{-1}.

In fig. 2.2 the result of the fitting procedure is shown, where in fig. 2.2a the degree of dimerisation is determined from the part of the IR spectrum with wavenumber 1680.5 - 1696 cm^{-1} for a dispersion with a concentration of 30 mg/ml. From fig. 2.2a it is clear that the two-state model fitted to the spectrum is good, with a coefficient of determination equal to $R^2 = 0.99$. Note that the quality of this fit is independent of the value of η_0 as it is a fit to a linear combination of the spectra measured at 10 mg/ml and 200 mg/ml regardless of the actual value of η_0. This procedure was repeated for all other concentrations, and the resulting concentration-dependent degree of dimerisation is shown in fig. 2.2b. Of all the data points shown in this figure, the point for 150 mg/ml results from the least accurate fit, with $R^2 = 0.83$. As previously remarked, the value of η_0 must be such that the degree of dimerisation increases linearly from a value of zero at vanishing concentration, and from fig. 2.2b it is clear that this is indeed to good approximation the case for $\eta_0 = 0.15$.

In the example given in the above, we have fitted the two-state model to a small region of the spectrum that includes three isosbestic points. At an isosbestic point, the measured intensity is constant because the specific extinction coefficient of the monomer and dimer are equal. Consequently, the measured intensity at such a point is independent of the degree of dimerisation. The 1680.5 - 1696 cm^{-1} interval of the spectrum was chosen for illustrative purposes and because the fitting procedure works well near isosbestic points. However, the two-state model can also be fitted to different parts of the spectrum. Alternatively, we can use the entire spectrum and thereby determine the degree of dimerisation from the coherent change upon dimerisation in all types of secondary structure. A different approach is to use parts of the spectrum that reflect the presence of different types of secondary structure, and finally we can use other parts of the spectrum that include a number of isosbestic points. We consider these different options in detail in section 2.5, where we repeat the fitting procedure as introduced in this section for other parts of the spectrum and combine the result with a dimerisation model in which self-crowding effects are included to determine the dimerisation constant. We present this dimerisation model in the next section. There, we show how η_0 can be determined as well as the dimerisation constant of BLG.

2.4 Dimerisation model

The reversible dimerisation of BLG is given by the following chemical equation,

$$2\,[\mathrm{M}] \rightleftharpoons [\mathrm{D}_2]\,, \tag{2.4}$$

where $[\mathrm{M}]$ is the molar concentration of monomeric BLG and $[\mathrm{D}_2]$ the molar concentration of dimeric BLG, and where the dimerisation constant reads,

$$K = [\mathrm{D}_2]\,/\,[\mathrm{M}]^2\,. \tag{2.5}$$

If we denote the total molar concentration of BLG molecules as $c = 2[\mathrm{D}_2] + [\mathrm{M}]$ and the fraction of BLG molecules that is part of a dimer, i.e., the degree of dimerisation, as η, then linearisation of eq. (2.5) around $\eta = 0$ yields,

$$\eta = 2Kc. \tag{2.6}$$

This shows, as advertised in the previous section, that for low protein concentrations the degree of dimerisation increases linearly with concentration. Note that this is a general property of mass-action driven dimerisation processes, hence it also holds when self-crowding effects are incorporated in the dimerisation model.

Using eq. (2.6) we can obtain the value of both K and η_0 by fitting it to the linear part of the relation between BLG concentration and the degree of dimerisation (which is a function of η_0), i.e., for concentrations up to 45 mg/ml (fig. 2.2b), as determined from the ATR FTIR measurements using the method described in the previous section. Whilst, in section 2.3 we focused on the 1680.5 - 1696 cm^{-1} part of the spectrum, we now focus on the entire spectrum, i.e., from 1600 to 1700 cm^{-1} as this allows us to determine the degree of dimerisation from the coherent change in the entire IR spectrum resulting from the mass-action driven shift in the monomer-dimer equilibrium. In fig. 2.3, the result of the fitting procedure is shown. For $\eta_0 = 0.151$ and $K = 200$ M^{-1} we find that the degree of dimerisation increases approximately linearly with concentration and is zero at zero concentration.

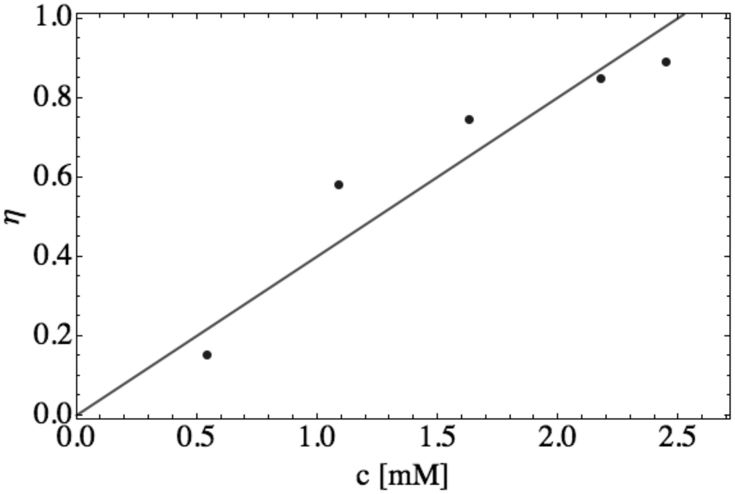

Figure 2.3: The degree of dimerisation as a function of protein concentration for protein concentrations up to 45 mg/ml (points) as determined by fitting the two-state model, eq. (2.2), to the ATR FTIR spectrum for wavenumber 1600 up to 1700 cm^{-1}. Eq. (2.6) has been fitted (line) to these data points by varying η_0 and K, the result is $K = 200$ M^{-1}, $\eta_0 = 0.151$ and the associated coefficient of determination is $R^2 = 0.982$.

Let us now consider how the degree of dimerisation as predicted by eq. (2.6) compares to the degree of dimerisation as determined from the ATR FTIR spectra over the entire concentration range. For this, the full non-linear relation between the degree of dimerisation, η, protein concentration, c, and the dimerisation constant K must be used,

$$\frac{\eta}{(1-\eta)^2} = 2Kc. \tag{2.7}$$

In fig. 2.4 the degree of dimerisation predicted by eq. (2.7) is shown as the dashed line for the previously determined value of $K = 200$ M^{-1}, whereas the degree of dimerisation as determined from the ATR FTIR measurements is indicated by the dots. Furthermore, the degree of dimerisation as predicted by the same equation as obtained from a force fit to the experimentally determined degree of dimerisation at all concentrations ($K = 2953$ M^{-1}) is shown as the dot-dashed line. Clearly, eq. (2.7) underestimates the degree of dimerisation, especially at higher concentrations, even if it is force fitted through all of the data points. A plausible explanation for this is that at high concentrations self-crowding is important. Indeed, at high concentrations the amount of free volume is limited and the decrease in the total excluded volume by the dimerisation of two BLG molecules is favourable. This effect, which is a well-known consequence of crowding, shifts the equilibrium of the dimerisation reaction towards the dimer.[17–19] In the following, we present a dimerisation model that takes these effects into account. That it is indeed well worth to include these effects is shown in fig. 2.4, where the concentration-dependent degree of dimerisation as predicted by the model including self-crowding effects is shown by the solid line. Clearly this is a significant improvement on the model that does not take crowding effects into account.

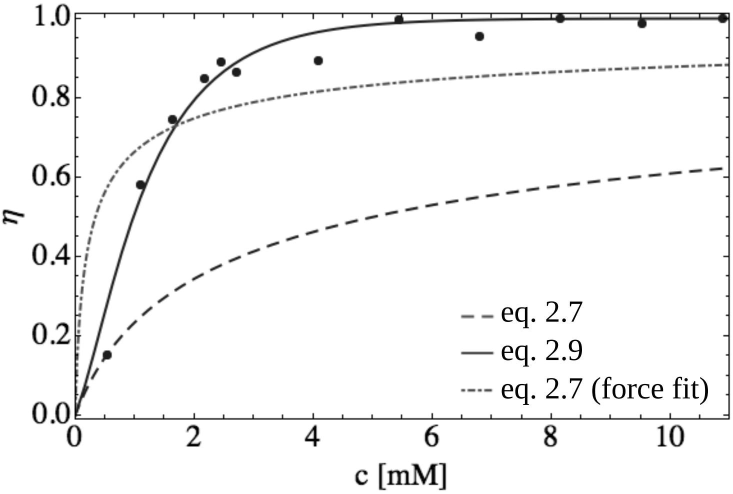

Figure 2.4: The degree of dimerisation as a function of protein concentration for protein concentrations up to 200 mg/ml (points) determined by fitting the two-state model, eq. (2.2), to the ATR-FTIR spectrum for wavenumber 1600 - 1700 cm^{-1}. Eq. (2.6) has been fitted to these data points, giving $\eta_0 = 0.151$ and $K = 200$ M^{-1}. The corresponding degree of dimerisation as predicted by eq. (2.7) is shown by the dashed line. The result of a force fit of this equation to all of the data points, giving $K = 2950$ M^{-1}, is shown by the dot-dashed line. An improved dimerisation model that takes crowding effects into account, given by eq. (2.9), is also fitted (solid line) yielding a ratio of the effective hard-sphere diameter (including electrostatic interactions) and the bare hard-sphere diameter of $\gamma = 3.29$.

Let us now consider how we can set up a dimerisation model that includes excluded-volume interactions. A sensible model free energy should include ideal solution terms accounting for mixing and translation of monomers and dimers, plus a term reflecting that the dimers have a lower free energy than two free monomers because of their binding, and a term that reflects excluded-volume effects. At the level of a second virial approximation, we obtain the following model free energy density,

$$\begin{aligned}\psi = \rho_{\mathrm{M}} \ln \rho_{\mathrm{M}} v_{\mathrm{M}} - \rho_{\mathrm{M}} - \mu\rho_{\mathrm{M}} + \rho_{\mathrm{D}_2} \ln \rho_{\mathrm{D}_2} v_{\mathrm{D}_2} - \rho_{\mathrm{D}_2} - 2\mu\rho_{\mathrm{D}_2} - \\ \epsilon\rho_d + B_{\mathrm{MM}}\rho_{\mathrm{M}}^2 + 2B_{\mathrm{MD}_2}\rho_{\mathrm{M}}\rho_{\mathrm{D}_2} + B_{\mathrm{D}_2\mathrm{D}_2}\rho_{\mathrm{D}_2}^2,\end{aligned} \tag{2.8}$$

where, ψ, is the grand potential per unit of volume and thermal energy ($k_B T$), ρ_M is the number density of BLG in the monomeric form, ρ_{D_2} the number density of dimers, v_M and v_{D_2} are interaction volume scales that we approximate by the volume of a single solvent molecule, ϵ is the dimer binding free energy, μ is the chemical potential of the proteins in solution and B_MM, B_{MD_2}, $B_{\mathrm{D}_2\mathrm{D}_2}$ are the second virial coefficients for monomer-monomer, monomer-dimer and dimer-dimer excluded-volume interactions.

For hard particles, the second virial coefficient equals half the mutually excluded-volume of the two interacting particles. Hence, the values of the second virial coefficients are readily determined if the monomer is modeled as a hard-sphere particle with an effective diameter σ, in which electrostatic interactions and higher order virial terms are tacitly incorporated, and the dimer as a hard spherocylinder with an effective diameter σ and length $L = 2\sigma/3$ (so its effective volume equals twice the effective volume of a monomer). The virial coefficient are then given by $B_\mathrm{MM} = 2\pi\sigma^3/3$, $B_{\mathrm{MD}_2} = \pi\sigma^3$ and $B_{\mathrm{D}_2\mathrm{D}_2} = 13\pi\sigma^3/9$.[57]

Under conditions of thermodynamic equilibrium ρ_M and ρ_{D_2} minimise the free energy density, eq. (2.8). To fix the chemical potential, we insist that the number density of BLG proteins, $\rho_\mathrm{M} + 2\rho_{\mathrm{D}_2}$, is conserved. This gives,

$$\frac{\eta}{(1-\eta)^2} = 2Kc \exp\left[\gamma^3 \left(4\phi - 2\phi\eta/3\right)\right], \tag{2.9}$$

where η is the degree of dimerisation, c the molar concentration of BLG, K the dimerisation constant, $\phi = cM_\beta/\rho_\beta$ the protein volume fraction with M_β the molar mass of BLG and $\rho_\beta = 1440$ mg/ml the mass density of BLG.[58] Finally, $\gamma = \sigma/\sigma_0$ is the ratio of the effective hard-sphere diameter, σ, and the bare hard-sphere diameter σ_0. In fig. 2.4, eq. (2.9) is fitted to the concentration-dependent degree of dimerisation as determined from the ATR FTIR measurements using the previously determined value of $K = 200\ M^{-1}$, yielding a value of $\gamma = 3.29$, meaning that effective diameter of the BLG molecule, that takes electrostatic interactions into account is 3.29 times larger than its bare diameter.

In section 2.5 we repeat the fitting procedure described in this and the previous section for other parts of the ATR FTIR spectrum, including fits for parts of the spectrum that reflect the presence of different types of secondary structure, and show that the coherent change of the entire spectrum caused by a changing degree of dimerisation can indeed be used to model the dimerisation process. Furthermore, we compare the obtained dimerisation constant with values reported in literature and compare the obtained value of γ with a theoretical prediction for this parameter.

2.5 Results

We have repeated the fitting procedure described in sections 2.3 and 2.4 for a number of different parts of the ATR FTIR spectrum. While it seems sensible to use the entire ATR FTIR spectrum to determine the concentration-dependent degree of dimerisation, it is equally valid to focus only on parts of the spectrum. Indeed, if the changes in the IR spectrum are induced by a changing degree of dimerisation, then the changes in different parts of the spectrum all reflect the same changes in the degree of dimerisation. Hence, the results of our method should be independent of the segment of the spectrum that is used in the fitting procedure and by repeating the fitting procedure for different parts of the spectrum one can assess the accuracy of the method.

We have determined the concentration-dependent degree of dimerisation and the corresponding values of η_0, K and γ for parts of the IR spectrum around isosbestic points in the wavenumber intervals 1613.5 - 1639 cm^{-1}, 1649 - 1668 cm^{-1} and 1675 - 1700 cm^{-1}, as well as around a number of specific wavenumbers that reflect the presence of different types of secondary structure.[59] Specifically, the parts of the spectrum around 1627 cm^{-1} and 1684 cm^{-1} (anti-parallel beta-sheet),[59] 1666 cm^{-1} (beta-turn),[56,59,60] 1653 cm^{-1} (random coil)[56,59,60] and 1658 cm^{-1} (alpha-helix)[56,59,60] have been used. For each of these wavenumbers, the degree of dimerisation was determined for a 10 cm^{-1} interval surrounding each of these wavenumbers. Detailed information on each of these fits can be found in table 1, in which the fitted values of η, eq. (2.2), to the ATR FTIR spectra are listed, and in table 2 where details of the fit of eqs. (2.6) and (2.9) are listed. Both tables can be found at the end of this chapter. Here, we only present the average values.

For η_0, the degree of dimerisation at a BLG concentration of 10 mg/ml, we find an average value of $\eta_0 = 0.15 \pm 0.01$, which was obtained by fitting eq. (2.6) to the concentration-dependent degree of dimerisation for concentrations upto 45 mg/ml while varying both η_0 and K for all the different wavenumber intervals as listed in the above. While we approximated the ATR FTIR spectrum of the BLG dimer as the spectrum measured at 200 mg/ml, the spectrum of monomeric BLG has so far remained undetermined. However, using the obtained value $\eta_0 = 0.15$ and $S_\mathrm{M} = \left(S^{10\ \mathrm{mg/ml}} - \eta_0 S^{200\ \mathrm{mg/ml}}\right) / (1 - \eta_0)$ (derived in section 2.3), the monomeric spectrum is now determined. In fig. 2.5 both the concentration-normalised second derivative of the ATR FTIR spectrum of momomeric (solid line) and dimeric (dashed line) of BLG are shown.

In determining the value of η_0, the dimerisation constant, K as defined by eq. (2.5), was also determined. For this parameter we find an average value of $K = 193 \pm 15\ M^{-1}$. Unfortunately, it is difficult to compare this value with previously reported values because the dimerisation constant is extremely sensitive to the ionic strength of the solution and the specific type of salt that is added.[61] Under otherwise identical experimental conditions the dimerisation constant increases by more than a factor 10^3 when 20 mM NaCl is replaced by 20 mM NaClO$_4$, while a 10-fold increase in the concentration of NaCl leads to an increase in the dimerisation constant by a factor 100.[61] Moreover, the results obtained by different experimental methods differ by almost a factor 3.[51]

Whilst a direct comparison with other experiments is difficult unless the experimental conditions are identical, we can attempt a comparison with the result of an experiment that was performed under *similar* experimental conditions. Goto et al. found a dimerisation constant of $K = 1.79 \pm 0.36 \cdot 10^5$ M^{-1} by performing sedimen-

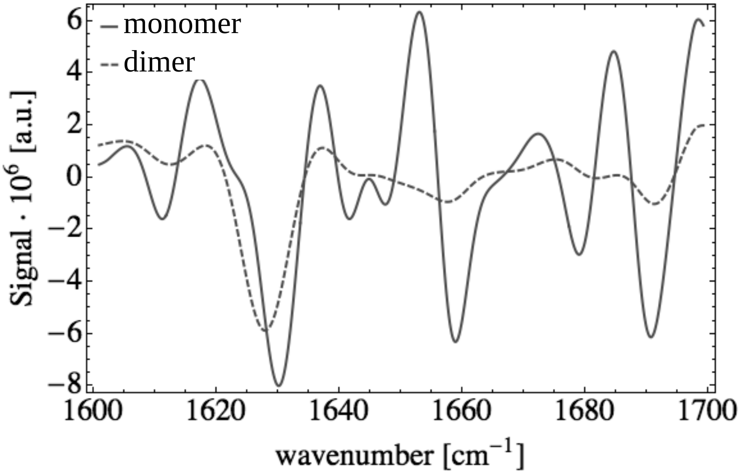

Figure 2.5: The 2nd derivative of the ATR FTIR spectra in the amide I region (1600 - 1700 cm^{-1}) of monomeric BLG (solid line) and dimeric BLG (dashed line).

tation equilibrium experiments over a concentration range of 0.1 - 2 mg/ml at fixed pH of 3 and with 1 M of NaCl added.[61] Their dimerisation constant is a factor 10^3 larger than ours, which is determined at a BLG concentrations range 10 - 45 mg/ml, at fixed pH of 3, with 0.2 M Na_2HPO_4 and 0.1 M citric acid added. While it seems difficult to reconcile this large discrepancy, it is in fact of the same order as the difference in the dimerisation constant that Goto et al. observed upon switching from NaCl to $NaClO_4$. Moreover, there are a number of reasons that make this difference in dimerisation constant between the two experiments consistent.

BLG dimer formation relies on a subtle balance of hydrophobic interactions at the interface of the two BLG molecules that form the dimer, the formation of 12 inter-protein hydrogen bonds, and the electrostatic screening of the charges present on the dimer interface by anion binding.[61] Considering this, as well as the differences between the two experiments we compare, we can rationalise the difference in the reported dimerisation constant. Our experiments are performed at BLG concentrations at least an order of magnitude larger, and in contrast to the experiment of Goto et al., the anions present are multivalent. Moreover, the $C_6H_5O_7^{-3}$ anions of citric acid are significantly larger than the Cl^- anion, and it is likely that it is simply too large to screen charges on the interface of the dimer, whilst leaving the inter-protein hydrogen bonds and hydrophobic interaction between the two BLG molecules intact. This suggests that the number of anions capable of stabilising the BLG dimer, per BLG molecule is actually significantly smaller in our experiment than in the experiment of Goto et al., suggesting that we should indeed find a smaller dimerisation constant.

In this context, it is important to realise that the dimerisation constant is in fact a very sensitive parameter, as it varies exponentially with changes in the dimer binding free energy. The model free energy, eq. (2.8), includes a term proportional to the dimer binding free energy, which is defined as ϵ (in units k_BT). In eq. (2.9), which is derived from this free energy, this parameter is included in the dimerisation constant, K, and $\epsilon = \ln(K\,[\mathrm{H_2O}])$, where $[\mathrm{H_2O}] = 55.5$ M the molar concentration of water. From the fits to the various parts of the ATR FTIR spectrum, we retrieve an average dimer binding free energy of $\epsilon = 9.28 \pm 0.08\ k_BT$. This energy is of the order of thermal energy, as one would indeed expect for a reversible dimerisation process. Moreover, this value differs less than a factor two from the dimer binding free energy of $\epsilon = 16.1\ k_BT$, which corresponds to $K = 1.79 \cdot 10^5$ as measured by Goto et al..[61]

Finally, for the γ we find an average value of $\gamma = 3.2 \pm 0.2$, which suggests that the effective hard-sphere radius, which includes electrostatic interactions, equals approximately 3.2 times the bare hard-sphere radius. The bare hard-sphere radius of BLG is approximately 1.7 nm, suggesting that the electrostatic interactions extent approximately 3.7 nm beyond the hard-sphere surface. Whether this is a reasonable parameter value can be checked, as within a Debye-Huckel approximation an analytic expression for γ for charged interacting hard-spheres in an electrolyte can be derived,[62]

$$\gamma = \left[1 + q^2 \frac{3\lambda_B\lambda_D^2}{2\sigma^3} \frac{1+\sigma/\lambda_D}{(1+\sigma/2\lambda_D)^2}\right]^{1/3}, \tag{2.10}$$

where $\sigma = 1.7$ nm, the bare hard-sphere radius of BLG, $\lambda_B = 0.7$ nm, the Bjerrum length in water at room temperature, $\lambda_D = 0.28$ nm the Debye length in the solution and $q = 16.8$ the number of charges present on the BLG monomer. We obtain $q = 16.8$, by presuming a linear increase in charge from $q = 0$ at the isoelectric point of BLG, pI 5.3 and $q = 20$ at pH 2.5.[61] Given these values, eq. (2.10) yields $\gamma = 1.43$, this differs by about a factor 2 from the experimentally determined value of $\gamma = 3.2 \pm 0.2$. Given that eq. (2.10) is a linear approximation for the electrostatic contribution to the second virial coefficient, the difference between the two values of γ we obtain is insignificant. Furthermore, we expect that the theoretically determined value of γ is smaller because the experimentally determined value also incorporates the effects of higher order virial coefficients.

2.6 Discussion

We have shown that a mass-action driven change in the conformation of BLG due to an increasing degree of dimerisation can be quantified through ATR FTIR measurements at different protein concentrations. In contrast to the conventional analysis of ATR FTIR spectra, where different parts of the spectrum are associated with different types of secondary structure, we showed that the coherent change in the entire IR spectrum with increasing protein concentration can be used to determine the relative abundance of two different protein conformations. This approach has two important advantages, firstly, while the ATR FTIR spectrum of monomeric BLG at pH 3 cannot be measured directly, we showed that the presented method does allow for its determination. Secondly, it allows for the determination of the concentration-dependent degree of dimerisation.

Because we performed experiments up to BLG concentrations of 200 mg/ml, we were able to show that at these concentrations self-crowding effects are important, see fig. 2.4, where the predictions of a dimerisation model including and excluding excluded volume interactions is shown. At these high concentrations, the amount of free volume is limited and the decrease in the total excluded volume caused by dimer formation leads to a decrease in free energy, hence self-crowding leads to an increased degree of dimerisation at high concentrations. Of course it has been recognised for a while that crowding effects can significantly influence the behaviour of proteins at high concentrations, our results reemphasise the importance of crowding-effects.

An important question that remains in regard to this method, is how well it works. In the previous section average values of η_0, K and γ were determined by fitting the two-state model, as introduced in section 2.3, to different parts of the ATR FTIR spectrum. The average values for these parameters seem accurate, the standard deviation in these parameters is less then 10% of their value. Importantly, the result obtained by fitting to the entire ATR FTIR spectrum, 1600 -1700 cm^{-1} are in agreement with these average values. This means that it is indeed valid to quantify the degree of dimerisation by considering the coherent change in the entire IR spectrum induced by changes in the degree of dimerisation.

A second approach to gauge the accuracy of the methodology we presented is to consider the quality of the individual fits that have been made. In table 2.1 and 2.2, the coefficient of determination for the fits made to eqs. (2.2), (2.6) and (2.9) are listed. Although there are some exceptions, the coefficient of determination is generally larger than 0.9, suggesting that these fits are reasonably good. Finally, and most importantly, the results of the analysis we presented are reasonable and self-consistent within the presumptions that were made. In section 2.5 we showed that the value of $\gamma = 3.2 \pm 0.2$, which is the ratio of the effective hard-sphere radius, including electrostatic interactions, to the bare hard-sphere radius, is of the same order of magnitude as a theoretical prediction for its value. Although the value of the dimerisation constant that we find, $K = 193 \pm 15$ M^{-1}, differs significantly from the value obtained for a *similar* experiment, it actually only corresponds to a difference in the binding free energy of less than a factor of two.

In conclusion, we present a new method to analyse the results of ATR FTIR measurements on protein dispersions. We believe that the method is suitable for the characterisation of the equilibrium constant of processes that involve changes in protein conformation. An advantage of our method is that it allows for determination of the IR spectra of the dominant protein conformations involved in such processes, allowing for insight in the structure of the protein in these different conformations.

In the next three chapters we investigate the consequences of the coupling of changes in the conformation of proteins to their phase behaviour and specifically focus on how this affects the conditions under which liquid-liquid phase separation occurs. To this end we shall present a two-state model for the proteins in which the proteins can reversibly switch between two different conformations. The results presented in this chapter clearly support the use of the two-state protein model, for we have shown that such a two-state model is very applicable to the results of experiments on BLG proteins.

We would like to thank John Ioannou for performing the ATR FTIR spectroscopy measurements on the beta-lactoglobulin dispersion. Furthermore, we thank Athene Donald and Hans Tromp for discussions.

concentration [mg/ml]		10	20	30	40	45	50	75	100	125	150	175	200
1600-1700 cm^{-1}	η	0	0.51	0.70	0.82	0.87	0.84	0.87	1	0.95	1	0.98	1
	R^2	1	0.997	0.991	0.981	0.972	0.967	0.978	0.908	0.990	0.831	0.998	1
1613.5-1639 cm^{-1}	η	0	0.46	0.67	0.76	0.80	0.78	0.86	0.94	0.93	0.98	0.98	1
	R^2	1	0.994	0.989	0.984	0.982	0.987	0.996	0.992	0.999	0.998	0.999	1
1649-1668 cm^{-1}	η	0	0.49	0.70	0.82	0.86	0.84	0.86	0.99	0.94	1	0.98	1
	R^2	1	0.988	0.960	0.904	0.879	0.889	0.870	0.734	0.914	0.860	0.995	1
1675-1700 cm^{-1}	η	0	0.54	0.71	0.85	0.90	0.87	0.89	1	0.96	1	0.99	1
	R^2	1	0.996	0.993	0.990	0.985	0.986	0.990	0.979	0.997	0.968	0.999	1
1622-1632 cm^{-1}	η	0	0.42	0.60	0.69	0.73	0.72	0.84	0.91	0.91	0.96	0.97	1
	R^2	1	0.982	0.986	0.981	0.975	0.992	0.995	0.989	0.999	0.999	0.995	1
1648-1658 cm^{-1}	η	0	0.51	0.73	0.85	0.89	0.87	0.89	1	0.96	1	0.99	1
	R^2	1	0.977	0.934	0.869	0.823	0.856	0.817	0.658	0.880	0.664	0.993	1
1653-1663 cm^{-1}	η	0	0.51	0.70	0.82	0.87	0.83	0.86	0.98	0.94	1	0.98	1
	R^2	1	0.989	0.949	0.817	0.721	0.768	0.698	-0.524	0.719	0.444	0.987	1
1661-1671 cm^{-1}	η	0	0.41	0.54	0.65	0.72	0.67	0.71	0.81	0.85	0.94	0.96	1
	R^2	1	0.995	0.978	0.948	0.960	0.954	0.926	0.907	0.955	0.957	0.996	1
1679-1689 cm^{-1}	η	0	0.52	0.69	0.83	0.88	0.84	0.87	1	0.95	1	0.98	1
	R^2	1	0.998	0.993	0.971	0.940	0.962	0.967	0.814	0.972	0.625	0.994	1
Average	η	0	0.49 ± 0.05	0.67 ± 0.06	0.79 ± 0.07	0.84 ± 0.07	0.81 ± 0.07	0.85 ± 0.05	0.96 ± 0.06	0.93 ± 0.03	0.99 ± 0.02	0.98 ± 0.01	1
	R^2	1	0.99 ± 0.01	0.98 ± 0.02	0.94 ± 0.06	0.92 ± 0.09	0.93 ± 0.07	0.92 ± 0.10	0.72 ± 0.48	0.94 ± 0.09	0.82 ± 0.20	0.99 ± 0.01	1

Table 2.1: Details of the two-state model fit to a number of different parts of the measured ATR FTIR spectra. All values listed are obtained whilst presuming $\eta_0 = 0$.

wavenumber [cm^{-1}]	1600-1700	1613.5 - 1639	1649 - 1668	1675 - 1700	1622-1632	1648 - 1658	1653 - 1663	1661 - 1671	1679 -1689
$R^2_{\text{ATR-FTIR}}$	0.96 ± 0.05	0.992 ± 0.006	0.90 ± 0.08	0.988 ± 0.009	0.989 ± 0.008	0.85 ± 0.11	0.62 ± 0.46	0.96 ± 0.03	0.92 ± 0.12
η_0	0.151	0.144	0.151	0.154	0.131	0.156	0.151	0.124	0.151
K [M^{-1}]	200	188	199	206	173	206	200	166	201
ϵ [$k_B T$]	9.32	9.25	9.31	9.35	9.17	9.35	9.32	9.13	9.32
R^2_{lin}	0.982	0.981	0.982	0.982	0.982	0.983	0.981	0.984	0.983
γ	3.29	3.11	3.27	3.37	2.91	3.36	3.28	2.71	3.30
R^2_{full}	0.93	0.92	0.93	0.93	0.91	0.93	0.93	0.90	0.93

Table 2.2: Details of the fits of eq. (2.6) and eq. (2.9), to the degree of dimerisation as determined from different parts of the IR spectrum using eq. (2.2). Values of the fit-parameters are given and the quality of the fits is indicated by the coefficient of determination.

Chapter 3

Implications of protein polymorphism on protein phase behaviour

Summary

In this chapter we investigate the phase behaviour of small globular proteins and in particular the coupling of changes in their conformation to liquid-liquid phase separation. We present a simple two-state model in which protein conformation is not conserved and where the high-energy, non-native state is stabilised by attractive interactions. The resulting phase behaviour is remarkably complex, non-universal and exhibits re-entrance. The model calculations show a demarcation between a regime where conformational transitioning is largely enslaved by phase separation and one where this is not the case.

The contents of this chapter has been published as:
J. Stegen and P. van der Schoot, Soft Matter **11**, 2036 (2015).

3.1 introduction

A large body of work, theoretical and experimental, has been devoted to studying the phase behaviour of globular proteins, reflecting the complexity and relevance of the subject. An understanding of protein phase behaviour is relevant in the context of the food[63–66] and pharmaceutical industry,[67,68] for the structural characterisation of proteins,[69] for understanding the behaviour of proteins within the crowded environment of a cell,[17,18] as well as for understanding numerous neurodegenerative diseases that have been linked to the formation of amyloid fibrils.[5] Furthermore, an understanding of protein dispersions is relevant to the design of bio-based and biomimetic molecular materials,[70] and due to its complexity it is of inherent scientific interest.

Proteins[12] have a heterogeneous surface that is different for every kind of protein, which gives rise to inherently anisotropic interactions with other proteins, even if they are globular.[25,71–73] The dependence of the surface properties and the charge distribution on the pH, and the dependence of electrostatic interactions on the ionic strength of the solution[74–77] add to the complexity.[67,78] In fact, proteins are never perfectly spherical, are in principle deformable[79] and in many cases are able to form supramolecular structures in native and non-native conformational states.[16,24,80,81] All of this translates into very rich phase behavior,[20] including liquid-liquid phase separation, crystallization, gelation and aggregation into a variety of different supramolecular structures.[16,24,80,81]

The coupling of conformation to phase behaviour of peptides has received some attention,[82,83] however the consequences of possible changes in protein conformation on liquid-liquid phase separation has to our knowledge received no prior attention. Inspired by a two-state model for polymer phase behaviour,[84] we theoretically address this topic. We do so by presuming a competition between two conformational states, being the native and a *single* non-native state that we do not specify. This differs from current models, which either presume the protein to remain in the native state and macroscopic phase behaviour to be reversible,[23] or presume the native state to be non-conserved with corresponding irreversible phase and/or aggregation behaviour.[16] We do not make this distinction here, but rather presume that changes in protein conformation in principle occur on a continuous scale ranging from being negligible to the complete loss of the native structure. We postulate that selection of the dominant non-native conformer is driven by the strength of the interactions between them and that these interactions ultimately drive condensation of the proteins. Whilst we presume protein phase behaviour to be reversible, we deduce from our model that reversibility is in some cases exceedingly slow and should not be observed on experimental time scales.

We presume that the change in protein conformation is the result of a change in the local microscopic environment of the protein, that is, it does not result from the hydrolysis of the protein into short polypeptides which is irreversible. Indeed, it is well known that the local environment can affect protein structure and that proteins must have some ‘conformational softness’ to perform their function within a living organism.[85–87] For instance, the adsorption of a protein at an interface almost invariantly result in conformational changes in the protein.[59,88] Also, changes in solution conditions can affect the protein conformation and even protein concentration alone affects the conformation of for example beta-lactoglobulin as we have seen in the previous chapter.[54] Here, we consider a system similar to this and let protein concentration be the source of changes in local environment. Through mass action, an increasing number of protein-protein interactions with increasing concentration, lead to an increasing number of proteins in the non-native state.

In principle, at fixed concentration such changes in local environment can result from a phase transition or local density fluctuations. Here, we run into a dilemma, which must come first? Does a phase transition induce changes in protein structure or do changes in protein structure induce a phase transition? Our work shows that the answer depends on the degree to which the conformation of the protein changes. For small changes in protein conformation, that we translate into a low free energy penalty relative to the native state, the phase transition induces a change in protein conformation. However for large changes in structure, i.e., a large free energy penalty, the new non-native conformation must typically be nucleated before a macroscopic phase transition (condensation) can occur. The two thermodynamic models that we invoke produce consistent predictions, suggesting that our conclusions are robust.

The remainder of this chapter is structured as follows. In section 3.2 we introduce our two-state protein model in which high free energy conformers are stabilised by attractive interactions with other high free energy conformers, and discuss its physical interpretation. In section 3.3 we show that a first-order conformational phase transition between a dispersion state with proteins mostly in their native state and a dispersion state with most proteins in their non-native state exists. In section 3.4 we combine our two-state protein model with a Flory-Huggins-type free energy[89,90] and with a Carnahan-Starling-based free energy[91] and discuss how phase and stability diagrams can be constructed.

In sections 3.5 and 3.6 we present and discuss the corresponding phase and stability diagrams where we show that the phase behaviour exhibits re-entrance and is non-universal, i.e., a law of corresponding states does not exist. Furthermore, we discuss the thermodynamic stability of the dispersion with respect to phase separation where, based on the local curvature of the free energy surface, we distinguish between spinodal decomposition and nucleation and growth. Additionally, we consider conformational relaxation of the proteins and show in section 3.6 that the presence of a first-order conformational phase transition causes the thermodynamic stability to become inherently dependent on the protein conformation.

Finally, in section 3.7, we provide an in-depth analysis of the predictions of our models to show that even if one presumes that changes in protein conformation occur on a continuous energetic scale, one finds a clear demarcation between a regime where the coupling between the phase behaviour and changes in protein conformation is weak, i.e., changes in protein structure are induced by a phase transition and have a negligible impact on phase behaviour, and a regime where the coupling is strong and the opposite holds true.

3.2 Two-state protein model

Our two-state protein model is based on the presumption that a protein can either be in its native state or in its non-native state, and that the protein can reversibly switch between these two states. There is a free energy difference ϵ (in units of thermal energy, $k_B T$) between these two states. There are steric (excluded-volume) interactions between all proteins, and proteins that are in the non-native state can engage in an attractive interaction with nearby proteins that are also in the non-native state. The strength of this interaction is measured by a dimensionless, so-called Flory parameter χ. All proteins that are in the non-native state are in an *identical*, non-native state. The model is graphically summarised in fig. 3.1.

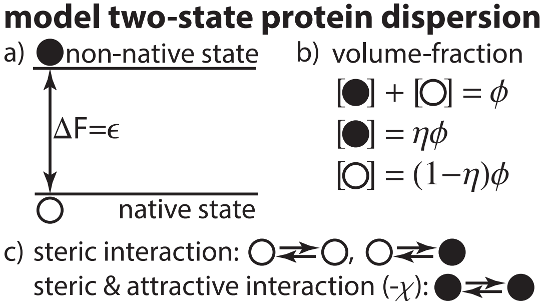
model two-state protein dispersion
a) ● non-native state
ΔF=ϵ
○ native state
b) volume-fraction
[●] + [○] = ϕ
[●] = ηϕ
[○] = (1−η)ϕ
c) steric interaction: ○⇄○, ○⇄●
steric & attractive interaction (-χ): ●⇄●

Figure 3.1: Ingredients of the two-state model. a) The native state (open circle) and non-native state (filled circle) of the model two-state protein are separated by a free energy difference ϵ (in units thermal energy). b) The overall protein volume fraction is ϕ, the fraction of proteins in the non-native state is η. c) The nature of protein-protein interactions depends on the conformational state of the proteins. All proteins interact via excluded volumes and nearby pairs of protein that are in the non-native state engage in attractive interactions of strength $-\chi$ (in units thermal energy).

The thermodynamic state of the protein dispersion depends, apart from the two energetic parameters, on the total volume fraction of protein, ϕ, which equals the protein number density times the volume of a protein, v_0, and the number fraction η of the proteins in the non-native state. Tacit assumption is that the volume of a protein is equal in both states, while this must not necessarily be the case, we presume this to be true for reasons of simplicity. In the next chapter we address the situation where the native and non-native conformation are not of equal effective volume and show that this strongly affects the predicted phase behaviour. So, if η is the number fraction of proteins in the non-native state, then $\eta\phi$ is the volume fraction of the solution occupied by proteins in the non-native state, while $(1-\eta)\phi$ is the volume fraction occupied by proteins in the native state. The volume fraction of solvent equals $1-\phi$.

We are now in a position to construct our free energy. Let N denote the total number of proteins in the dispersion. The total number of proteins in the non-native state must then be equal to $N\eta$, while the total number of proteins in the native state is $N(1-\eta)$. In the mean-field approximation the distribution of native and non-native states over the N proteins is independent, allowing us to directly write down the Gibbsian entropy due to the increased number of microscopic states available to the dispersion. The corresponding entropic contribution to the dimensionless free energy density is,

$$f_{\text{entr}} = \eta\phi \ln \eta + (1-\eta)\,\phi \ln 1 - \eta, \tag{3.1}$$

where f_{entr} is scaled to the volume of a single protein, v_0, and in units of thermal energy, $k_B T$. The enthalpic contribution to the free energy, we calculate next.

Having $N\eta$ proteins in the non-native state comes at a free energy cost of $N\eta\epsilon$, which corresponds to an increase of the dimensionless free energy density of $\eta\phi\epsilon$. The free energy cost of having proteins in the non-native state can be compensated for by attractive interactions between them of strength $-\chi$. From mean-field arguments it follows that the dimensionless free energy density associated with these interactions is $-\chi\,(\eta\phi)^2/2$, because the probability that two proteins that are in the non-native state and in range of each others attractive potential is proportional to $(\eta\phi)^2$, while the factor of $1/2$ corrects for double counting. Combining the two energetic contributions we obtain the following dimensionless free energy density,

$$f_{\text{enth}} = \epsilon\eta\phi - \frac{\chi}{2}\,(\eta\phi)^2\,. \tag{3.2}$$

The total contribution to the dimensionless free energy density of our two-state protein model is now given by,

$$f_{\text{2s}} = f_{\text{entr}} + f_{\text{enth}}. \tag{3.3}$$

In summary, the state of the protein dispersion is characterised by two order parameters, ϕ and η, while the external conditions and the protein properties determine the values of the two energetic parameters, χ and ϵ.[1] Because we lack a microscopic model for the latter two, we cannot predict how these respond to changes in say temperature and other solution conditions including ionic strength and acidity. Hence, we treat χ and ϵ as phenomenological parameters, also to keep the theory as general as possible. Although the phase behaviour predicted by our model is a function of χ and ϵ alone and not of the underlying microscopic model relating these parameters to solution conditions, these parameters are in principle amenable to experimental determination as a function of solution conditions.[74,77] For our purpose, it is important to realise that ϵ presumably increases with increasing departure from the native conformation and that χ, which drives macroscopic phase separation, is temperature dependent.

---

[1] Note that χ and ϵ are strictly speaking not enthalpies but free energies because they contain information about the solvent and protein degrees of freedom that have been glossed over in our coarse-grained model.

3.3 A first-order conformational phase transition

The equilibrium state of the protein dispersion is given by its minimum free energy state, hence the equilibrium fraction of proteins that are in the non-native state, η_{eq}, follows by setting the partial derivative of the free energy, $f_{2\mathrm{s}}$ as given by eqs. (3.1), (3.2) and (3.3), with respect to η, $\partial_\eta f_{2\mathrm{s}} \equiv \partial f_{2\mathrm{s}}/\partial\eta = 0$, giving,

$$\frac{\eta_{\mathrm{eq}}}{1-\eta_{\mathrm{eq}}} = \exp\left(\chi\phi\eta_{\mathrm{eq}} - \epsilon\right). \tag{3.4}$$

Note that we need not include contributions from steric interactions between the proteins for we presume them to have equal volume in both conformational states. An important consequence of the functional form of eq. (3.4) is that it, as we shall see, leads to non-universal phase behaviour, that is, there is no law of corresponding states.[2]

We read of from eq. (3.4) that the non-native state can only be stabilised by attractive interactions between proteins in the non-native state, because $\epsilon > 0$ is a free energy penalty. For attractive interactions $\chi > 0$, stabilisation of the non-native state is only effective at sufficiently high concentrations, ϕ. This can be rationalised by realising that entropy favours a dispersion state with an equal number of proteins in each conformation, but that the free energy cost associated with the non-native state favours as few proteins as possible in that state, while attractive interactions between proteins in the non-native state favours proteins to be in the non-native state. The competition between the latter two render the value of η_{eq} strongly concentration dependent.

It is instructive to consider the actual shape of the curves given by eq. (3.4) for small and large values of the energetic parameters, χ and ϵ. The dependence of the equilibrium fraction of proteins that are in the non-native state, η_{eq}, on the protein concentration, ϕ, is shown in fig. 3.2 for the two representative cases with $\chi = 3.5$ and $\epsilon = 1$ (fig. 3.2a) and $\chi = 10$ and $\epsilon = 3$ (fig. 3.2c) respectively. In the figure the solid line indicates a local free energy minimum ($\partial_{\eta\eta} f_{2\mathrm{s}} > 0$) at fixed value of ϕ while the dashed line indicates a local maximum ($\partial_{\eta\eta} f_{2s} < 0$). This is illustrated by figs 3.2b and 3.2d, which show the dimensionless free energy density on the η_{eq}-curve as shown in figs. 3.2a and 3.2c respectively. We present this dimensionless free energy in the next section and we only show the free energy for illustrative purposes here.

Fig. 3.2 shows that the dependence of η_{eq} on ϕ is fundamentally different for small and large values of χ and ϵ. For small values of the energetic parameters the fraction of proteins in the non-native state, η_{eq}, increases monotonically with concentration, ϕ. However, for large values of these parameters we obtain a van der Waals-like loop, indicative of thermodynamic instability. It is the presence of this thermodynamic instability that leads to the strong coupling of conformational changes within the proteins and the macroscopic phase behaviour that we eluded to in the introduction and explore in considerable detail in sections 3.6 and 3.7.

---

[2] This equation itself cannot be rewritten as a universal equation in terms of reduced variables.

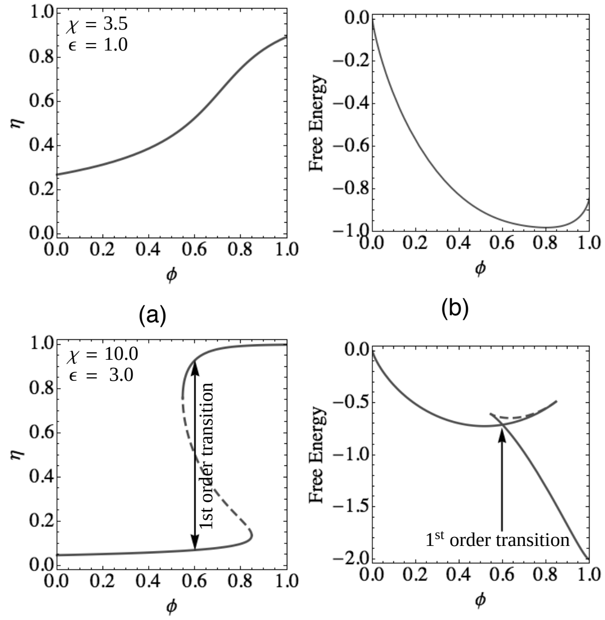

(a) (b)

(c) (d)

Figure 3.2: The equilibrium fraction of proteins in the non-native state, η_{eq} and the dimensionless free energy at $\eta = \eta_{\text{eq}}$ as a function of ϕ. We introduce the dimensionless free energy, f_{2sFH} defined in eq. (3.7), that is shown in these graphs in the next section and only show the free energy for illustrative purposes. a,b) For attractive interactions of strength $\chi = 3.5\ k_B T$ and a free energy penalty of $\epsilon = 1\ k_B T$ associated with the non-native state. c,d) For $\chi = 10$ and $\epsilon = 3$, solid lines represent stable equilibria while the dashed line represents unstable equilibria, both at fixed concentration, i.e., we suppress phase separation. The location of the first-order conformational phase transition is shown.

The thermodynamic instability occurs when both energetic parameters have values larger than thermal energy, $k_B T$, for under these circumstances a dispersion with approximately equal amounts of proteins in the native and the non-native state is no longer entropically stabilised. The equilibrium state of the dispersion is then either one where nearly all proteins are in the native state or one where nearly all protein are in the non-native state. These two equilibrium states are separated by a first-order conformational phase transition at constant concentration as indicated in fig. 3.2c. Of course, we must realise that we cannot keep the local concentration fixed and as it turns out this phase transition is intimately coupled to macroscopic phase separation, that for now we have suppressed.

Of the dispersion states separated by the van der Waals-like loop, at any concentration one of the two states is a meta-stable state and one is the equilibrium state, and the first-order conformational phase transition occurs when both dispersion states have equal free energy density. This is illustrated in fig. 3.2d where we show the dimensionless free energy density at $\eta = \eta_{\mathrm{eq}}$ (shown in fig. 3.2c) as a function of protein concentration for $\chi = 10$ and $\epsilon = 3$. Not suprisingly, it shows a similiar van der Waals-like loop, confirming that we are dealing with a first-order transition.

The presence of this van der Waals-like loop has an important kinetic consequence. Presuming model-C-like kinetics,[92] and having suppressed possible phase separation, the average protein conformation, η, will at all times spontaneously relax towards a value where the free energy is at a (local) minimum for the given concentration. While in the absence of the van der Waals-like loop conformational relaxation at a given concentration is always towards a unique dispersion state, this no longer holds true when the van der Waals-like loop is present. Here, the unstable part of the loop, i.e., the part that corresponds to a local maximum in the free energy, is a barrier separating dispersion states that relax towards a dispersion of mostly native and a dispersion of proteins mostly in their non-native state respectively. In section 3.6, we shall see that this has important consequences for the thermodynamic stability of the dispersion with respect to phase separation of these two states is not necessarily equal.

The first-order conformational phase transition between dispersion states exists only for $\chi \geq 4$ and $\epsilon \geq 2$, and in fact this demarcates the regimes of weak and strong coupling. In section 3.6 we show how this phase transition couples to macroscopic phase separation. But before that, we need to formulate the contribution to the free energy that take into account volume-exclusion between the proteins. For this purpose we rely on a simplistic lattice fluid model[89,90] as well as on the more accurate Carnahan-Starling equation of state.[91]

3.4 Solution model

The simplest model that one can write down for volume exclusion and mixing in a binary fluid is the Flory-Huggins model.[89,90] However, this presumes protein and solvent molecules to be roughly equally sized. Obviously this is not the case for a protein solution. On the other hand, water is a structured fluid implying that plausibly one can model water on the level of clusters.[93] A somewhat more sophisticated treatment is based on the Carnahan-Starling equation of state for a hard-sphere fluid,[91] which we also consider. As we shall see, both predict qualitatively identical phase behaviour, showing that our results are robust.

At the level of a Flory-Huggins-type lattice fluid model, we have the following contribution to the free energy resulting from mixing and volume exclusions,[89,90]

$$f_{\mathrm{FH}} = \phi \ln \phi + (1-\phi) \ln 1 - \phi, \tag{3.5}$$

where f is the dimensionless free energy density, scaled to the volume of a single protein, v_0, and in units of thermal energy, $k_B T$ and ϕ is the protein volume fraction.

Within the Carnahan-Starling treatment,[91] this free energy density reads,

$$f_{\mathrm{CS}} = \phi\left[\ln\phi - 1 + \frac{\phi\,(4-3\phi)}{(1-\phi)^2}\right]. \tag{3.6}$$

We can now combine the latter two free energy densities with that of our two-state model, (3.3). This gives the total dimensionless free energy density of the model protein solution for the two models,

$$f_{\mathrm{2sFH}} = f_{\mathrm{FH}} + f_{\mathrm{2s}}, \text{ and } f_{\mathrm{2sCS}} = f_{\mathrm{CS}} + f_{\mathrm{2s}}. \tag{3.7}$$

From these free energy densities we can calculate the binodals and spinodals, and hence construct phase and stability diagrams. In our case, the binodal describes coexistence between protein-rich and protein-poor phases whilst the spinodal demarcates the limit of thermodynamic stability of a homogeneous dispersion.

The former can be calculated by setting temperature, osmotic pressure and the chemical potential of the proteins equal in both coexisting phases. Equal temperature implies equal χ and ϵ in both phases, equal chemical potential of the proteins in the two phases implies equal value of $\mu = \partial_\phi f$, and $\partial_\eta f = 0$ for both phases.[3] Finally, equal osmotic pressures implies equal value of $f - \phi\mu$. The resulting set of equations must be solved numerically as a function of χ and ϵ to determine the composition of the coexisting phases.

The spinodal lines are given by lines of inflection on the free energy surface. Such lines are obtained by setting the determinant of the Hessian equal to zero, so $\partial_{\phi\phi}f\partial_{\eta\eta}f - \left(\partial_{\phi\eta}f\right)^2 = 0$, which can be solved analytically. The inflection lines are a complex set of lines in the $\phi - \eta$ plane and are shown for both free energy equations, eq. (3.7), as dotted lines in fig. 3.3, in the area enclosed by these lines the dispersion is thermodynamically unstable against macroscopic phase separation. In fig. 3.3, we again compare typical cases of weak and strong coupling and superimpose the spinodal region over the equilibrium value of the fraction of proteins in the non-native state, η_{eq}, as a function of the concentration, ϕ for both free energy equations. From fig. 3.3 it is clear that there are some differences between the results obtained from the two different free energies. However, in the remainder of this chapter we shall see that these differences are only quantitative while the corresponding phase behaviour is qualitatively identical.

We find that in the strong-coupling regime, where the van der Waals-like loop is observed, the unstable part of the loop is at all times located within the spinodal region. This shows, as advertised, that the first-order conformational phase transition and macroscopic phase separation are intimately coupled. This becomes even more apparent if we consider the binodal points, which are indicated in the same figure as squares and are separated by the underlying *conformational* phase transition in the strong-coupling regime. The local maximum in the free energy, indicated by the dashed line, is presumably a barrier that effectively separates the coexisting phases

---

[3] Note that η is a non-conserved order parameter and hence its chemical potential must be zero.

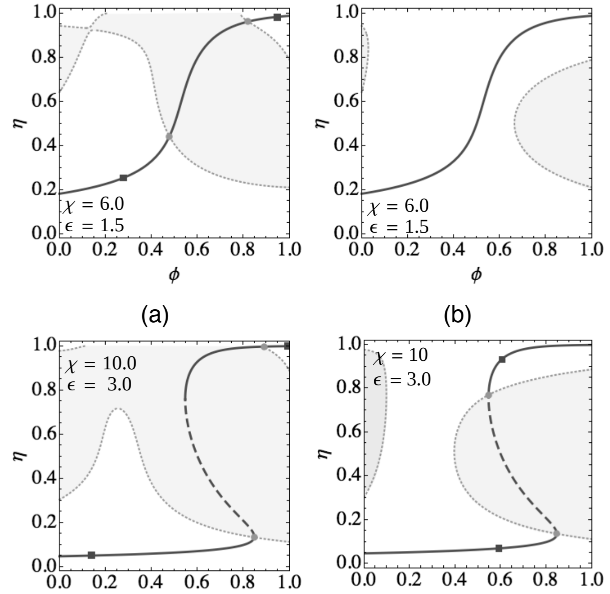

(a) (b)

(c) (d)

Figure 3.3: a) η_{eq} as a function of ϕ for $\chi = 6$ and $\epsilon = 1.5$ (solid and dashed line, see fig. 3.2 for details), coexisting states (squares) and the thermodynamically unstable region (shaded) enclosed by spinodal lines (dotted line). The intersection of the spinodal line and the η_{eq} curve (dot) is defined as the "equilibrium" spinodal points for the Flory-Huggins-type free energy. b) The same plot for $\chi = 6$ and $\epsilon = 1.5$ and for the Carnahan-Starling-based free energy. c) The same plot for $\chi = 10$, $\epsilon = 3$ and for the Flory-Huggins-type free energy d) The same plot for $\chi = 10$ and $\epsilon = 3$ and for the Carnahan-Starling-based free energy.

and might give rise to nucleation phenomena inside of the spinodal region depending on the initial conformational state of the proteins.

If we instantaneously prepare our system in a non-equilibrium state in the spinodal region, then the subsequent manner in which the protein dispersion relaxes should depend on the average conformation of the proteins prior to the quench, the free energy landscape and on the ratio, r_t, of the time scale at which conformational changes of a protein can take place and the self-diffusion time of the proteins. The latter follows from an analysis of the non-equilibrium behaviour in terms of a set of model-C-type kinetic equations.[92] While a complete analysis of the non-equilibrium behaviour is outside of the scope of this chapter, borrowing notions from kinetic theory does allow us to analyse certain aspects of it and pinpoint in the phase diagram what kind of kinetics predominates: nucleation and growth, spinodal decomposition or a combination of both. For our system, this turns out to be highly complex, non-universal and dependent on ϕ, η, χ and ϵ. In chapter 5 we investigate this in more detail and present a stability analysis of the Caranahan-Starling-based free energy.

For this, it makes sense to consider two limiting cases for r_t. In the first, $r_t \rightarrow \infty$, and the proteins are conformationally frozen, that is, η does not change on the diffusional time scale. The dispersion is effectively a three component dispersion, which perhaps is less interesting. In the second, more interesting case where $r_t \rightarrow 0$, relaxation of the protein conformation is instantaneous on the time scale of diffusion. In this situation, the states available to the protein dispersion are in effect restricted to states where $\eta \equiv \eta_{\text{eq}}$ and the stability of the dispersion is determined by the “equilibrium” spinodal points which are defined as the intersection of the spinodal lines and the η_{eq} curve and are shown as dots in fig. 3.3.

Presuming the limit of $r_t \rightarrow 0$ to hold we are now able to indicate various kinetic regimes in phase diagrams. This we do in the next two sections, where we demonstrate that for both thermodynamic solution models an identical demarcation between regimes of weak and strong coupling between conformational changes and macroscopic phase separation exists. In section 3.7 we briefly discuss how a finite non-zero value of r_t affects the results that we present in the next two sections and show that this does not invalidate these results.

3.5 Phase diagrams for the weak-coupling regime

In this section, we present phase and stability diagrams by taking $\epsilon = 0$ and $\epsilon = 2$, i.e., focus on the weak-coupling regime first that applies if $\epsilon \leq 2$. We project the resulting phase and stability diagrams onto the ϕ-χ plane and retrieve Flory-Huggins-like phase behaviour,[89,90] where changes in protein conformation are induced by macroscopic phase separation. Striking differences, however, are the loss of universality and the emergence of re-entrance in the phase behaviour. These differences disappear in the hypothetical limit $\epsilon \rightarrow -\infty$ where in our model the native state has vanishing probability.

The phase and stability diagram for the Flory-Huggins-based model for $\epsilon = 0$ is shown in fig. 3.4a, and that for $\epsilon = 2$ in fig. 3.4b. Those for the Carnahan-Starling-based model and the same values of ϵ in figs. 3.4c and 3.4d. The binodal is represented by the solid line, where coexisting states are joined by horizontal tie lines. The collection of “equilibrium” spinodal points, as defined in the previous section, is represented by the dotted line. Each of the diagrams consists of three regions. As is the case for the standard Flory-Huggins diagram, in region I the equilibrium state of the dispersion is a homogeneous state, in region II macroscopic phase separation occurs by nucleation and growth, while in region III it occurs by spinodal decomposition. Versions of these phase diagram in which the η direction is included are shown in fig. 3.5

By invoking the previously defined limit of $r_t \rightarrow \infty$, in which conformational changes of the protein occur instantaneously on the time scale of the self-diffusion of the pro-

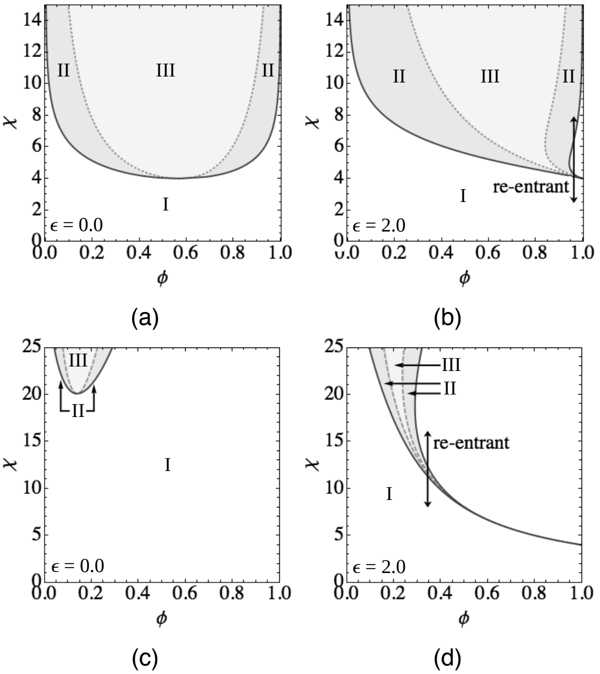

(a) (b)

(c) (d)

Figure 3.4: Phase and stability diagrams for our two-state protein model as a function of the interaction parameter χ and protein volume fraction ϕ. a) Results from Flory-Huggins-based model for free energy difference between native and non-native states of $\epsilon = 0$ (units of thermal energy). b) Flory-Huggins-based model for $\epsilon = 2$. c) Carnahan-Starling-based model for $\epsilon = 0$. d) Carnahan-Starling-based model for $\epsilon = 2$. The binodal is depicted as a solid line, the spinodal is given by the dotted line. In region I the equilibrium state is homogeneous, in region II phase separation occurs by nucleation and growth, in region III by spinodal decomposition. 3D versions of these phase diagrams, including the η-direction, can be found in fig. 3.5.

teins, we can address an important question: How does the average conformation of the proteins, as expressed in the value of η for a given concentration ϕ, affect the pathway towards thermodynamic equilibrium and why do we consider the coupling to be weak for $\epsilon \leq 2$? To answer this question, we consider the relaxation of a protein solution as a function of the concentration, ϕ, and the protein conformation, η, for the specific case of an interaction strength $\chi = 6$ and a free energy penalty on the non-native state $\epsilon = 1.5$, and refer to figs. 3.6a and 3.6b (Flory-Huggins-type free energy) and for $\chi = 20$ and $\epsilon = 1.5$, and refer to figs. 3.6c and 3.6d (Carnahan-Starling-based free energy). This case is representative of the behaviour in the weak coupling regime. Furthermore, the differences between the results for the two dif-

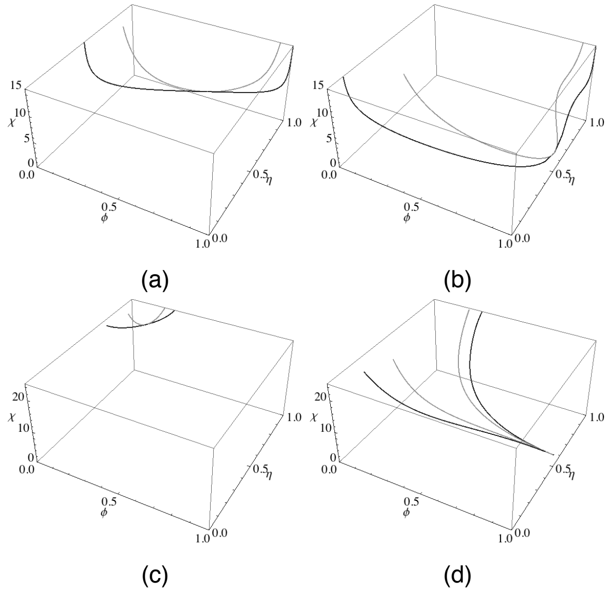

(a) (b)

(c) (d)

Figure 3.5: a-d) The phase diagrams for the same free energy equations and same values of ϵ as shown in figs. 3.4a-3.4d. The binodal is shown as the black solid line, the “equilibrium” spinodal as the solid grey line.

ferent free energies are again quantitative. For $\chi = 6$ the Carnahan-Starling-based model predicts no phase separation to occur, hence $\chi = 20$ is chosen because for this value phase separation does occur. While the location of the binodal and spinodal points is not equal for the two free energies, the corresponding phase behaviour is qualitatively identical as we shall show next.

In figs. 3.6a and 3.6c, the equilibrium fraction of proteins in the non-native state, η_{eq}, is given as a function of protein concentration, ϕ, for the two different free energy equations. The dots represent the “equilibrium” spinodal points and the squares coexisting states. Also drawn are the regions in the ϕ-η plane, where the equilibrium state of the dispersion is a homogeneous dispersion (region I) and where macroscopic phase separation occurs by nucleation and growth (region II) and by spinodal decomposition (region III). The boundaries between these regions are given by vertical lines, so at fixed concentration, through the binodal and the “equilibrium” spinodal points. This indeed shows that the predicted kinetic mechanism by which phase separation occurs is independent of the average protein conformation, η. This must be so because of our presumption that conformational relaxation of the proteins occurs instantaneously on the diffusion time scale. In other words, any solution state first relaxes to $\eta \equiv \eta_{\text{eq}}$ at fixed concentration before diffusion can cause local changes in concentration and hence the kinetic mechanism by which phase separation occurs

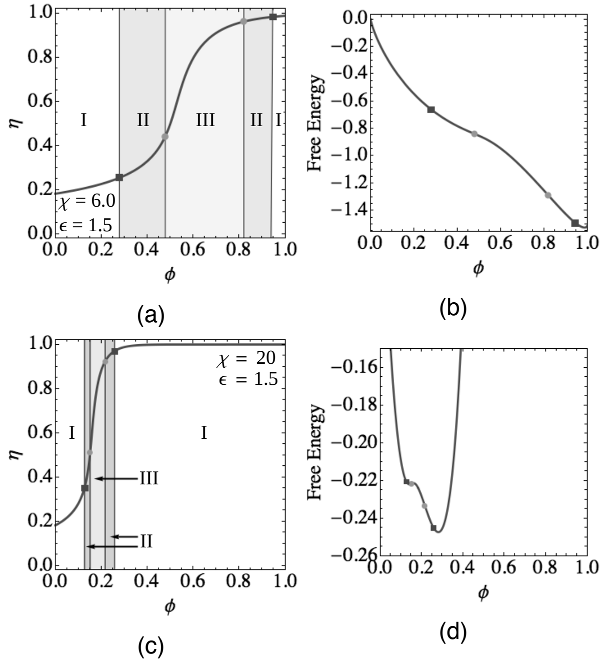

(a) (b)

(c) (d)

Figure 3.6: a) Equilibrium fraction of proteins in the non-native state, η_{eq}, as a function of ϕ for $\chi = 6$ and $\epsilon = 1.5$ (solid line), showing "equilibrium" spinodal points (dots) and binodal points (squares), calculated from the Flory-Huggins-based model. Regions I, II and III are defined as in fig. 3.4. b) Dimensionless Flory-Huggins-based free energy density along the η_{eq} curve, as shown in fig. 3.6a, including the indicated binodal and "equilibrium" spinodal points. c) The same type of plot as in fig. 3.6a but for $\chi = 20$ and $\epsilon = 1.5$ and for the Carnahan-Starling-based free energy. d) The same type of plot as in fig. 3.6b but now for fig. 3.6c.

is independent of protein conformation, η.

Effectively, the states available to the dispersion are restricted to states where $\eta \equiv \eta_{\text{eq}}$, and as a consequence a local change in concentration, ϕ, induces a corresponding change in η, such that the corresponding state lies on the η_{eq} curve. Hence, changes in protein conformation are enslaved by changes in local concentration. For these reasons, we consider the coupling between conformational changes and macroscopic phase behaviour weak. We shall see that this does not hold true for $\epsilon > 2$, where the coupling is strong.

Before discussing the strong-coupling regime, we consider how the phase and stability diagram changes when ϵ increases from 0 to 2. For both thermodynamic models (Flory-Huggins and Carnahan-Starling) the critical point shifts to larger concentrations with increasing value of ϵ. The reason for this is simple, the increasing conformational free energy cost of the transition to the non-native state must be compensated for by an increasing number of contacts between proteins in the non-native state. Interestingly, the phase behaviour exhibits (double) re-entrance for $\epsilon = 2$. As indicated by arrows in figs. 3.4b and 3.4d, within a limited concentration range, a continuous change in temperature and hence in χ causes the equilibrium state to shift from homogeneous to phase separated, to homogeneous and back to phase separated again. Re-entrace occurs approximately only for $\epsilon > 1.8$ for the Flory-Huggins-based model and for $\epsilon > 1.65$ for the Carnahan-Starling-based model.

For $\epsilon = 2$, the critical point lies for both solution models at the (admittedly unphysical) volume fraction of $\phi = 1$ and turns out to represent a multi-critical point. At that point, the critical point of liquid-liquid phase separation coincides with the critical point of an Ising-like conformational demixing transition. The latter gives rise to spatial domains characterised by different average conformation of the proteins at a fixed volume fraction of $\phi = 1$. This is to be expected, because the free energy density for $\phi = 1$ reduces to that of a mean-field Ising model. Note that at the critical point, for $\epsilon = 2$ the binodal has the shape of a cusp. Interestingly, as we shall see in the next section, for $\epsilon > 2$ the second order Ising-like transition turns into a first-order transition and there is no longer a real critical point for liquid-liquid phase separation. Finally we note that the diagrams shown in figs. 3.4a-3.4d cannot be rescaled by the critical concentration and χ value to obtain a universal phase diagram, that is, the phase behaviour is non-universal and there is no law of corresponding states.

3.6 Phase diagrams for the strong-coupling regime

The cross-over to strong coupling occurs at $\epsilon = 2$ and coincides with the presence of the multi-critical point at $\phi = 1$ and $\chi = 4$: it is the convolution of the critical point of liquid-liquid phase separation and that associated with the Ising-like conformational demixing at $\phi = 1$ as discussed in the previous section. The latter transition also corresponds to the first appearance of the first-order conformational phase transition and the associated van der Waals-like loop discussed in section 3.3. It is the presence of the van der Waals-like loop, in particular the unstable part of it, that gives rise to the strong-coupling regime. In the limit of $r_t \to 0$, in which conformational relaxation of the protein occurs instantaneously as discussed in section 3.4, this part of the loop is a barrier separating non-equilibrium dispersion states that instantaneously relax towards a dispersion state on either the lower or upper stable part of the loop. As we shall see, the kinetic mechanism by which phase separation subsequently occurs depends onto which of the two branches the system initially relaxes.

In fig. 3.7a the phase and stability diagram for the Flory-Huggins-based free energy is shown for $\epsilon = 3$. In it, the diagram is projected onto the ϕ-χ plane. The corresponding diagram for the Carnahan-Starling-based free energy is shown in fig. 3.7b. In these figures, the blue line represents the binodal and coexisting states are joined by horizontal tie lines, the green dotted line indicates the spinodal, while the region in between the red lines, which are situated mostly underneath the spinodal, demarcate the region where the van der Waals-like loop is observed. No fewer than a total of 13 regions, instead of just 3 for $\epsilon \leq 2$, have been identified in the diagram. In fig. 3.7a three of these regions (XI - XIII) are situated between the spinodal line and the upper boundary of the region where the first-order conformational phase transition exists. These regions are small in the diagram, and hence for clarity their location is shown schematically at the bottom of the phase diagram. In fig. 3.7b the same is done for regions III, XII and XIII. The background colours indicate the type of phase behaviour observed in each of the regions. In fig. 3.8 3D versions of these phase diagrams are shown in which the η-direction is included, here the binodal is shown as a black line and the "equilibrium" spinodal as a grey line. In this figure the Ising-like coexistence at $\phi = 1$ between phases of proteins in which the average protein conformation is different is clearly visible as the binodals nor the spinodals meet in a single point at $\phi = 1$.

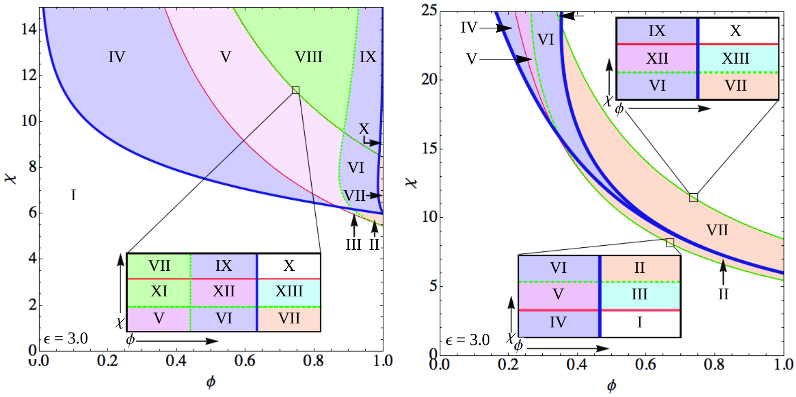

(a) (b)

Figure 3.7: The phase and stability diagram for $\epsilon = 3$ for a) the Flory-Huggins-based free energy and b) for the Carnahan-Starling-based free energy. The thick blue line represents the binodal, coexisting states are joined by horizontal tie-lines, the green dotted line represents the spinodal and the area enclosed by the red lines indicates the region where the van der Waals-like loop is present. Thirteen regions, each with distinct phase behaviour, as discussed below, are indicated. A 3D version of the diagrams is shown in fig. 3.8.

Before we address the phase behaviour in each of these regions, a few general remarks are in order. Firstly, the diagram as shown in fig. 3.7 is a good representation of the phase behaviour for $\epsilon \geq 2$ of both solution models. Hence in the following discussion we focus entirely on the behaviour of the Flory-Huggins-based model for $\epsilon = 3$. Before we discuss the phase behaviour in the strong coupling regime it is worth repeating that it is the unstable part of the van der Waals-like loop that separates non-equilibrium dispersion states that instantaneously relax towards either the lower (a) or

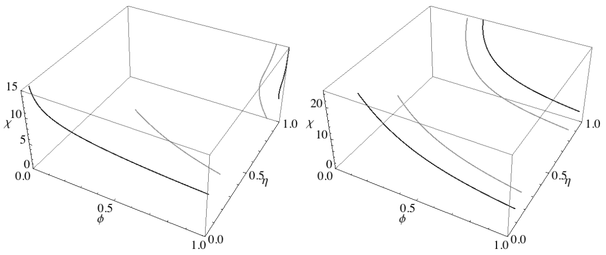

(a) (b)

Figure 3.8: a,b) The phase diagrams for the same free energy equations and same values of ϵ as shown in fig. 3.7. The binodal is represented by the black line and the "equilibrium" spinodal by the gray line

upper (b) stable part of the loop that is responsible for the complexity of the diagram. This becomes evident by taking ϕ-η slices out of the phase and stability diagram and including the η_{eq} curve for $\chi = 5.95$ (fig. 3.9) and $\chi = 10$ (fig. 3.10), both for $\epsilon = 3$.

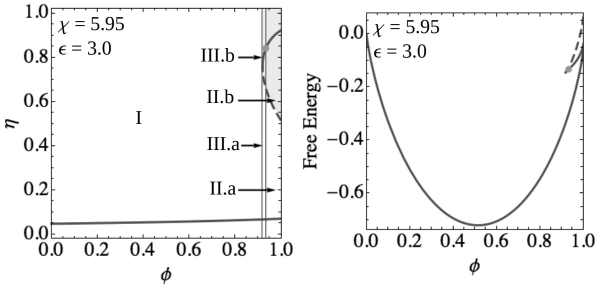

(a) (b)

Figure 3.9: a) Mapping of phase behaviour in ϕ-η space for $\chi = 5.95$ and $\epsilon = 3.0$ for the Flory-Huggins-based free energy, showing the η_{eq} curve, "equilibrium" spinodal point (dot). Regions I, II and III are situated in the corresponding regions in fig. 3.7, the behaviour in each of these regions is discussed below. b) The dimensionless Flory-Huggins-based free energy density along the η_{eq} curve for $\chi = 5.95$ and $\epsilon = 3.0$.

All regions shown in fig. 3.9a are part of regions I-III in fig. 3.7. Just as in the weak coupling regime, boundaries between these regions are at fixed value of ϕ, i.e., independent of η. Unlike in the weak coupling regime, there is an additional subdivision of regions II and III into two parts, which are separated by the unstable part of the van der Waals-like loop.

In region I, the dispersion is homogeneous and the equilibrium dispersion state is independent of the initial (non-equilibrium) value of η. In principle, the same holds true for regions II and III, however, here the presence of the van der Waals-like loop leads to the existence of meta-stable dispersion states that are located on the upper stable part of the loop. This becomes clear from fig. 3.9b in which we show the free energy as a function of ϕ. In region II.b these meta-stable states are thermodynamically stable against density fluctuations, while in region III.b these meta-stable states are thermodynamically unstable because the "equilibrium" spinodal has been crossed. If the activated relaxation towards the equilibrium state on the lower stable branch is sufficiently slow, one might expect to observe a spinodal decomposition-like process to occur on the upper branch in this region. This is suprising as there are no co-existing phases and the equilibrium state is a homogeneous dispersion with most proteins in their native state. The behaviour of the model dispersion in regions VII and XIII is similar to that in respectively regions II and III and hence we do not address it explicitly. Note that a summary of the phase and stability behaviour in each of the thirteen regions can be found in table 3.1.

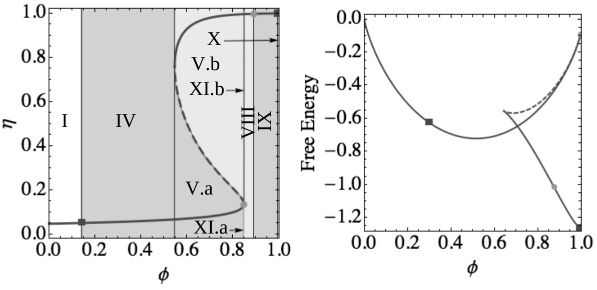

(a) (b)

Figure 3.10: a) Mapping of phase behaviour in ϕ-η space for $\chi = 10.0$ and $\epsilon = 3.0$ for the Flory-Huggins-based free energy, showing the η_{eq} curve, "equilibrium" spinodal points (dots) and binodal points (squares). The regions as indicated are situated in the corresponding regions in fig. 3.7, the behaviour in each of these regions is discussed below. b) The dimensionless free energy density along the η_{eq} curve for $\chi = 10.0$ and $\epsilon = 3.0$.

Focusing now on the case $\chi = 10$ and $\epsilon = 3$, phase separation is possible and the exact phase behaviour of the dispersion depends on both ϕ and η. This is shown in fig. 3.10a, in which a total of 7 different regions are shown. As before, in regions I and X the equilibrium state of the dispersion is homogeneous and independent of the initial value of η, see fig. 3.10b. In regions IV and IX phase separation must occur by nucleation and growth and in region VIII by spinodal decomposition. In regions V and XI the kinetic pathway by which phase separation occurs depends on the initial average protein conformation, η. In region V.a phase separation proceeds by nucleation and growth and by spinodal decomposition in region V.b. The behaviour in regions VI and XII is similar to that in regions V and XI with phase separation by nucleation and growth or spinodal decomposition depending on the initial average protein conformation. A summary of the phase and stability behaviour in each of the thirteen regions can be found in table 3.1.

Region	a) Lower part of loop	b) Upper part of loop
I	Homogeneous	Homogeneous
II	Homogeneous	Meta-stable
III	Homogeneous	Meta-stable & spinodal decomposition
IV	Phase separation by nucleation and growth	Not present
V	Phase separation by nucleation and growth	Phase separation by spinodal decomposition
VI	Phase separation by nucleation and growth	Phase separation by nucleation and growth
VII	Meta-stable	Homogeneous
VIII	Not present	Phase separation by spinodal decomposition
IX	Not present	Phase separation by nucleation and growth
X	Not present	Homogeneous
XI	Phase separation by spinodal decomposition	Phase separation by spinodal decomposition
XII	Phase separation by spinodal decomposition	Phase separation by nucleation and growth
XIII	Meta-stable and spinodal decomposition	Homogeneous

Table 3.1: Overview of phase and stability behaviour in regions I-XIII as shown in figs. 3.7, 3.9 and 3.10. The lower part of the loop refers to the stable portion of the η_{eq} curve below the unstable part of the van der Waals-like loop while the upper part refers to part of the loop above it, see fig. 3.2. Note that in region I the van der Waals-like loop in the η_{eq} curve does not exist.

An interesting feature of the phase behaviour of our model proteins in the strong-coupling regime is that, *if* initially most proteins are in their native state, the concentration interval where phase separation occurs by spinodal decomposition is small. In fact, the only region where this occurs are regions XI.a and XII.a. It arguably does not happen in region VIII because here spinodal decomposition must be preceded by relaxation of nearly all proteins to their non-native state, which plausibly does not occur instantaneously. The concentration interval over which we expect to see spinodal decomposition, $\Delta\phi_s$, is plotted as a function of χ and ϵ for both the Flory-Huggins and Carnahan-Starling-based free energy in fig. 3.11. In that figure, and also in fig. 3.7, we see that for sufficiently small values of χ the regions XI and XII are not present at all, and phase separation must always be nucleated in a dispersion of proteins in their native state.

In conclusion, in the strong coupling regime phase separation in a dispersion of mostly native proteins must almost always occur by nucleation and growth. It must be remarked that this conclusion follows from a somewhat limited kinetic analysis that is based on the presumed limit of instantaneous conformational relaxation, $r_t \to 0$. In spite of this, it is clear that the unstable part of the van der Waals-like loop poses a barrier that effectively demands the model dispersion to phase separate through nucleation and growth at least if most proteins are initially in their native state.

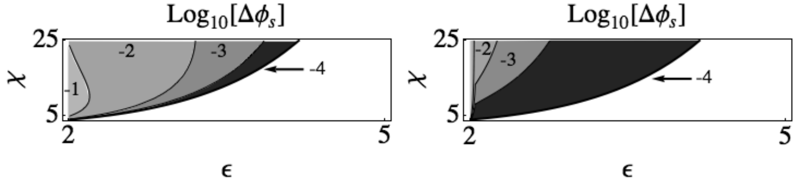

(a) (b)

Figure 3.11: Size of the concentration interval, $\Delta\phi_s$, for which phase separation occurs by spinodal decomposition if the proteins are initially in their native state as a function of χ and ϵ (as defined in fig. 3.1). For a) the Flory-Huggins-based and b) the Carnahan-Starling-based free energy. Note that in the non-shaded region phase separation never occurs by spinodal decomposition.

3.7 Discussion

We presented a theoretical study into the effects of the coupling of conformational changes and protein phase behaviour. In our model, native state proteins can reversibly switch to a high-energy non-native (e.g., unfolded) state. Both conformers interact through volume exclusion, whilst proteins in the non-native state also attract each other. For simplicity we assumed that both conformers are of equal shape and volume. The model allows us to study the phase behaviour as a function of the energy difference between the native and non-native state and the strength of the interaction between proteins in their non-native state.

Our results show that there are two regimes, a regime of weak and one of strong coupling, which are demarcated by a free energy difference of 2 k_BT between the two conformers. In the first regime, so for small free energy differences, the coupling between conformational changes and phase behaviour is weak. The phase behaviour is reminiscent of classical phase separation between solvent and solute. However, there are important differences: 1) the phase behaviour is non-universal, 2) under the right conditions the dispersion exhibits double re-entrance, and 3) changes in concentration induce changes in protein conformation.

The strong coupling regime manifests itself in three clear ways: 1) the classical critical point for phase separation disappears, 2) there is a conformational phase separation in the solvent-free (dry) system, 3) the emergence of unusual meta-stable dispersion states. This leads to a plethora of kinetic regimes, a total of 13 for both models investigated. These regimes reflect differences in the kinetic pathway towards a phase separated dispersion, depending on the average protein conformation prior to phase separation. For example, for a given concentration, phase separation can occur by nucleation and growth if most proteins are initially in their native state, while it occurs by spinodal decomposition if this is not the case.

Significantly, it turns out that phase separation in a dispersion of native proteins must almost always proceed by nucleation and growth. In that case, phase separation must be initiated by a coherent change in the conformation of proteins. Protein conformation is no longer enslaved to concentration and hence mass transport. One of our most unusual findings is that there are regimes in which there is a kinetic pathway between homogeneous dispersion states that, according to our interpretation of the model, must involve temporary phase separation.

In current protein literature, modeling of phase separation in solution ignores possible changes in conformation,[71–73,75,77] while the modeling of aggregation into supramolecular assemblies, including amyloid fibrils, hinges on changes in conformation.[16,24,80,81] We argue that the demarcation between weak and strong coupling of phase behaviour and conformational changes as predicted by our model is reminiscent of this distinction. We realise that our model does not allow for any amyloid-like structure to appear. Furthermore, because we employ equilibrium theory any irreversible binding or conformational changes is ignored, so this conclusion is tentative.

Our analysis of the thermodynamic stability and kinetic pathways towards equilibrium relies on the presumed limit of $r_t \to 0$. This means that conformational changes occur instantaneously on the self-diffusion time scale of the proteins. This assumption is probably not always realistic, yet it simplifies the kinetic analysis. If the limit of $r_t \to 0$ does not hold, the kinetics by which phase separation occur depends at all times on the initial protein conformation. The simple subdivision in phase separation by spinodal decomposition or by nucleation and growth no longer holds. A more subtle processes is possible, where at first phase separation must occur by nucleation and growth, but where, before a nucleation event has occurred, conformational relaxation forces the dispersion into a thermodynamically unstable state and phase separation proceeds by spinodal decomposition. We study this and similar kinetic processes in chapter 5 from the perspective of dynamic density functional theory.

The consequences of these more complicated kinetic pathways towards a fully phase separated dispersion leave our conclusions intact. In the weak coupling regime, conformational relaxation is, at a given concentration, always towards the same average protein conformation. However, in the strong coupling regime we have seen that, depending on the initial average conformation, the dispersion relaxes toward either of two different dispersion states. Because the thermodynamic stability of these two states is not necessarily equal, this presents a fundamentally different coupling between conformation and phase behaviour. Hence, the demarcation between the weak and strong coupling regimes holds beyond the presumed limit of $r_t \to 0$.

Much of the interesting behaviour predicted by our models occurs at very high concentration, where the protein might crystallize. It would be interesting to see how the phase behaviour predicted by our model couples to crystallization. We have invoked a simple van der Waals-solid model,[94] which led to unphysical results. As there are no attractive interactions between proteins in the native state within our model, phase separation leads to a dense phase of attractively interacting proteins in their non-native state. Phase separation is then always thermodynamically more favourable than crystallization of non-interacting native proteins. Clearly, more work is required to couple our model to a crystallization model.

Finally, a few remarks must be made on the similarities and differences between the Flory-Huggins-type and Carnahan-Starling-type free energies. Although the phase and stability diagrams appear to be distinctly different in shape for both models, the underlying structure is identical and hence both models support the existence of a demarcation between a weak and strong coupling regime. The main cause for the difference in shape of the diagrams is that in the Carnahan-Starling-type model the free energy more strongly increases with protein concentration, leading to the formation of a less dense dispersion of proteins in the non-native state by phase separation.

In the next chapter we extend the model presented in this chapter to also include changes in the size of the protein upon transitioning to the non-native state and show that this significantly affects the predicted phase behaviour. However, we also show that the key results presented in this chapter, being the demarcation between regimes of weak-coupling and strong-coupling, remain valid even if the native and non-native conformation are not of equal size.

Chapter 4

Self-crowding induced phase separation

Summary

In this chapter the effects of changes in volume exclusion on protein conformation and solution phase behaviour is studied. Our model two-state proteins can reversibly switch between a native and an excited non-native state. The proteins interact by excluded volumes regardless of conformation, upon transition to the non-native state the effective radius of the protein increases. Proteins in the non-native state interact attractively with other proteins in the non-native state. For high concentrations the native state is stabilised by volume exclusion, while for intermediate concentrations phase separation is suppressed and a dispersion of proteins mostly in their non-native state is stabilised. Concurrent with these effects is the presence of two first-order transitions at fixed concentration and two separate regimes of phase separation of which the latter is induced by self-crowding effects.

The contents of this chapter has been submitted for publication as: J. Stegen and P. van der Schoot, Self-crowding induced phase separation in protein dispersions.

4.1 Introduction

Protein phase behaviour is often modeled by presuming that the proteins are structureless and undeformable spherical particles. However, proteins do have an internal structure and it is well known that this structure may respond to changes in the local environment. This includes changes in physico-chemical conditions,[12] assembly and complexation,[61,95–97] and even non-bonded interactions between the proteins at elevated concentrations.[98] The response of the structure of a protein to such changes can induce changes in its effective volume that includes the tightly bound hydration water and the interactions between the proteins. This implies that in crowded environments, where the free volume is limited due to presence of a high concentration of macromolecules such as is the case in the cell,[99,100] interactions between proteins may be different from that in a dilute solution.[17,101–104] Crowding tends to increase, e.g., protein complexation rates, and shifts the equilibrium towards more compact conformations and to assembled states because it increases the free volume of the solution.[17] Hence, crowding stabilises compact (native) protein conformations.[98,105–107] On the other hand, diffusion-limited associative reactions slow down due to a decrease in diffusivity.

It is clear that gaining an understanding of how crowding couples to protein phase behaviour and the conformational stability of the protein is important scientifically. Moreover, industrial applications in food[64] and pharmaceutics[68] involve dense protein formulations, which are difficult to process and exhibit unwanted phenomena like syneresis, i.e., the explusion of water. That crowding, including self-crowding, is important and that the study of proteins in dilute solutions is not necessarily helpful in understanding the physical properties of such systems is well recognised.[108] Indeed, in an increasing number of experiments, crowding agents are added or the experiments are carried out in living cells to address crowding-related effects, e.g., in complexation and folding.[19]

While our understanding of how crowding induces phase separation in multi-component systems is relatively advanced,[109–111] it is to our knowledge not known how self-crowding affects protein phase behaviour in the liquid phase. Here, we study theoretically how volume-exclusion between a single type of model protein influences the switching between two conformational states, native and non-native, and through that the interactions between the proteins. We show that if these two conformational states have different effective volumes, even if this difference is very small, it profoundly affects the phase behaviour. We find that with increasing concentration, following liquid-liquid phase separation in which in the dense phase the non-native state is more prevalent, a second phase separation occurs in which the native state becomes more stable again.

The model that we make use of is an extension to a two-state protein model that we studied in the previous chapter. In the extended model we presume there is a thermodynamic equilibrium between a native and an excited (high-energy) non-native conformation of the protein that we both presume to be spherical but to have different hard-core radii. All model proteins interact with each other sterically, while the proteins in the non-native state also attract each other. Key parameters in the model are κ, the ratio of the hard-core diameters of the two conformers, ϵ, the free energy difference between the excited non-native state and the native state of the protein, and χ, a free energy that characterises the strength of the attractive interactions between proteins in the non-native state. Hence, we calculate phase diagrams of our model protein solution as a function of these three parameters and as a function of protein concentration, and find that these are exquisitely sensitive to the value of κ. This suggests that one can not treat proteins as simple nanocolloids.

In the remainder of this chapter, we present our model free energy in section 4.2 and use this to determine the equilibrium phase behaviour in sections 4.3 and 4.4. In section 4.3, we investigate how the equilibrium fraction of proteins in the non-native state depends on the concentration and on the three model parameters, and show that there are two first-order conformational phase transitions. This leads to a total of 5 qualitatively different relationships between protein concentration and conformation. In section 4.4, we determine the corresponding phase diagrams and show how both first-order conformational phase transitions are coupled to liquid-liquid phase separation. Furthermore, we show that a distinction between two qualitatively different types of phase diagram can be made. An aspect of theoretical interest is that in our model protein volume fraction is a non-conserved order parameter. Finally, in section 4.5 we summarise and discuss the results.

4.2 Free energy model

Our model dispersion consists of an implicit solvent and two types of spherical particle 1 and 2, with diameters d_1 and $d_2 \geq d_1$. Particles 1 and 2 represent the two different states of our protein and can reversibly interconvert where a free energy penalty $\epsilon \geq 0$ is assigned to particle 2 (the non-native state). Both types of particle interact via hard-core volume exclusion, whereas particles in state 2 also attract each other via some unspecified interaction potential.

We construct a free energy for this model system by combining the free energy of a bidisperse hard-sphere fluid that we derive from the polydisperse Boublik-Mansoori-Carnahan-Starling-Leland (BMCSL) equation of state,[112,113] a van der Waals-like term that accounts for attractive interactions between the non-native species, a term describing the interconversion between the two states.

The BMCSL equation of state can be integrated isothermally over the volume to obtain the corresponding Helmholtz free energy. If we define the dimensionless free energy density as $f = v_1 \beta F/V$, where v_1 is the volume of a single protein that is in its native state, $1/\beta = k_B T$ is the thermal energy and V is the system volume, then the BMCSL contribution to the free energy reads,

$$f^{\mathrm{HS}} = (1-\eta)\,\phi \ln(1-\eta)\,\phi + \frac{\eta\phi}{\kappa^3}\ln\frac{\eta\phi}{\kappa^3} - (1-\eta)\,\phi - \frac{\eta\phi}{\kappa^3} + \phi\left(1+\frac{1-\kappa^3}{\kappa^3}\eta\right) \times \left[\frac{3\,(1-y_1-y_2-y_3/3)}{2\,(1-\phi)^2} + \frac{3y_2+2y_3}{1-\phi} - \frac{3\,(1-y_1+y_2+y_3)}{2} + (y_3-1)\ln(1-\phi)\right] \tag{4.1}$$

where ϕ is the total protein volume fraction and η is the fraction of the volume of protein that corresponds to proteins in the non-native state. The terms y_1, y_2 and y_3 are defined as

$$y_1 = \eta\,(1-\eta)\,\frac{(1-\kappa)^2\,(1+\kappa)}{\kappa^3+(1-\kappa^3)\,\eta}, \tag{4.2}$$

$$y_2 = \eta\,(1-\eta)\,\frac{(1-\kappa)^2\,(\kappa+(1-\kappa)\,\eta)}{\kappa^3+(1-\kappa^3)\,\eta}, \tag{4.3}$$

$$y_3 = \frac{(\kappa+(1-\kappa)\,\eta)^3}{\kappa^3+(1-\kappa^3)\,\eta}, \tag{4.4}$$

where $\kappa = d_2/d_1$ with d_2 the effective diameter of the protein when it is in the non-native state and d_1 the effective diameter of the protein when it is in its native state. In this work we presume the native conformation to be the more compact conformation, that is, $\kappa \geq 1$.

Again, for simplicity, we presume that only particles of type 2 attract each other. Within a mean-field van der Waals-type of approximation,[114] we account for this in a dimensionless free energy density contribution of the form,

$$f^{vdW} = -\frac{\chi}{2\kappa^3}(\eta\phi)^2, \tag{4.5}$$

where χ describes the attractive part of the interaction between particles of type 2 and is given in units of thermal energy ($k_B T$). As we presume particle type 2 to be a high energy non-native state of the proteins, we add a free energy of the form,

$$f^{\mathrm{Conf}} = \frac{\eta\phi}{\kappa^3}\epsilon, \tag{4.6}$$

where κ enters because of our normalisation of the free energy density.

The total dimensionless free energy density of the model two-state protein dispersion is now,

$$f = f^{\mathrm{HS}} + f^{\mathrm{vdW}} + f^{\mathrm{Conf}}, \tag{4.7}$$

where f^{HS} is given by eq. (4.2), f^{vdW} by eq. (4.5) and f^{Conf} by eq. (4.6). Note that for $\kappa = 1$, we retrieve the dimensionless free energy density for a monodisperse Carnahan-Starling-based model as presented in the previous chapter, eq. (3.7).[91]

Because proteins can reversibly switch between conformations of different effective volumes, neither the overall protein volume fraction, ϕ, nor the fraction of the protein volume in the non-native state, η, are conserved quantities. While the quantity η may seem unusual, it is directly related to the number fraction of proteins in the non-native state, η_N, via the relation,

$$\eta_\mathrm{N} = \eta / \left(\kappa^3 + \left(1-\kappa^3\right)\eta\right). \tag{4.8}$$

We realise that this parameter offers a more intuitive description of the conformational state of the proteins, however the parameter η enters our hard-sphere free energy directly from the BMCSL equation of state.

While the overall protein volume fraction, ϕ, might seem a natural concentration scale, in our case it is a little unusual because it is non-conserved. The overall number density of proteins is a conserved quantity and it is possible to introduce a dimensionless concentration that is proportional to this quantity and that is also conserved. A natural dimensionless concentration that does that is the volume fraction the proteins would occupy if all proteins were in the native state,

$$\phi_\mathrm{Na} = \phi\left(1 + \frac{1-\kappa^3}{\kappa^3}\eta\right). \tag{4.9}$$

Importantly, experimentally it is readily determined because it is a direct measure for the amount of proteins dissolved.

In summary, we have put forward a dimensionless free energy density for our model protein dispersion. Solution conditions and protein properties are reflected in the parameters χ, ϵ and κ, while the thermodynamic state of the dispersion is given by ϕ or ϕ_Na and η or η_N. In the next section, section 4.3, we determine the equilibrium fraction of proteins in the non-native state as a function of concentration, and show that volume exclusion stabilizes the native state at high concentrations.

4.3 Stabilization of the native state at high concentrations

The equilibrium fraction of proteins in the non-native state minimises the free energy for a given amount of dissolved protein, ϕ_Na. Hence, we set

$$\left(\frac{\partial f}{\partial \eta_\mathrm{N}}\right)_{\phi_\mathrm{Na},\chi,\epsilon,\kappa} = 0. \tag{4.10}$$

We solve the resulting implicit equation numerically and determine whether they are free energy minima or maxima. As we shall see, the local maximum values are physically relevant, because they correspond to a free energy barrier between different (meta-)stable dispersion states with different fractions of proteins in the non-native state at fixed concentration. Furthermore, we will show that these local maxima can be crossed by two different first-order conformational phase transitions at fixed concentrations, giving rise to no fewer than 5 qualitatively different relations between equilibrium protein conformation and protein concentration. The loci of liquid-liquid phase separation we determine by equating chemical potentials and pressures in the coexisting phases. These can be calculated from our free energy, eq. (4.7), where the chemical potential is proportional to $\partial_{\phi_{\mathrm{Na}}} f$ and the osmotic pressure to $-f + \phi_{\mathrm{Na}} \partial_{\phi_{\mathrm{Na}}} f$. In this section we focus first on how the equilibrium number fraction of proteins in the non-native state, $\eta_{\mathrm{N}}^{\mathrm{eq}}$, varies with protein concentration, ϕ_{Na}. In the following section we will discuss phase diagrams in more detail.

To set the stage, let us first consider qualitatively how the equilibrium value of η_{N}, $\eta_{\mathrm{N}}^{\mathrm{eq}}$, depends on the protein concentration, ϕ_{Na}, and the other three model parameters, χ, ϵ and κ. This dependence essentially involves four different competing effects. The first three effects also hold for a system in which both conformations are of equal size, $\kappa = 1$, and are, 1) entropy, which favours equal amounts of proteins in both conformations, 2) attractive interactions of strength χ between proteins in the non-native state, which favour as many proteins in the non-native state as possible, and 3) the free energy penalty associated with the non-native state, ϵ (≥ 0), which favours as few proteins as possible in the non-native state. The competition between the latter two effects is strongly concentration dependent. The size difference between the two conformations introduces a fourth competing effect: 4) self-crowding (excluded-volume) effects that favour as few proteins as possible in the non-native state. This becomes more important with increasing protein concentration when the system runs out of free volume.

To illustrate how self-crowding influences how $\eta_{\mathrm{N}}^{\mathrm{eq}}$ varies with ϕ_{Na}, we set $\chi = 6$ and $\epsilon = 0$, both in units $k_B T$. We focus on the case where the effective diameter of the protein increases by a mere 5 percent upon transitioning to the non-native state, so $\kappa = 1.05$ and compare this with the case where $\kappa = 1$ and self-crowding is absent. Fig. 4.1a shows that without self-crowding, $\eta_{\mathrm{N}}^{\mathrm{eq}}$ increases monotonically with concentration. Fig. 4.1b on the other hand shows that with self-crowding this is no longer the case: self-crowding suppresses the non-native state at high enough concentration. As a result of this the dependence of $\eta_{\mathrm{N}}^{\mathrm{eq}}$ on concentration exhibits a maximum. Notice that the area shaded in gray in fig. 4.1b corresponds to actual volume fractions larger than unity, which of course is unphysical.

If we increase the strength of the attractive interaction between proteins in the non-native state from $\chi = 6$ to 12 and 40, this leads to a qualitatively different behaviour. Fig. 4.2a shows that for $\chi = 12$ the relation between conformation and concentration exhibits a van der Waals-like loop, signifying a first-order conformational phase transition. The dashed line in fig. 4.2a corresponds to a local maximum in the free energy that separates a local (meta-stable) and a global minimum (stable) free energy dispersion state for a fixed value of ϕ_{Na}.

Indicated in the figure (with a double-pointed arrow) is where the conformational transition would occur if there were no macroscopic phase separation. This happens at equal free energies provided the concentration is fixed. In fact, in section 4.4, we show that this conformational transformation is intimately linked to the transition from

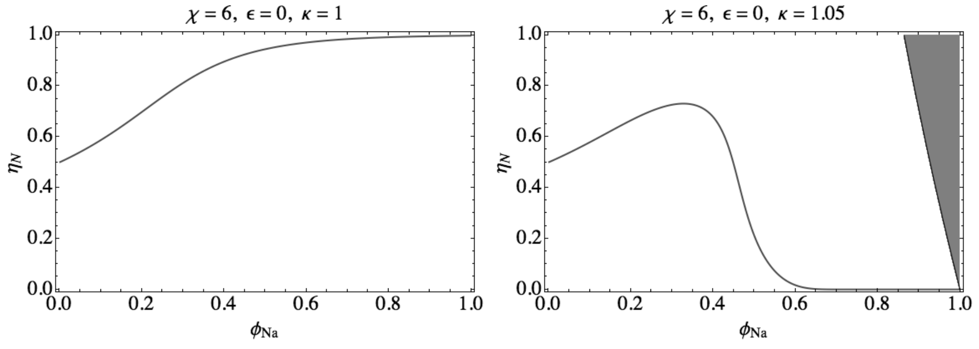

(a)

(b)

Figure 4.1: The equilibrium fraction of proteins in the non-native state, $\eta_{\mathrm{N}}^{\mathrm{eq}}$, as a function of protein concentration, ϕ_{Na}. The strength of the attractive interactions between the non-native proteins is $\chi = 6.0\ k_B T$ and the free energy penalty associated with the non-native state is $\epsilon = 0$. a) Both conformers are of equal size, $\kappa = 1$. b) The non-native conformer is 5 percent larger than the native conformer, $\kappa = 1.05$. The shaded area indicates unphysical dispersion states where the protein volume fraction exceeds 1.

a homogeneous dispersion to a liquid-liquid phase separated dispersion in which the concentrations and conformational states are not equal. The conditions for which we have coexisting phases are indicated in the figure by black dots.

The conformational phase transition that occurs is a result of the competition between self-crowding effects and the attractive interactions between proteins in their non-native state, which respectively favour a state with most proteins in their native and non-native state. With an increase of the strength of the attractive interactions between the proteins in the non-native state, the non-native conformation remains thermodynamically stabilised up to a higher concentration when crowding effects take over as is shown in fig 4.2b.

When the free energy difference between the native and non-native state is increased to a non-zero value this increases the thermodynamic stability of the native conformation even when proteins in the non-native state strongly attract each other. Fig. 4.3a shows that for $\chi = 15$, $\epsilon = 3$ and $\kappa = 1.05$, the native conformation is thermodynamically stable for all concentrations. The effect of self-crowding becomes clear if we compare this to the situation where both conformations are of equal size and self-crowding plays no role, fig. 4.3b. In this case the non-native conformation is thermodynamically stabilised at high concentrations.

In fig. 4.3b a second type of van der Waals-like loop presents itself, different from the one shown in fig. 4.2. Associated with it is another first-order conformational phase transition that results from the competition between the tendency of proteins

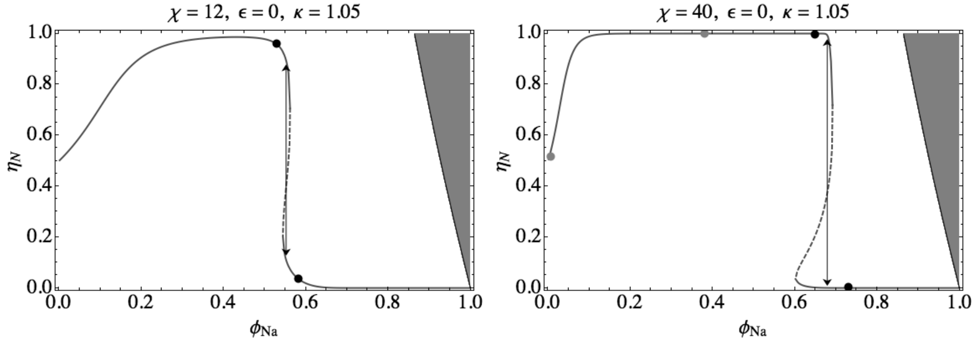

(a) (b)

Figure 4.2: The equilibrium fraction of proteins in the non-native state, $\eta_{\rm N}^{\rm eq}$, as a function of protein concentration, $\phi_{\rm Na}$ and a size difference of 5 per cent, $\kappa = 1.05$ and zero free energy difference between the two , for a) $\chi = 12$ and b) $\chi = 40$. In both figures the solid line corresponds to a (local) minimum while the dashed line corresponds to a maximum in the free energy. The concentration at which a first-order conformational phase transition would occur in a homogeneous solution is indicated by a double-pointed arrow. In reality, the solution phase separates and coexisting phases are indicated by the black and grey dots. See also the caption of fig. 4.1 for further details.

to remain in their native state due to the increase in conformational free energy, ϵ, and the tendency of proteins to switch to the non-native state and lower the free energy through attractive interactions of strength χ.

Let us now consider how the relation between protein concentration and conformation changes, as we slowly increase the value of κ from 1 upto 1.05 while the other two model parameters remain fixed at $\chi = 15$ and $\epsilon = 3$. In doing this, we investigate how precisely the concentration dependence of $\eta_{\rm N}^{\rm eq}$ changes from the one shown in fig 4.3b to the one shown in fig. 4.3a.

If the effective diameter of the non-native state of the protein increases by just 0.01 percent upto $\kappa = 1.0001$, then a second first-order conformational phase transition appears at high concentration as is shown in fig. 4.4a. This transition has the same physical origin as the one shown in fig. 4.2, where self-crowding causes the larger non-native state to become unfavourable at high volume fractions. With increasing κ, self-crowding effects become significant at a lower protein concentration, and the van der Waals-like loop at high concentrations $\phi_{\rm Na}$ shifts to lower concentrations. This continues until $\kappa \approx 1.0002$, when the lower boundary of both loops meet in a single point as is shown in fig. 4.4b.

A further increase in κ leads to a change in the structure of the free energy landscape, where both van der Waals-like loops merge separating a regime of (meta-

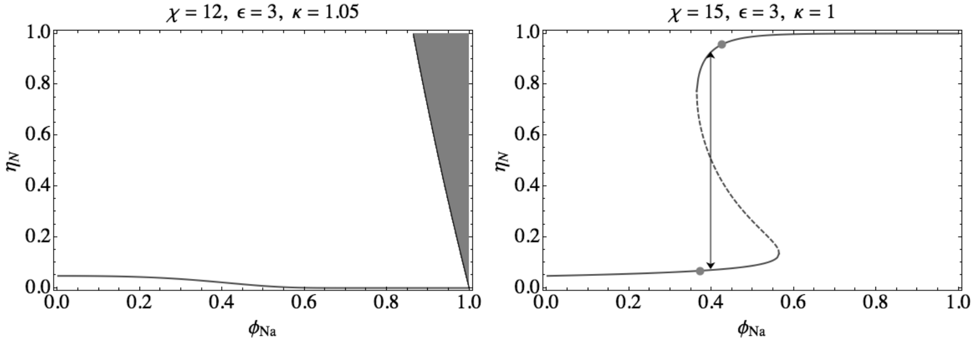

(a) (b)

Figure 4.3: The equilibrium fraction of proteins in the non-native state, $\eta_{\mathrm{N}}^{\mathrm{eq}}$, as a function of the protein concentration, ϕ_{Na}. Refer to the caption of fig. 4.2 for further details. For attractive interactions of strength $\chi = 15$ and a free energy penalty of $\epsilon = 3$. a) Size difference $\kappa = 1.05$. b) No size difference, $\kappa = 1$. The van der Waals-like loop that is shown has a different physical origin from the one shown in fig. 4.2b, see the main text.

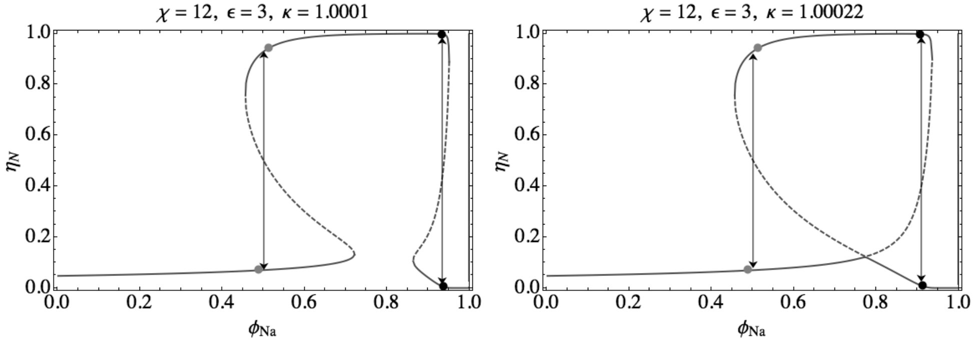

(a) (b)

Figure 4.4: The equilibrium fraction of proteins in the non-native state, $\eta_{\mathrm{N}}^{\mathrm{eq}}$, as a function of protein concentration, ϕ_{Na} for attractive interactions of strength $\chi = 15$ and a free energy penalty of $\epsilon = 3$. Refer to fig. 4.2 for further details. For a size difference a) $\kappa = 1.0001$ and b) $\kappa = 1.0002$.

)stable dispersion states with proteins mostly in their native state from a regime of (meta-)stable dispersion states with proteins mostly in their native state. See fig. 4.5. The dispersion state with most proteins in the non-native state is only stable in between the two first-order conformational phase transitions. Even though the structure appears to be quite different, the two first-order conformational phase transitions that we previously discussed still exist and the behaviour remains qualitatively the same.

Increasing κ further enhances self-crowding effects and causes the non-native state to be increasingly unfavourable and the concentration range over which it is stabilised decreases. This situations remains unchanged upto a critical value of κ at which the two first-order conformational phase transitions merge at a single value of ϕ_{Na}. In the next two sections we shall see that this corresponds to the "critical point" of two liquid-liquid phase separation transitions. For a further increase in κ, all of the dispersion states with proteins mostly in their non-native state on the upper $\eta_{\mathrm{N}}^{\mathrm{eq}}$ curve become meta-stable states, i.e., they have a higher free energy than the corresponding states at lower values of η_{N}. Increasing κ upto $\kappa = 1.05$ causes these meta-stable states to disappear altogether and the situation as shown in fig. 4.3a is retrieved.

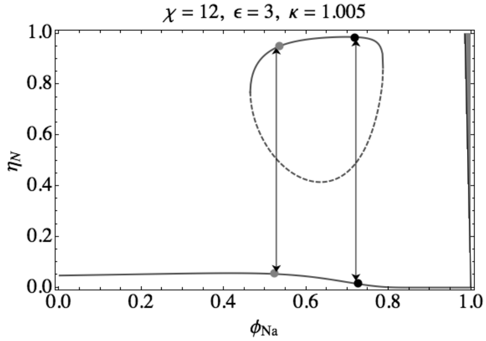

Figure 4.5: The equilibrium fraction of proteins in the non-native state, $\eta_{\mathrm{N}}^{\mathrm{eq}}$, as a function of protein concentration, ϕ_{Na} for $\chi = 15$, $\epsilon = 3$ and $\kappa = 1.005$. See fig. 4.2 for further details.

We have now covered all qualitatively different relationships between protein concentration and equilibrium conformation. The found dependence is the result of four different competing effects as discussed at the beginning of this section. In the next section we investigate in more detail under which circumstances phase separation can occur and if it occurs, what the composition of the coexisting phases is. There we shall see that the two types of van der Waals-like loop that we discovered in this section are intimately linked with two consecutive phase separations of the model dispersion with increasing concentration. In effect, we find re-entrant phase behaviour as we demonstrate in the next section.

4.4 Self-crowding induced phase separation

Phase separation occurs if the solution has a concentration in between the concentrations of two coexisting phases, as determined by the physico-chemical conditions of the solution. Under conditions of thermodynamic equilibrium temperatures are equal, the chemical potential of the proteins are equal and the osmotic pressure is equal. For the system at hand equal temperatures implies that χ and ϵ must be equal in the two phases. In the previous section we identified how to obtain the chemical potential and osmotic pressure from our free energy. The concentration and the average conformation of the protein in each of the two coexisting phases we determine numerically as a function of χ, ϵ and κ. In this section we show that two qualitatively different types of phase diagram present themselves.

We have determined the composition of coexisting phases for a variety of the model parameter values. We present these as phase diagrams, where the concentration, ϕ_{Na}, in each of the two coexisting phases is shown as a function of χ for a fixed value of ϵ and κ. By projecting the phase diagram onto the ϕ_{Na}-χ plane we do not explicitly consider the η_{N} direction. However, to get an impression of how the fraction of proteins in the non-native state varies across the phase diagram, we present cuts at fixed χ.

For a given value of κ, the two different types of phase diagrams that we find, are separated by a κ-dependent critical value of ϵ that we have not studied in depth. Let us first consider the class of phase diagrams for values of ϵ below this critical value. The phase diagram for $\kappa = 1.05$ and $\epsilon = 1.15$ is representative of this class and is shown in fig. 4.6a. The phase diagram shows two distinct regimes where phase separation occurs, the first is denoted by a solid curve, the second is denoted by a dashed line. For both binodal curves, the coexisting phases are joint by horizontal tie lines at constant χ. Note that phases on the solid curve do not coexist with phases on the dashed curve.

In the low-concentration regime phase separation results in a dilute phase of proteins in their native state and a dense phase of proteins in their non-native state. This is illustrated in fig. 4.6b showing the equilibrium fraction of proteins in the non-native state for $\chi = 20$ and where these two coexisting states are indicated by grey dots. Here, phase separation occurs because it is favourable to have a dilute phase of proteins in the native state and a dense phase of proteins mostly in their non-native state where attractive interactions compensate the free energy penalty for the transition to the non-native state.

In the high-concentration regime phase separation results in a relatively dilute phase of proteins mostly in their non-native state and a denser phase where proteins are mostly in their native state. This is indicated by the black dots in fig. 4.6b, which show the average conformational state in the coexisting phases. At high densities where a large fraction of the proteins are in the non-native, expanded state, the system runs out of free volume. To accomodate that, proteins will forgo their attractive interactions in favor of an increase in translational entropy by reverting to the smaller native state. Hence, phase separation is induced by self-crowding effects that can-

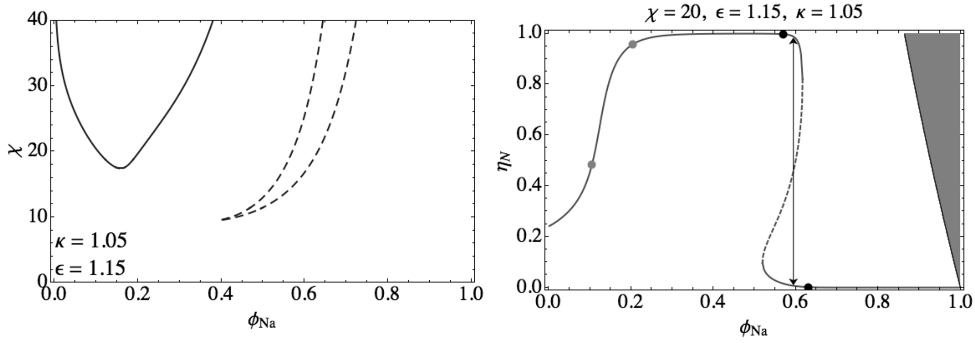

(a)

(b)

Figure 4.6: a) Phase diagram for $\kappa = 1.05$ and $\epsilon = 1.15$ showing two binodals. The solid curve denotes the protein concentration of coexisting phases that are joint by horizontal tie lines at constant χ. At higher protein concentrations there is a second regime where phase separation occurs, the dashed line also denotes the protein volume-fraction of coexisting states which are joint by horizontal tie-lines at constant χ. b) $\eta_{\text{N}}^{\text{eq}}$ as a function of ϕ_{Na} for $\kappa = 1.05$, $\epsilon = 1.15$ and $\chi = 20$ showing the two sets of two coexisting phases as grey and black dots respectively. The first-order conformational phase transition is indicated by the double-headed black arrow.

not be observed for $\kappa = 1$. Note that in this high-density regime, phase separation appears to be coupled to the underlying first-order conformational phase transition that we discussed in section 4.3 and as is shown in fig. 3.7b.

By labeling a phase as dilute relative to another phase, we mean that ϕ_{Na} is smaller in that phase, i.e., the number density of proteins is lower in the dilute phase. However, this does not mean that volume fraction in the dilute phase is smaller than that in the coexisting dense phase. This is indeed the case for the situation as shown in fig. 4.6b, while the phase with proteins mostly in their non-native state has $\phi_{\text{Na}} = 0.57$ and the phase with proteins mostly in their native state has $\phi_{\text{Na}} = 0.63$, the protein volume fraction in the first phase is $\phi = 0.66$ and in the latter phase it is $\phi = 0.63$.

Fig. 4.6 shows two more important characteristics of the phase behaviour of the model two-state protein dispersion. Firstly, fig. 4.6b shows that for values of ϕ_{Na} intermediate to the two regimes of phase separation, the non-native state is the more stable one. Secondly, the second regime of phase separation, indicated by the dashed binodal in fig. 4.6a, exhibits re-entrance, meaning that a continuous changes in temperature, and hence in χ,[1] leads to the transition from a homogeneous to a phase-separated and again to a homogeneous equilibrium state.

---

[1] χ is a free energy scaled to thermal energy, $k_B T$. Presuming that it contains a non-zero enthalpic contribution the value of χ must be temperature-dependent.

In fig. 4.7 we show the phase diagram for $\kappa = 1.25$ and $\epsilon = 2.17$, which is representative of the second class of phase diagrams as advertised above. Fig. 4.7a shows the phase diagram as a function of the protein concentration, ϕ_{Na}, which is a conserved quantity and fig. 4.7b that as a function of the protein volume fraction, ϕ, which is a non-conserved quantity. Again there are two concentration regimes where phase separation occurs, indicated by the solid and the dashed binodals, and coexisting phases are joint by horizontal tie lines at constant χ. For the first regime of phase separation, for the low-concentration branch the proteins are mostly in the native state while for the high-concentration branch the proteins are mostly in the non-native state. For the second regime, the opposite holds true.

As is evident from fig 4.7a, the two regimes of phase separation at low and high densities seem to merge at the lowest value of χ, in this case $\chi \approx 20$. However, when expressed in terms of ϕ instead of ϕ_{Na}, it transpires that the situation is more complex because the volume fractions of the coexisting phases do not merge into something that resembles a critical point. Hence, what appears to be a critical point in fig. 4.7a is not: the fraction of proteins in the non-native state remains different upon approach of the “critical point” where the concentrations become equal. This means that the phase gaps of both first-order phase transitions do not exhibit a critical end point. The transition remains first-order because it is connected to the first appearance of the first-order conformational transition described in the previous section. This is in contrast to the first class of phase diagrams discussed in the above, where the phase gap does end in an actual critical point.

At the “critical point” in fig. 4.7a both regimes of phase separation have one of the two coexisting phase where most proteins are in the native state and one where most proteins are in the non-native state. Interestingly, at the “critical point” the two regimes of phase separation can no longer be distinguished from each other, for the two coexisting phases in each of those two regimes are identical. As a consequence, for both regimes the protein volume fraction, ϕ, of the two coexisting phases is different at the “critical point”. the volume fraction , if the phase diagram is shown as a function of protein volume fraction, ϕ, as in fig. 4.7b, the “critical point” splits into two points at different protein volume fractions. In each of these points one of each of the branches of the binodal meet with one branch of the branches of the binodal of the other regime of phase separation meets, i.e., a solid and dashed line meet in these points, see fig. 4.7b.

In the second class of phase diagrams, both liquid-liquid phase separations turn out to be coupled to underlying first-order conformational phase transitions of the proteins themselves. This is how the second class of phase diagrams appears to set themselves apart from the first class, where only the high-density phase separation is coupled to this underlying conformational phase transition. We illustrate this in fig. 4.8 where the composition of the coexisting phases of both regimes of phase separation and the location of the underlying first-order conformational phase transitions are shown for $\chi = 23$ and $\chi = 30$.

Let us now briefly return to the phase diagrams shown in fig. 4.7b and focus on the region just above and in between the two “critical points”. From this figure, we might

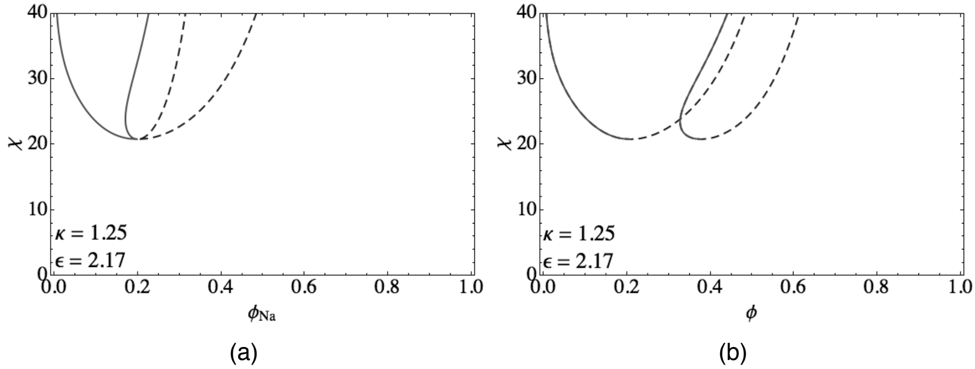

Figure 4.7: a) Phase diagram for $\kappa = 1.25$ and $\epsilon = 2.17$ showing two binodals. The solid curve denotes the protein concentration of coexisting phases that are joint by horizontal tie lines at constant χ. At higher protein concentrations there is a second regime where phase separation occurs, the dashed line also denotes the protein concentration of coexisting states which are joint by horizontal tie-lines at constant χ. b) The same phase diagram, but now shown as a function of protein volume-fraction, ϕ. Coexisting states are joint by horizontal tie-lines, however because ϕ is not a conserved order parameter interpretation of this phase diagram is difficult.

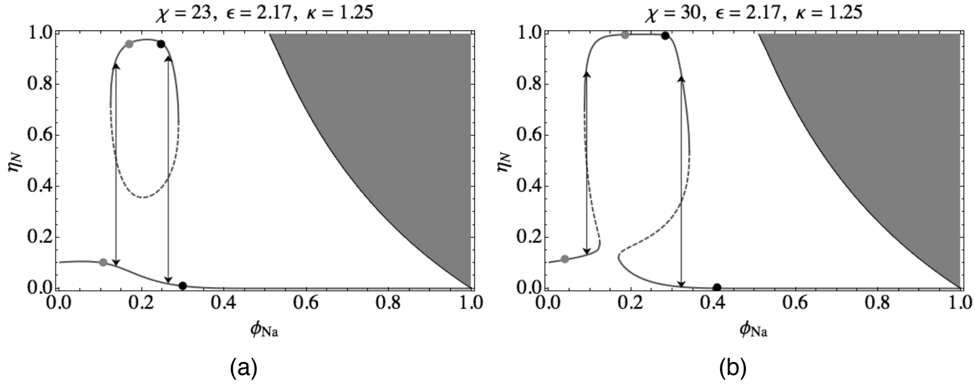

Figure 4.8: a) $\eta_{\rm N}^{\rm eq}$ as a function of $\phi_{\rm Na}$ for $\kappa = 1.25$, $\epsilon = 2.17$ and $\chi = 23$ showing the two sets of two coexisting states as grey and black dots respectively. The first-order conformational phase transition is indicated by the double-headed black arrow b) The same type of graph, but for $\kappa = 1.25$, $\epsilon = 2.17$ and $\chi = 30$.

conclude that for these protein volume fractions both regimes of phase separation are accessible as the protein volume fraction is intermediate to the protein volume fractions of the coexisting phases of both regimes of phase separation. However, this interpretation is incorrect, protein volume fraction is a non-conserved quantity and the two regimes of phase separation occur at different protein concentrations that do not overlap, see fig. 4.7a. Protein concentration, ϕ_{Na}, is a conserved order quantity and hence, it must be conserved during phase separation. As a consequence, the phase diagram as shown in fig. 4.7a must be used to determine if phase separation can occur, and if it occurs what the composition of the two coexisting phases are and not the one shown in fig. 4.7b.

For other values of ϵ and κ the phase diagram is qualitatively similar to either the phase diagram as shown in fig. 4.6a or fig. 4.7a and hence, in the above a comprehensive qualitative discussion of the model's phase behaviour was given. In the next section we provide a discussion of the results that we have presented.

4.5 Discussion

In this chapter we present a model for protein liquid-liquid phase separation in which protein conformation is not conserved and where there is an equilibrium between an inert native conformation and an excited, expanded non-native conformation, which is not only larger in size but also interacts attractively with proteins with the same conformation. Our calculations show that volume exclusion stabilizes the native state at high protein concentrations due to self-crowding (free-volume) effects. We find that there are two different first-order conformational phase transitions at fixed protein concentration. These first-order conformational phase transitions are coupled to two different regimes of liquid-liquid phase separation, where the regime at higher protein concentration is induced by self-crowding. Interestingly, the underlying physics of the phase separations and the first-order conformational phase transitions, hidden behind the associated liquid-liquid phase separation, is identical.

In our theory we see two clear effects that are caused by self-crowding, which itself is caused by the larger volume of the non-native conformation that reduces the free volume of the solution. These effects are the stabilisation of the native state at high protein concentration and the presence of a second regime of phase separation at high protein concentrations. This is superficially different from the effects of more conventional cases of macromolecular crowding where crowding agents are added to a protein solution leading to either phase separation or aggregation depending on the specific interaction between the proteins. Here too, a decrease in free volume drives these processes.[17,109] The crucial difference of course is that in our case free volume is primarily linked with the volume the particles themselves take up whereas in the more conventional case it is linked to mutual excluded volume of groups of particles.

An obvious question is how the predictions of the model compare with experimental observations on liquid-liquid phase separation in protein dispersions. To our knowledge, protein dispersions only display one regime of phase separation, rather than the two predicted by our model.[75,78] A possible reason for this is that the second regime of phase separation occurs at protein concentrations where the solution gels or crystallizes.[22] Neither of these effects are included in our model as we focus on the consequences of self crowding on liquid-liquid phase separation. However, we expect similar effects to be relevant to crystallization especially since the structure of crystals is largely determined by excluded-volume effects.[114]

One interesting feature of the model is that protein volume fraction is a non-conserved quantity, which, as we have seen, leads to unusual phase behaviour. A consequence of this that we so far have not addressed relates to the nature of the spinodal, i.e., the limit of stability of a homogeneous dispersion. The stability is determined by the local curvature of the free energy and the spinodal coincides with points where, for a multi-order parameter system, the determinant of the Hessian vanishes. However, for our model, the location of inflection points in the free energy landscape depends on the choice of order parameters, that is, ϕ_{Na} and η_{N} or ϕ and η. The question is then, too the inflection points for which set of these parameters does the spinodal correspond? To answer this question, we must realise that from a thermodynamic point of view, the spinodal must correspond to the point where fluctuations in the number density of proteins in the native and proteins in the non-native state become unstable. Using this as as starting point we find that the spinodal is given by inflection points in the free energy landscape in ϕ-η representation.

A consequence of this is, is that in general the spinodal and binodal do not meet in the critical point. In previous work, we showed that this also holds true for the situation where both conformations are of equal volume and are separated by a sufficiently large difference in free energy. This also holds true for the model presented here, however, because in the model presented here there are two first-order conformational phase transitions, rather than just one as for the model presented in chapter 3 ($\kappa = 1$), the interdependence between protein conformation, number-density and the stability of the dispersion is highly non-universal and complex and hence beyond the scope of this chapter.

In summary, we have shown that changes in effective protein volume induced by switching between the native and a non-native state strongly affect the phase behaviour. The corresponding self-crowding effects lead to stabilization of the native state at high protein concentrations and cause the appearance of a regime of phase separation at high concentration.

Chapter 5

Anomalous kinetic processes in a model two-state protein dispersion

Summary

In this chapter we investigate the non-equilibrium behaviour of the model two-state protein dispersion introduced in chapter 3. We perform a linear stability analysis on a set of model-C-like kinetic equations using a square-gradient free energy functional. The stability analysis suggests that initially relaxation occurs by either of three different modes. These modes are, 1) a classic spinodal decomposition mode, 2) a mode in which the protein conformation relaxes towards equilibrium over the entire system simultaneously and 3) a mode that involves the scale-free phase separation of the model dispersion in such a manner that the local concentration of proteins in the non-native state is conserved. Based on these three modes we discuss the relaxation from a number of different non-equilibrium states towards equilibrium.

5.1 Introduction

In this chapter we investigate the kinetic consequences of the coupling of changes in protein conformation to the phase separation of a protein dispersion. To this end, we investigate the non-equilibrium processes that can occur in a model two-state protein dispersion in which proteins can reversibly switch between their native and a single non-native conformation. Whilst in a model mixture of solvent and proteins with fixed conformation phase separation proceeds either by spinodal decomposition or by nucleation and growth, the kinetics are more complex when there is a coupling to changes in the conformation of the protein. In this situation, non-equilibrium processes can involve changes both in local protein concentration and conformation. Nonetheless, both the concept of spinodal decomposition and nucleation and growth remain useful in the analysis of the non-equilibrium processes in the model dispersion.

Before we address the non-equilibrium behaviour of the model two-state protein dispersion, which we introduced in chapter 3, we briefly repeat the properties of the model and review the most important aspects of the equilibrium behaviour. The model proteins can reversibly switch between their native and a high-energy non-native conformation, where the transition to the non-native state involves a free energy penalty of ϵ (in units of thermal energy, $k_B T$) per protein. The model proteins are presumed to be of equal size and shape and interact through excluded volumes regardless of their conformation. Proteins in the non-native state can engage in attractive interactions of strength χ (in units $k_B T$) with other nearby proteins that are also in the non-native conformation. The state of the model dispersion is specified by the protein volume fraction, ϕ, and the number fraction of proteins in the non-native state, η. The equilibrium behaviour of this model exhibits a demarcation between a regime of weak coupling and a regime of strong coupling between changes in conformation and phase separation, where the coupling becomes strong due to the presence of an underlying first-order conformational phase transition. We briefly address the difference between these two regimes in more detail in sections 5.5 and 5.6 and refer the reader to chapter 3 for a detailed discussion.

The coupling of phase separation to protein conformation has two immediate consequences for the non-equilibrium behaviour. Firstly, the protein self-diffusion time is no longer the only time scale involved, as non-equilibrium processes are in our case also dependent on the time scale at which conformational changes in the protein can occur. Secondly, the non-equilibrium behaviour is no longer exclusively restricted to the transition between homogeneous and heterogeneous dispersion states, processes that only involve changes in the average conformation of the proteins are also possible in our model dispersion. We investigate such relaxation modes for the weak-coupling regime in detail in section 5.5 where we show that such processes can involve *temporary* phase separation. In section 5.6 we investigate the kinetics by which phase separation occurs in the strong-coupling regime where the coexisting phases are separated by an underlying first-order conformational phase transition.

To analyse the non-equilibrium behaviour we introduce in section 5.2 a pair of model-C-type kinetic equations for the protein concentration and the protein conformation,[92] as well as a free energy functional that incorporates both non-local and local contributions to the free energy. The non-local contribution consists of a square-gradient term[115] while the local free energy is based on a combination of mean-field arguments and the Carnahan-Starling equation of state.[91]

In sections 5.3 and 5.4 we perform a linear stability analysis on the kinetic equations and determine the different eigenmodes by which the relaxation from a non-equilibrium state initially proceeds. In sections 5.5 and 5.6 we use the linear stability analysis to investigate the stability and relaxation modes for the weak-coupling and the strong-coupling regime respectively. In section 5.7 we discuss the results that we present in this chapter.

5.2 Model

We model the non-equilibrium behaviour of the two-state protein dispersion by presuming model-C-type kinetics.[92] The free energy of the dispersion is modeled by a free energy functional that includes local and non-local contributions. The local free energy includes a contribution that reflects the properties of the model two-state proteins, and a Carnahan-Starling based contribution[91] to take excluded-volume effects into account. For the non-local contribution we use a single square-gradient term[115] to penalize gradients in the concentration of non-native proteins. We omit the square-gradient terms involving proteins in the native state both for simplicity and because the interfacial stiffness of a Carnahan-Starling hard-sphere fluid is negative and hence unphysical.[116]

Introduction of the dimensionless time, $\tau = \Gamma t$, where Γ^{-1} is a measure for the time scale at which the conformation of the proteins change, and the dimensionless distance $\vec{x} = \vec{r}/\sqrt{k}$, where $\sqrt{k}$ is a measure of the interfacial "stiffness" between different phases in the dispersion, allows for a reduced non-dimensional representation of the kinetic equations. Within this representation the kinetic equation for the local protein volume fraction, ϕ, which is a conserved quantity reads,[92]

$$\partial_\tau \phi = \alpha \vec{\nabla}_x \cdot \left(\phi \vec{\nabla}_x \mu \right) + \zeta, \tag{5.1}$$

where $\alpha = D/\Gamma k$ is the ratio of the conformational relaxation time to the protein self-diffusion time, with D the protein self-diffusion constant, $\mu = \delta_\phi F$ is the chemical potential of the proteins in units of thermal energy ($k_B T$), given by the functional derivative of the free energy density functional F with respect ϕ. The final term, ζ is a Gaussian white-noise term with zero mean and covariance $\langle \zeta(\vec{x}, \tau) \zeta(\vec{x}', \tau') \rangle = 2\alpha\phi\vec{\nabla}_x^2 \delta(\tau - \tau') \delta(\vec{x} - \vec{x}')$. The time evolution of the local average protein conformation, η, which is a non-conserved quantity is given by,[92]

$$\partial_\tau \eta = -\delta_\eta F + \theta, \tag{5.2}$$

where $\delta_\eta F$ is the functional derivative of the free energy density functional, F, with respect to η and θ is again a Gaussian white-noise term with zero mean and covariance $\langle \theta (\vec{x}, \tau) \, \theta (\vec{x}', \tau') \rangle = 2\delta (\tau - \tau') \, \delta (\vec{x} - \vec{x}')$.

The dimensionless free energy density functional, in units of thermal energy is given by

$$F \left[\phi (\vec{x}, \tau) , \eta (\vec{x}, \tau) \right] = \int d\vec{x} \left(f + \frac{1}{2} \left(\vec{\nabla}_x \phi \eta \right)^2 \right), \tag{5.3}$$

where f is the local dimensionless free energy density,

$$f = \eta\phi \ln \eta\phi + (1 - \eta) \, \phi \ln (1 - \eta) \, \phi - \phi + \frac{\phi^2 (4 - 3\phi)}{(1 - \phi)^2} + \epsilon\eta\phi - \frac{\chi}{2} (\eta\phi)^2 , \tag{5.4}$$

where χ is a measure for the strength of the attractive interactions between proteins in the non-native state and ϵ is the free energy difference between the native and non-native conformation of the protein. Both free energy parameters are in units of thermal energy.

In summary, in reduced representation the model consists of two order parameters, ϕ, which denotes the protein volume fraction and η, the number fraction of proteins in the non-native state. Solution conditions and protein properties are reflected in the value of two free energy parameters, being χ, which is a measure of the strength of attractive interactions between proteins in the non-native state, and ϵ, which denotes the free energy difference between the non-native and native conformation of the protein. The final model parameter, α, is the ratio of the conformational relaxation time of the protein to the protein self-diffusion time. In the remainder of this chapter we report on the results of a linear stability analysis for this model, where we show that a number of anomalous relaxation modes exist.

5.3 Linear stability analysis

To gauge the stability of different compositions of the model dispersion, we perform a linear stability analysis. From the results of this analysis we determine under which circumstances the dispersion is thermodynamically unstable and what the initial typical time and length scales are at which the instabilities grow. The results show that there are three different relaxation modes, one of which is the usual spinodal decomposition,[115] one of which involves global relaxation of protein conformation and one of which involves a length-scale free relaxation of both protein concentration and conformation where the local concentration of proteins in the non-native state is conserved.

The relaxation modes can be determined by first dropping the Gaussian white noise terms from eqs. (5.1) and (5.2). After subsequent linearisation in ϕ and η around the initial values (ϕ_0, η_0) and Fourier transformation, the resulting set of equations can be written as a simple matrix equation of which the resulting two eigenmodes, $\vec{m}_{\pm}$, and two eigenvalues, $\lambda_{\pm}$, can be determined,

$$\lambda_{\pm} = \frac{A+D}{2} \pm \frac{\sqrt{(A-D)^2 + 4BC}}{2}, \tag{5.5}$$

$$\vec{m}_{\pm} = \left(\frac{A-D}{2C} \pm \frac{\sqrt{(A-D)^2 + 4BC}}{2C}, 1 \right), \tag{5.6}$$

where A, B, C and D are given by,

$$A = -\alpha\xi^2 \left(\phi_0 f_{\phi\phi} + \phi_0 \eta_0^2 \xi^2 \right), \tag{5.7}$$

$$B = -\alpha\xi^2 \left(\phi_0 f_{\phi\eta} + \phi_0^2 \eta_0 \xi^2 \right), \tag{5.8}$$

$$C = -\left(f_{\phi\eta} + \eta_0 \phi_0 \xi^2 \right), \tag{5.9}$$

$$D = -\left(f_{\eta\eta} + \phi_0^2 \xi^2 \right), \tag{5.10}$$

where ξ is the absolute value of $\vec{\xi}$, which is the dimensionless momentum transfer (wave vector) conjugate to the dimensionless positional degree of freedom, $\vec{x}$ and f_{ij} denotes the derivative of the local free energy, eq. (5.4), with respect to i, j and where i, j are either ϕ or η. The initial response to any fluctuation or perturbation, $(\Delta\phi(\xi), \Delta\eta(\xi))$ of momentum transfer $2\pi\xi^{-1}$ can be decomposed into the two eigenmodes $\vec{m}_{\pm}(\xi) = (\Delta\phi_{\pm}(\xi), \Delta\eta_{\pm}(\xi))$. These eigenmodes grow exponentially over time if $\lambda_{\pm}(\xi) > 0$ and decay exponentially over time if $\lambda_{\pm}(\xi) < 0$. Note that this result only holds true for $|\vec{\xi}| \neq 0$ and immediately after occurrence of the fluctuation or application of the perturbation.

The result of the stability analysis is the following: a dispersion of composition ϕ_0, η_0 is stable in regards to any small fluctuation or perturbation if $\lambda_{\pm}(\xi) \leq 0$ for all $\xi > 0$. If $\lambda_{\pm}(\xi) > 0$ for any ξ, the dispersion is thermodynamically unstable. The typical length scale at which the instability grows is $2\pi\xi_{\mathrm{max}}^{-1}$ and the difference in protein concentration and conformation between the domains grows exponentially at a time scale $\lambda_{\pm}(\xi_{\mathrm{max}})^{-1}$. Here, ξ_{max} denotes the value of ξ for which $\lambda_{\pm}(\xi)$ is at a maximum.

As previously mentioned, this results strictly only holds for $\xi \neq 0$. This is so, because for $\xi = 0$ the linearised kinetic equation for the protein conformation involves a term $-f_{\eta}\delta(\xi)$, which renders the associated differential equation inhomogeneous for $\xi = 0$ and prehibits one to write the set of kinetic equations as a matrix equation, with the associated eigenmodes and eigenvalues as given by eqs. (5.5), (5.6) and (5.7). Only for $\xi \neq 0$ and $\delta(\xi \neq 0) = 0$ this term drops out and the homogeneous kinetic equations of which we determined the corresponding eigenmodes and eigenvalues are retrieved.

Let us now consider the case where perturbations and fluctuations are of wavelength $\xi = 0$, i.e., those of infinite length scale. For a *conserved* order parameter perturbations and fluctuations with $\xi = 0$ do not grow or decay as they involve transport over an infinite length scale, which is infinitely slow. In agreement with this we find that any eigenmode, $\vec{m}_\pm(\xi = 0) = (\Delta\phi_\pm(0), \Delta\eta_\pm(0))$, with $\Delta\phi_\pm(0) \neq 0$ has an eigenvalue $\lambda_\pm(0) \leq 0$. However, an eigenmode $(0, 1)$ can have a non-zero eigenvalue as the mode does not involve mass transport, meaning that global relaxation of protein conformation can occur.

From the linear stability analysis, and without the presumption $\xi \neq 0$, we find that this mode has the following time evolution,

$$\delta\eta(\tau) = \left(\delta\eta_0 + f_\eta/f_{\eta\eta}\right) \exp\left[-f_{\eta\eta}\tau\right] - f_\eta/f_{\eta\eta}. \tag{5.11}$$

From this equation, it follows that any dispersion state with $f_{\eta\eta} < 0$ is unstable, resulting in a system-wide relaxation of η ($\xi = 0$). Note, however, that this is the result of a linear stability analysis. An analysis of the full non-linear kinetic equations should reveal that any dispersion state, except for those where the free energy is at a minimum with respect to η at the fixed initial concentration, must be unstable with respect to fluctuations in η. The average protein conformation, η, is a non-conserved quantity and hence the average protein conformation, η, should always spontaneously relax to a value corresponding to a (local) minimum in the free energy.

5.4 Eigenmodes

In the previous section we performed a linear stability analysis and determined the eigenmodes and corresponding eigenvalues by which the model two-state dispersion initially reacts to small perturbations and fluctuations. There, we briefly mentioned that a distinction between three different eigenmodes by which instabilities grow can be made, these modes are: classic spinodal decomposition, a mode that involves the scale-free relaxation of both protein concentration and conformation while the local concentration of proteins in the non-native state is conserved and finally a mode that involves the global relaxation of protein conformation. Here we derive mathematically under which circumstances, i.e., for which values of the model parameters, these modes are active. In the next two sections we consider explicitly when these modes are active as a function of ϕ and η for several different values of χ, ϵ and α. There, we shall see that the activity of these modes is restricted to the areas that we previously identified as being thermodynamically unstable in chapter 3.

The system is unstable for conditions under which there is a positive maximum eigenvalue of the mobility matrix, $\lambda_\pm(\xi = \xi_{\text{max}})$. In that case, the instability grows at a time scale proportional to $2\pi{\xi_{\text{max}}}^{-1}$ and an associated length scale, $2\pi{\xi_{\text{max}}}^{-1}$, predominates in the initial stages of spinodal decomposition. Interestingly, for the local free energy as given by eq. (5.4), $\lambda_-(\xi)$ is negative for all values of the model parameters and the three different relaxation modes are found at different values of ξ for $\lambda_+(\xi)$. In the following, we discuss under which conditions each of these three modes is active.

The first of the three modes that we discuss involves the global relaxation of protein conformation. By substitution of $\xi = 0$ in eqs. (5.5) and (5.6), we find that for $\xi = 0$ and $f_{\eta\eta} < 0$, $\lambda_+(\xi = 0) = -f_{\eta\eta}$ is positive. Furthermore we find that the corresponding eigenmode is $\vec{m}_+ = (0,1)$, and hence it involves changes in protein conformation only and does not involve mass transport. Or, in short if $f_{\eta\eta} < 0$,

$$\begin{aligned} \lambda_+(\xi = 0) &= -f_{\eta\eta}, \\ \vec{m}_+(\xi = 0) &= (0,1). \end{aligned} \tag{5.12}$$

The value of $\lambda_+(\xi = 0)$ is independent of α, the ratio of the conformational relaxation time to the protein self-diffusion time. This is indeed what one expects, because the mode only involves relaxation of protein conformation and the unit of time, τ, is normalised by the protein conformational relaxation time. The relaxation process predicted by eq. (5.12) is in agreement with the predictions of eq. (5.11).

An example of the situation where the $\lambda_+(\xi = 0)$ is the dominant mode is shown in fig. 5.1, where the value of $\lambda_+(\xi)$ is plotted. It shows that λ has a maximum for $\xi = 0$ and that $\lambda_+(\xi)$ remains positive up to approximately $\xi = 2.24$. Note, that for $\xi > 0$ the modes become increasingly slower with decreasing length scale (increasing ξ) and that these modes are hence not dominant.

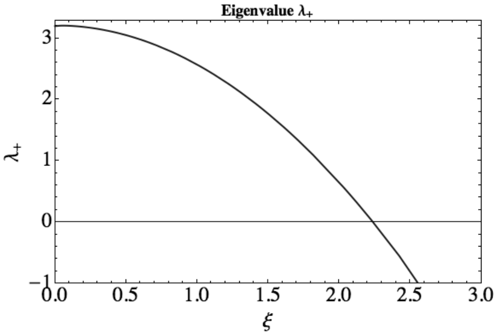

Figure 5.1: The eigenvalue λ_+ as a function of ξ for $\phi_0 = 0.8$, $\eta_0 = 0.5$, $\chi = 10$, $\epsilon = 1$ and $\alpha = 1$. It has a maximum of $\lambda_+(0) = 3.2$ for $\xi = 0$ where the corresponding eigenvector is $\vec{m}_+ = (0,1)$, implying that the average protein conformation relaxes globally at a time scale proportional to $\lambda_+(0)^{-1}$.

Next we consider the other extreme, i.e., eigenmodes with a positive maximum at a vanishingly small length scale, which corresponds to the limit $\xi \to \infty$. Usually, such modes also yield an eigenvalue of 0, because fluctuations at a vanishingly small length scale generate infinite gradients which lead to a diverging contribution of the square-gradient term to the free energy functional of the system, eq. (5.3). Moreover, fluctuations at very large values of ξ, and hence at very small length scales, become meaningless when these lengths approach the dimensions of a single protein. Interestingly, the linear stability analysis predicts that under certain circumstances λ_+ has a positive value in the limit $\xi \to \infty$ and that it retains this value over a large range in ξ, suggesting that relaxation is equally fast at all these length scales.

As we shall see, such a mode can exist within our model because it does not lead to a divergence of the non-local contribution to the free energy functional, eq. (5.3). Furthermore, our theory only implicitly takes the size of the protein into account, hence the model is blind to the minimum length scale at which any fluctuation can occur.

An example of the situation where this mode is dominant is shown in fig. 5.2, where the value of $\lambda_+(\xi)$ is plotted. The existence of this mode can be shown by taking the limit $\lim_{\xi\to\infty}\lambda_+(\xi)$ and $\lim_{\xi\to\infty}\vec{m}_+(\xi)$ and applying l'Hôpital's rule. The resulting eigenvalue and eigenmode are,

$$\begin{aligned} \lambda_+(\xi\to\infty) &= \left(2\eta\phi f_{\phi\eta} - \phi^2 f_{\phi\phi} - \eta^2 f_{\eta\eta}\right)/\eta^2, \\ \vec{m}_+(\xi\to\infty) &= (-\phi,\eta)/\sqrt{\phi^2+\eta^2}. \end{aligned} \tag{5.13}$$

Note that the eigenvalue and eigenmode are again independent of α. This is to be expected because the limit $\xi\to\infty$ corresponds to fluctuations over infinitely small length scales. At infinitisimal length scales, mass transport occurs instantaneously and hence the protein self-diffusion time scale is irrelevant. The time scale at which this mode operates is then the time scale to which we scaled the dimensionless time τ, i.e., the time scale at which conformational relaxation occurs.

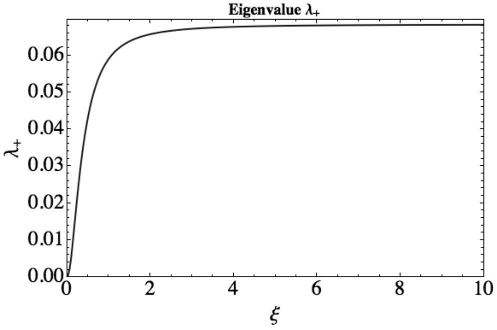

Figure 5.2: The eigenvalue λ_+ as a function of ξ for $\phi_0 = 0.04$, $\eta_0 = 0.5$, $\chi = 10$, $\epsilon = 3$ and $\alpha = 1$. It has a maximum of $\lambda_+ = 0.068$ for $\xi \to \infty$ where the corresponding eigenvector is $\vec{m}_+ = (-0.079, 0.997)$. A detailed explanation of the non-equilibrium behaviour corresponding to this eigenmode is given in the main text.

We mentioned that the non-local square-gradient contribution to the free energy should prohibit a non-zero value of $\lambda_+(\infty)$ because any such mode generates infinite gradients. The reason as to why we do find a non-zero value of $\lambda_+(\infty)$ lies in the definition of the free energy functional, eq. (5.3), and the eigenmode, eq. (5.13). If the eigenmode $\vec{m}_+(\infty)$ is plotted as a vector field as a function of ϕ_0, η_0, i.e., the initial protein concentration and conformation, then the corresponding field lines are such that along them, the concentration of proteins in the non-native state is conserved. Indeed, these field lines are given by $\partial\eta/\partial\phi = -\eta/\phi$ and integration by separation of variables shows that $\eta\phi$ is a conserved quantity on these field lines. Hence the eigenmode is a mode under which the local concentration of proteins in the non-native state is conserved. As a consequence, this mode does not produce a gradient in the concentration of proteins in the non-native state and because the free energy functional, eq. (5.3), only involves a square-gradient term that penalises a gradient in the concentration of proteins in the non-native state, this mode can occur.

Note that we only include this single square-gradient term in our free energy functional because the interfacial stiffness of a Carnahan-Starling hard-sphere fluid is negative and thus unphysical.[116] Furthermore, it reduces parameter space and thereby simplifies the analysis of the model system which already displays highly non-universal behaviour. Nonetheless, one could easily argue that this mode is an artifact of our model. While this makes it perhaps less relevant from a practical point of view, it remains interesting from a theoretical perspective.

The final mode is a spinodal decomposition mode where $\lambda_+(\xi)$ has a well defined maximum at a finite, non-zero value of $\xi = \xi_{\text{max}}$. Unfortunately, we cannot analytically determine the position and value of this maximum because finding the roots of the derivative of $\lambda_+(\xi)$ with respect to ξ involves solving a seventh order polynomial in ξ, which must be solved by numerical means. However, it is possible to derive an analytic criterion that must hold for a possible spinodal mode to exist. Indeed, the second derivative $\partial_{\xi\xi}\lambda_+(\xi)$ must at the least be positive at $\xi = 0$ to produce a positive maximum. This holds true when,

$$\begin{array}{ll} \phi + \alpha f_{\phi\eta}^2/f_{\eta\eta} < 0, & f_{\eta\eta} < 0 \\ f_{\phi\phi}f_{\eta\eta} < f_{\phi\eta}^2, & f_{\eta\eta} > 0. \end{array} \tag{5.14}$$

Because $\lambda_+(0) \geq 0$ this indeed guarantees the existence of a positive maximum value of $\lambda_+(\xi)$ that is necessarily larger than $\lambda_+(0)$. However, when the inequalities in both eq. (5.13) and eq. (5.14) hold, it is possible that the maximum value of $\lambda_+(\xi)$ is obtained in the limit of $\xi \to \infty$, see fig. 5.2. Whether this is indeed the case can be checked by determining the sign of the first derivative, $\partial_\xi\lambda_+(\xi)$ at some large, but finite value of ξ. If this derivative is negative then $\lambda_+(\xi)$ has a positive maximum at some finite value of ξ. A situation where all of this is the case is shown in fig. 5.3.

A few additional remarks are in order. Firstly, we have not determined the values of ξ_{max}, $\lambda_+(\xi_{\text{max}})$ and $\vec{m}_+(\xi_{\text{max}})$ as a function of the remaining model parameters. In principle the values of these parameters depends on the value of α, meaning that the manner in which an instability grows is not only determined by the local free energy landscape, but is also determined by the different time scales at which changes in ϕ and η occur. Secondly, the boundary of the region where the second inequality of eq. (5.14) holds ($f_{\eta\eta} > 0$ and $f_{\phi\phi}f_{\eta\eta} < f_{\phi\eta}^2$), is given by inflection lines in the free energy surface. These are given by points where the determinant of the Hessian equals zero. Note that this inequality holds at all times provided $f_{\phi\phi} < 0$ because $f_{\eta\eta} > 0$ and $f_{\phi\eta}^2 \geq 0$. This is not surprising, because $f_{\phi\phi} < 0$ implies that the local free energy is concave in the ϕ-direction, and this is the classic criterion for spinodal decomposition to occur in for example a binary mixture.

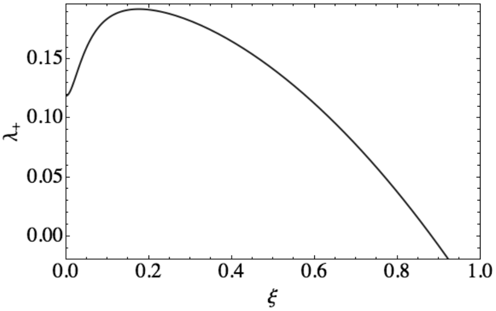

Figure 5.3: The eigenvalue λ_+ as a function of ξ for $\phi_0 = 0.5$, $\eta_0 = 0.7$, $\chi = 10$, $\epsilon = 3$ and $\alpha = 1$. It has a maximum of $\lambda_+ = 0.192$ for $\xi_{\mathrm{max}} = 0.176$ where the corresponding eigenvector is $\vec{m}_+ = (0.025, 0.999)$. A detailed explanation of the non-equilibrium behaviour corresponding to this eigenmode is given in the main text.

Previously we mentioned that $\lambda_-(\xi)$ is negative at all times for the Carnahan-Starling based local free energy, eq. (5.4). This does not necessarily hold for other local free energies. So, let us in a more general case consider when $\lambda_-(\xi)$ has a well defined maximum at a finite non-zero value of ξ. Because $\lambda_-(0) \leq 0$ and $\lambda_-(\infty) \to -\infty$ a positive maximum can exist when $\partial_{\xi\xi}\lambda_-(\xi)$ is positive for $\xi = 0$. This is the case when

$$f_{\eta\eta} < 0 \;\text{ and }\; f_{\phi\phi}f_{\eta\eta} > f_{\phi\eta}^2. \tag{5.15}$$

if eq. (5.15) holds, $\lambda_-(0) = 0$ also applies, so a positive maximum must indeed exist under these conditions. Note that for the inequality in eq. (5.15) to hold, $f_{\phi\phi} < 0$ is a necessary condition. This implies that the local free energy is convex in the ϕ-direction. This is opposite to the criterion for spinodal decomposition to occur in a binary mixture, which might explain why this mode is never observed for our Carnahan-Starling-based model free energy.

In the next sections, sections 5.5 and 5.6, we shall take a more practical approach and consider the phase behaviour for $\epsilon = 1$ and $\epsilon = 3$, which are representative of the weak-coupling and strong-coupling regime respectively, as introduced in chapter 3. For these values of ϵ we investigate for which dispersion compositions ϕ_0, η_0 the different modes are active.

5.5 Phase and stability behaviour in the weak-coupling regime

We have established the theoretical framework that is required to analyse the stability and non-equilibrium behaviour of the model dispersion. In this section, we discuss the equilibrium phase and stability behaviour, and the expected non-equilibrium behaviour for the situation $\epsilon \leq 2$. In section 5.6 we perform a similar analysis for the situation $\epsilon > 2$. We discuss the situations for $\epsilon \leq 2$ and $\epsilon > 2$ separately for $\epsilon = 2$ demarcates the regimes of so-called weak coupling and strong coupling between phase separation and conformational changes. In chapter 3 we addressed the equilibrium properties of both regimes in detail and speculated on the relevant kinetic regimes, in this section and in section 5.6 we briefly review these.

We now turn to the phase and stability diagram for $\epsilon = 1$, which is representative of the weak-coupling regime and shown in fig. 5.4.

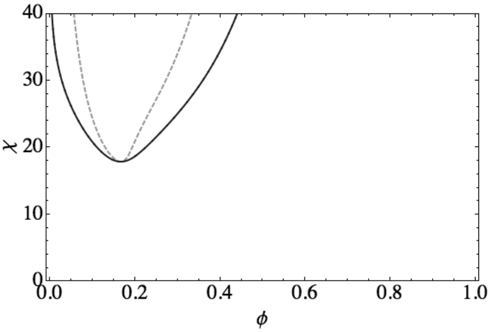

Figure 5.4: The phase and stability diagram for $\epsilon = 1$ (the free energy difference between the native and non-native state of the protein, in units of $k_B T$) for the dimensionless local free energy density as given by eq. (5.4). The binodal is shown by the solid line and coexisting states are joint by horizontal tie lines at constant value of χ (the strength of attractive interactions between proteins in the non-native state, in units of $k_B T$), while the dashed line depicts the "equilibrium" spinodal. In the main text we discuss this concept in more detail.

The phase diagram as shown in fig. 5.4 superficially appears to be conventional. It should however be noted that this diagram is a projection onto the ϕ-χ plane, that is, the average protein conformation, η, of the coexisting phases is not shown. Secondly, it should be noted that we defined an "equilibrium" spinodal that is slightly different from the conventional spinodal. This somewhat unconventional definition is a consequence of the coupling of protein concentration and conformation in the model system. We can investigate both of these aspects by considering the phase and stability behaviour as a function of ϕ and η for fixed value of χ and ϵ. For $\epsilon = 1$ we do so for $\chi = 10$, fig. 5.5a, and for $\chi = 25$, fig. 5.5b.

A detailed explanation of the graphs in fig. 5.5 can be found in the caption of the figure. As previously mentioned, fig. 5.5 provides additional insight into the nature of the coexisting phases and "equilibrium" spinodal points as shown in the phase diagram for $\epsilon = 1$, fig. 5.4. The phase diagram, fig. 5.4, indicates that $\chi = 10$ lies below the critical point and in accordance with this, the graph in fig. 5.5a contains no binodal or "equilibrium" spinodal points. For $\chi = 25$ we are above the critical point and

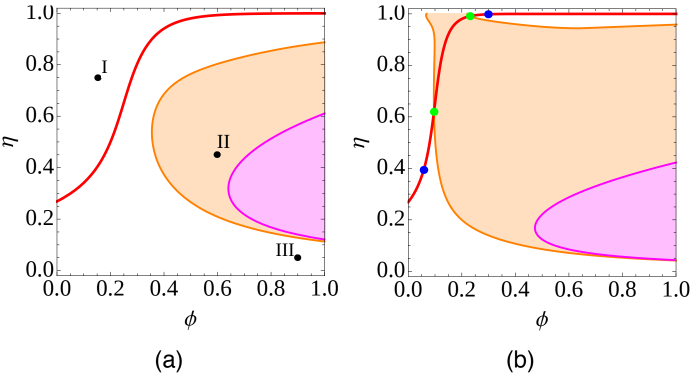

(a) (b)

Figure 5.5: Summary of the equilibrium and stability behaviour of the model protein dispersion as a function of protein volume fraction, ϕ, and average protein conformation, η, for a free energy difference between the native and non-native state of $\epsilon = 1$ $k_B T$ and we set $\alpha = 0.05$ meaning that the self-diffusion time of the proteins is 20 times larger than their conformational relaxation time. In both figures the solid red line indicates the concentration-dependent equilibrium fraction of proteins in the non-native state. In the coloured regions the dispersion is thermodynamically unstable, in the region shaded in purple the $\lambda_+ (0)$ mode is the dominant mode, while in the region shaded in orange the $\lambda_+ (\xi_{\text{max}})$ spinodal mode is dominant. a) Results for attractive interactions between proteins in the non-native state of strength $\chi = 10$ $k_B T$, and b) for attractive interactions between proteins in the non-native state of strength $\chi = 25$ $k_B T$. In this figure the coexisting phases are indicated by blue dots while the green points indicate the "equilibrium" spinodal dots.

in fig. 5.5b the coexisting phases are indicated by blue dots while the "equilibrium" spinodal points are indicated by green dots. The binodal points indicate that a phase with slightly more than half of the proteins in the native state coexists with a denser phase with almost all proteins in the non-native state. It turns out that for the model local free energy as given by eq. (5.4) coexistence is always between a relatively dilute phase of proteins mostly in the native state and a denser phase of proteins mostly in their non-native state. The definition of the "equilibrium" spinodal points is clarified by the same figure: the "equilibrium" spinodal points bound the concentration regime where the dispersion is thermodynamically unstable if $\eta \equiv \eta_{eq}$, where η_{eq} is the equilibrium fraction of proteins in the non-native state at the given concentration, which is indicated by the red line in the graphs in fig. 5.5.

The regions where the eigenmodes are active are shaded. In the region shaded in purple the $\lambda_+ (0)$ mode is dominant and in the region shaded in orange the $\lambda_+ (\xi_{\text{max}})$ spinodal mode is dominant. With increasing value of α the size of the region where the $\lambda_+ (0)$ mode is dominant decreases. This follows from eq. (5.14) ($f_{\eta\eta} < 0$) and can be understood because for small α the rate of a process that involves both protein diffusion and conformational changes, i.e., the $\lambda_+ (\xi_{\text{max}})$ mode, is limited by protein self-diffusion and hence slower than a process that only involves changes in protein conformation, i.e., the $\lambda_+ (0)$ mode.

Indicated in fig. 5.5 are three non-equilibrium states for which relaxation to equilibrium occurs by different kinetic mechanisms. For the weak-coupling regime we restrict our kinetic analysis to this and we shall address the kinetics by which phase separation occurs in the next section. There we address the strong-coupling regime, for which we expect the kinetics of phase separation to be more interesting due to the underlying first-order conformational phase transition. Let us now briefly discuss the expected non-equilibrium behaviour that should be observed during relaxation from the three different non-equilibrium states shown in fig 5.5.

For non-equilibrium state I, $\phi_0 = 0.15$, $\eta_0 = 0.75$, we find from the linear stability analysis that none of the modes discussed in the previous section are active and that the protein conformation should relax across the system toward equilibrium according to eq. (5.11). For this non-equilibrium state we find $f_\eta = 0.146$ and $f_{\eta\eta} = 0.575$, and eq. (5.11) indicates that while fluctuations in η do not grow over time. However, the initial value $\eta_0 = 0.75$ is not stable because for $\tau \to \infty$ we find $\delta\eta\,(\tau) = -f_\eta / f_{\eta\eta} \neq 0$. While this limiting solution does not result in relaxation to the equilibrium value of η, we do expect that η, should spontaneously relax towards a value corresponding to a (local) minimum in the free energy. The reason is that it is a non-conserved quantity and nothing prevents this from happening. In this case, non-linear effects that are not included in eq. (5.11) must clearly be included to determine the kinetics by which full relaxation to equilibrium occurs.

The expected behaviour for state II, $\phi_0 = 0.6$, $\eta_0 = 0.45$, is different. Here the spinodal mode is the dominant relaxation mode, eq. (5.14), and $\lambda_+ (\xi_{\text{max}} = 0.18) = 1.178$ while $\vec{m}_+ = (0.003, 0.999)$, see fig. 5.3 for an example of the corresponding dependence of λ_+ on ξ for the spinodal mode. This suggests that initially the dispersion phase separates into domains of a typical size $2\pi/\xi_{\text{max}}^{-1}$ in which small differences in protein concentration and conformation are established. The results of the stability analysis suggest that this process should continue until the fraction of proteins in the non-native state, η, in both phases is such that these dispersion state are no longer located in the region that is shaded orange in fig. 5.5. From this point onward, the fraction of proteins in the non-native state should increase according to the full non-linear kinetic equation. Interestingly, the stability analysis suggests that at this point there is no driving force that leads to the spontaneous disappearance of the phase separated domains formed in the previous stage of the relaxation process because fluctuations are suppressed ($\lambda_\pm < 0$). This suggests that the homogeneous equilibrium phase is either reached by a process described by effects captured only in the full non-linear kinetic equations, possibly related to the presence of an interface between the two phases, or by the gradual brake down of these domains by fluctuations near the interface.

The mechanism by which relaxation from state III, $\phi_0 = 0.9$, $\eta_0 = 0.05$ occurs, should be a combination of the behaviour observed for state I and II. Initially relaxation of the average protein conformation, η, towards equilibrium must occur according to eq. (5.11) because $\lambda_{\pm} < 0$ and subsequently by effects only included in the full non-linear kinetic equations. This continues until η has a value where the region shaded in orange in fig. 5.5a is briefly entered. Here $\lambda_{+}(\xi)$ has a positive value for non-zero values of ξ, suggesting that the dispersion should phase separate in a manner similar to the one as discussed for the expected non-equilibrium behaviour from state II in the above. It should be noted that the actual difference between the regions shaded in orange and purple is in this case small. The difference is the position of the maximum in $\lambda_{+}(\xi)$ which is at $\xi = 0$ for the region shaded in purple while it is at a non-zero value of ξ for the region shaded in orange. For example, for non-equilibrium state II, $\lambda_{+}(\xi_{\text{max}} = 0.18) = 1.178$ and $\vec{m}_{+}(\xi_{\text{max}} = 0.18) = (0.003, 0.999)$ while $\lambda_{+}(\xi = 0) = 1.176$ and $\vec{m}_{+}(\xi = 0) = (0, 1)$ implying that both eigenmodes are almost identical and equally fast.

Non-equilibrium states that should display qualitatively identical relaxation mechanisms as the three mechanisms discussed in the above can also be found in the phase and stability diagram in fig. 5.5b. In addition to these modes, there are non-equilibrium states that relax towards a heterogeneous, phase-separated equilibrium state. We postpone a discussion of the kinetics by which phase separation occurs to the next section, where phase separation is coupled to an underlying first-order conformational phase transition.

5.6 Phase and stability behaviour in the strong-coupling regime

Having considered a number of different aspects of the non-equilibrium behaviour in the weak-coupling regime, we now turn to the strong-coupling regime. In fig. 5.6 the phase diagram for $\epsilon = 3$, which is representative of the strong-coupling regime, is shown. As before, the solid line indicates the binodal and the dashed line indicates the “equilibrium” spinodal. Further details can be found in chapter 3 where this phase diagram is discussed in detail.

Here, we specifically focus on the results of the linear stability analysis for $\epsilon = 3$ and $\chi = 6$, see fig. 5.7a, and $\epsilon = 3$ and $\chi = 10$, see fig. 5.7b. This allows us to investigate two important features of the phase diagram in fig. 5.6. Firstly, it allows us to investigate the nature of the “critical point” at $\chi = 6$ and $\phi = 1$ where the two binodals appear to meet. Secondly, it allows us to clarify the non-standard definition of the “equilibrium” spinodal lines. From fig. 5.7a, it is clear that the binodals do in fact not meet in a single point at $\phi = 1$ for $\chi = 6$ because the two coexisting phases, indicated by blue dots, differ in the fraction of proteins that are in the non-native state. As discussed in chapter 3 this corresponds to an Ising-like demixing of the conformations at fixed concentration $\phi = 1$. From figs. 5.7a and 5.7b, the nature of the spinodals also becomes clear, for they relate to the stability of the dispersion states on either the lower or upper part of the η_{eq} curve where the free energy is at a (local) minimum with respect to η, these are the curves indicated by the solid red line, which

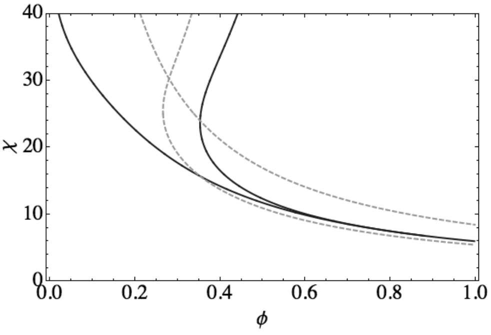

Figure 5.6: The phase and stability diagram for a free energy difference between the native and non-native state of the protein of $\epsilon = 3\ k_B T$. See fig. 5.4 for further details. For $\phi = 1$ an Ising-like conformational demixing is predicted, see chapter 3, fig. 3.8b.

are separated by the dashed red line that demarcates a local maximum in the free energy. Both of these features are a consequence of the first-order conformational phase transition that underlies the phase separation of the dispersion. Just as in the previous section, we have indicated a number of non-equilibrium dispersion states for which we expect interesting kinetic processes during the relaxation towards equilibrium in fig. 5.7. In the following we discuss the expected behaviour for each of these states.

Non-equilibrium state IV, with $\phi_0 = 0.04$ and $\eta_0 = 0.50$, is located in the region shaded in light blue. Here the $\lambda_+(\infty) = 0.08$ mode is dominant and $\vec{m}_+(\infty) = (-0.08, 0.99)$, see eq. (5.13) and fig. 5.2, suggesting that initially the local protein conformation changes the most while smaller differences in protein concentration are also established. While $\lambda_+(0) = 0$, the eigenvalue quickly increases up to $\lambda_+ = 0.079$ at $\xi = 10$, indicating that the initial stage of phase separation is approximately equally fast at all length scales larger than $\xi^{-1} = 1/10$. The corresponding pattern of phase separating domains should be fractal in nature, where the scale invariance breaks down at length scales above $2\pi\xi^{-1} = 1/10$ and below the size of a single protein. Note that the final equilibrium state is a homogeneous phase with $\eta_{\text{eq}} = 0.045$. After the initial stages of phase separation as described in the above, relaxation should continue towards the equilibrium state in the same manner as described for non-equilibrium state II in the previous section, see also fig. 5.5a.

Non-equilibrium states V, with $\phi_0 = 0.96$ and $\eta_0 = 0.82$, and VI, with $\phi_0 = 0.96$ and $\eta_0 = 0.74$, are of interest because these dispersion states should initially relax towards the homogeneous meta-stable dispersion state at $\eta = 0.90$, away from the local maximum, because this is the direction in which the free energy of the dispersion decreases, see fig. 5.7a. For state V the kinetics by which this occurs should be similar to the kinetics by which relaxation occurs from state I as discussed in the previous section, see fig. 5.5a, while for state VI the kinetics should be similar to the

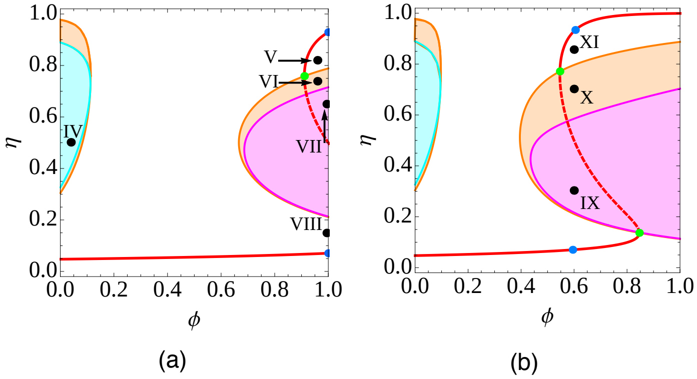

Figure 5.7: Summary of the equilibrium and stability behaviour of the model protein dispersion as a function of protein volume fraction, ϕ, and average protein conformation, η, for a free energy difference between the native and non-native state of $\epsilon = 3\ k_B T$. We set $\alpha = 0.05$ meaning that the self-diffusion time of the proteins is 20 times larger than their conformational relaxation time. In both figures the solid red line indicates a (local) minimum in the free energy at fixed concentration while the dashed red line indicates a maximum. Coexisting phases are indicated by blue dots while the green dots indicate the "equilibrium" spinodal points. In the coloured regions the dispersion is thermodynamically unstable, in the region shaded in purple the $\lambda_+ (0)$ mode is the dominant mode, in the region shaded in light blue the $\lambda_+ (\infty)$ mode is dominant, while in the region shaded in orange the $\lambda_+ (\xi_{\text{max}})$ spinodal mode is dominant. a) Results for attractive interactions between proteins in the non-native state of strength $\chi = 6\ k_B T$ and b) for attractive interactions of strength $\chi = 10\ k_B T$.

relaxation kinetics as described for state II, see fig. 5.5a. After having reached the meta-stable dispersion state at $\eta = 0.90$, of which the free energy is $0.96\ k_B T$ larger than the actual equilibrium state at $\eta = 0.07$, the final relaxation to the homogeneous equilibrium state should occur by an activated process because the free energy barrier of $0.47\ k_B T$ at $\eta = 0.57$ must be crossed to reach this phase.

Non-equilbrium states VII, with $\phi_0 = 1$ and $\eta_0 = 0.65$, and VIII, with $\phi_0 = 1$ and $\eta_0 = 0.15$ are of interest because for $\phi = 1$, $\chi = 6$ and $\epsilon = 3$ there is an Ising-like coexistence between a phase of proteins mostly in their native state, $\eta = 0.07$, and a phase with most proteins in their non-native state, $\eta = 0.93$, as indicated by the blue binodal points in fig. 5.7a. The coexisting phases have equal free energy and are separated by a free energy barrier of $0.12\ k_B T$ at $\eta = 0.5$ relative to the two coexisting phases. Hence, thermal fluctuations are sufficient to allow access to both coexisting phases. However, while both coexisting phases are easily reached by thermal fluctuations, it is questionable whether this small free energy barrier is sufficient to allow for the observation of conformational phase separation at fixed concentration $\phi = 1$ because neither of these phases are very stable with respect to thermal fluctuations. Finally, we note that state VII and VIII differ in stability and in the direction of the initial relaxation process, which for state VII is towards the coexisting phase with $\eta = 0.93$ and for state VIII towards $\eta = 0.07$. Hence, the maximum in the free energy, as indicated by the dashed red line in fig. 5.7a separates regions where the number of proteins in the non-native state initially increase and decrease.

The final three non-equilibrium states, IX, with $\phi_0 = 0.6$ and $\eta_0 = 0.3$, X, with $\phi_0 = 0.6$ and $\eta_0 = 0.70$, and XI, with $\phi_0 = 0.6$ and $\eta_0 = 0.85$, are all at a concentration intermediate to the two coexisting phases with $(\phi = 595, \eta = 0.070)$ and $(\phi = 0.605, \eta = 0.934)$, which are indicated by blue points in fig. 5.7b. Hence, the equilibrium phase of all three phases is an identically phase separated state because the protein concentration in states IX-XI is equal. However, the kinetics by which phase separation occurs should be different for the three states. Non-equilibrium states IX and X are both thermodynamically unstable and phase separation should initially proceed by spinodal decomposition, for state IX the $\lambda_+(0)$ is the dominant mode while for state X the $\lambda_+(\xi_{max})$ mode is dominant. In sections 5.4 and 5.5 we discussed these modes in some detail.

For state IX relaxation is initially towards the local minimum in the free energy at $\eta = 0.07$ while for X it is towards the local minimum at $\eta = 0.91$, which is in both cases “away” from the second coexisting phase. The question is now by which kinetic mechanism the fully phase separated state is reached. Without numerical evaluation of the full non-linear kinetic equations, this is not easy to answer. However, we can consider three different plausible mechanisms:

1) It is possible that states IX and X initially relax towards a homogeneous metastable state with an average protein conformation, $\eta = \eta_{eq}$, much like the relaxation of state II as discussed in the previous section. If this indeed happens the final phase separation must be a nucleated processes just like phase separation from state XI must be a nucleated process, where the nucleation step involves both changes in the local protein concentration and conformation.

2) If during the initial stages of spinodal composition one of the phases gets sufficiently close to the local maximum, which separates the final two coexisting phases (indicated by the dashed red line), it is possible that thermal fluctuations “push” some of the phase separating domains of over this barrier. This would allow this domain to relax towards the second coexisting phase, which could subsequently grow until the system is fully phase separated. This last step is essentially a nucleation step that must occur during the spontaneous spinodal decomposition of the dispersion.

3) If one of the phases that is formed during the initial spinodal decomposition reaches either of the points where the dashed and solid red line meet (the green spinodal points are on top of these points in fig. 5.7b), then at this point there is no longer a free energy barrier preventing this phase from relaxing to the second coexisting phase and the system should spontaneously fully phase separate.

Presumably, which and if phase separation occurs by any of these 3 mechanisms depends strongly on the parameter α, which sets the difference in the time scale at which differences in protein concentration and conformation are established. However, numerical evaluation of the full kinetic equations are clearly needed to understand in which manner phase separation occurs when the coexisting phases are separated by a first-order conformational phase transition.

5.7 Discussion

We have studied the kinetics by which relaxation to equilibrium occurs in a model two-state protein dispersion. In our model dispersion, proteins can switch between a native and a high-energy non-native state, which can be stabilised by attractive interactions with other proteins that are also in the non-native state. Because a kinetic process typically involve both changes in protein concentration and conformation, both the time scale at which changes in protein concenctration, i.e., the protein self-diffusion time and the time scale at which the conformation of a protein changes are important in determining the actual kinetics by which these processes occur.

Our analysis is based on linear stability analysis of a set of model-C kinetic equations[92] that we applied to a free energy functional that includes a non-local square gradient term[115] that penalises gradients in the concentration of proteins in the non-native state. Furthermore, the free energy functional includes a local free energy based on a model two-state protein and the Carnahan-Starling equation of state for a hard-sphere fluid.[91] The phase behaviour of this free energy is discussed in detail in chapter 3.

The analysis shows that the kinetics by which non-equilibrium states relax towards a thermodynamic equilibrium phase is highly non-universal and strongly dependent on the protein concentration, the protein conformation, as well as the other three model parameters. Moreover, the kinetics by which equilibrium states are reached can differ significantly and widely between different non-equilibrium states. Nonetheless, there are a number of common factors underlying the different kinetic processes that can occur in the model dispersion.

Firstly, in any state that is thermodynamically unstable, the instability grows initially by any of three different relaxation modes, which we obtained from a linear stability analysis. These three modes are, 1) the global relaxation of protein conformation, 2) a spinodal mode where phase separation involving changes in both concentration and conformation occurs at a well defined length scale and 3) a scale-free relaxation of both protein concentration and conformation in a manner in which the local concentration of proteins in the non-native state is conserved.

Presumably this last mode is an artifact of our model because the free energy functional, eq. (5.3), only incorporates a square-gradient term penalising the formation of gradients in the concentration of proteins in the non-native state. The spinodal mode where phase separation initially occurs at a distinct length scale is by and large conventional. In an experiment this mode would be indistinguishable from a standard spinodal decomposition process that does not involve changes in protein conformation, unless one actually “measures” the conformation of the proteins in the dispersion. Finally the mode, which involves the global relaxation of proteins is experimentally observed when proteins reversible denature and renature.[117]

There are a number of other common features between the different kinetic processes. Because the average conformation of the proteins, η, is a non-conserved quantity, it at all times spontaneously relaxes towards a value $\eta \equiv \eta_{eq}$ such that the free energy is at a (local) minimum. As we have seen, this can involve temporary phase separation in the system. Furthermore, in the strong-coupling regime the presence of two minima in the free energy separated by a maximum at fixed concentration causes non-equilibrium states with values of η above and below this maximum to initially relax towards different dispersion states. Finally, all of the kinetic processes (or parts of it) typically still resemble either spinodal decomposition or nucleation and growth, even if these processes also involve changes in the conformation of the proteins.

Perhaps most interesting is the kinetics by which phase separation occurs in our model dispersion in the strong-coupling regime. Here, the underlying first-order conformational phase transition greatly complicates the kinetic process by which phase separation occurs. While we speculate on a number of kinetic processes by which the system fully phase separates, a real understanding of these processes must involve numerical evaluation of the full non-linear kinetic equations in which thermal fluctuations are taken into account because the underlying first-order conformational phase transition can impose a nucleation step even if phase separation initially proceeds by spinodal decomposition.

In summary, phase separation and relaxation processes in our model two-state protein dispersion, in which the proteins can reversibly switch between different conformations, are highly non-universal even if these processes strongly resemble classical spinodal decomposition or nucleation and growth.

Part II

Ultrasonication of carbon nanotubes

Chapter 6

Scission mechanics of carbon nanotubes by analytic theory

Summary

In this chapter we present a theoretical study of the mechanics of carbon nanotube scission under sonicaton, based on the accepted view that it is caused by strong gradients in the fluid velocity near a transiently collapsing bubble. We calculate the length-dependent scission rate by taking the actual movement of the nanotube during the collapse of a bubble into account, allowing for the prediction of the temporal evolution of the length distribution of the nanotubes. We show that the dependence of the scission rate on the sonication settings and the nanotube properties results in non-universal, experiment-dependent scission kinetics potentially explaining the variety in experimentally observed scission kinetics.

The contents of this chapter has been published as:
J. Stegen, J. Chem. Phys. **140**, 244908 (2014).

6.1 Introduction

Carbon nanotube-based polymer composites[8,27,28] are promising new materials in which carbon nanotubes are, for example, used to create transparent conductive layers.[9,10] Dispersions of exfoliated nanotubes are required for the production of these so-called latex based nanotube composites.[8] Such dispersions can be obtained by means of sonication,[39,118–123] however, sonication also induces scission of nanotubes. Scission is unwanted because the quality of nanotube composites strongly depends on nanotube length.[124] Hence, the subject of nanotube scission under sonication has received some attention in literature.[38,125–134] There has however been little theoretical work on the scission mechanics of carbon nanotubes under sonication.[126,127,130,133,134] In fact, no attempt to describe exfoliation and scission simultaneously has been made. Such a description is highly relevant for it would, in principle, allow for the determination of optimal sonication settings. Pertinent questions that arise in this context include: How can a maximum degree of exfoliation and a minimum of nanotube scission under sonication be achieved? How can sonication be used to control the length distribution of a nanotube dispersion? This chapter provides a first step towards answering these questions.

During sonication an acoustic field is applied to a liquid and the resulting interaction between small bubbles in it and the acoustic field is known as acoustic cavitation.[40–42,135–138] In the process of acoustic cavitation, oscillations of the acoustic pressure cause the growth of microbubbles due to rectified diffusion.[42] These become unstable above a critical bubble radius.[136,138,139] The instability leads to the explosive growth of the bubble up to some maximum radius[139] and ends in the violent transient collapse of the bubble.[40] The violent nature of transient cavitation has been used to cut a wide variety of macromolecules, including carbon nanotubes. Much attention has been devoted to the disentanglement and scission of polymers.[140,141] The degradation of DNA[142] and the fragmentation of other fiber-like structures such as protein fibrils[143] has been studied. All of these macromolecules have a high aspect-ratio, which makes them sensitive to the strong gradients in fluid velocity that accompany the transient collapse of a bubble. The exact scission mechanism will however depend on the atomic structure of the macromolecule. Relevant in this regard is the work by Yu et al. who have studied the mechanics of scission under tension for single and multi-wall carbon nanotubes as well as that of single-wall nanotube ropes.[34,144] They observed that scission occurs in the outer tubes as, in their experiments, forces are primarily exerted on these tubes. We expect that similar scission mechanisms are at play during sonication. Here too, forces are primarily exerted on the outer tubes by the fluid flow, potentially leading to layer-by-layer scission of multi-wall nanotubes and to exfoliation of nanotube bundles.

The mechanics of nanotube scission under sonication is determined by the interaction between the flow set up in the fluid following the transient collapse of a bubble and a nanotube. Following the model for polymer scission under sonication, as proposed by Kuijpers et al.,[140] Hennrich et al. attributed the scission of carbon nanotubes to the high strain rate of the fluid flow resulting from the transient collapse of the bubble. Strong viscous drag forces exerted by the fluid on the nanotube, which they presume to be radially aligned in the flow field, are responsible for scission of the nanotube in their model. In particular, they demonstrated that the total drag force exerted by the fluid on the nanotube is proportional to the square of the nanotube length, and realised that this implies a terminal nanotube length below which scission can no longer occur.[126] This idea was reformulated by Ahir et al. in a simple model that gives a mathematical expression for the minimum nanotube length that can be reached by sonication for a given maximum strain rate experienced by the nanotube.[127] Lucas et al. realised that the scission rate of nanotubes should be length-dependent and is related to the probability that a nanotube is close to a cavitating bubble. Because a longer nanotube sweeps out a larger volume it is more likely to be close to a cavitating bubble and should thus break more easily. Their experimental results show a power law dependence of the average nanotube length on the amount of supplied acoustic energy.[130] A power law decay of the average length has been reported by other groups as well, albeit that the reported value of the exponent seems to be non-universal.[122, 126, 130, 132] A very similar result was obtained for the *exfoliation* of nanotube bundles under sonication,[122, 123] indeed suggesting that perhaps the same mechanism is responsible for scission and exfoliation.

Although the mechanism by which scission is thought to occur, that is, under tension, is well established, there has been some discussion on the role of buckling-mediated scission of nanotubes. Simulations by Chew et al. suggest that nanotubes enter the bubble during explosive growth and are expelled from the bubble due to their inertia in the final stages of collapse. After expulsion from the bubble into the liquid, the tangentially oriented nanotubes buckle and break due to overbending.[133] Pagani et al. argue that the mechanism proposed by Chew et al. is relevant only to a tiny fraction of carbon nanotubes for most nanotubes never get sufficiently close to the bubble to be absorbed into it.[134] Their simulations show that the scission mechanism is length-dependent, long nanotubes are expected to buckle and break while short nanotubes orient radially and break under tension, where the crossover-length between the two mechanisms is determined by the bending stiffness of the nanotube. Furthermore, they realised that there is a critical distance between bubble and nanotube at the start of bubble collapse beyond which no scission occurs: beyond this critical distance the fluid strain rate around the nanotube does not become sufficiently high. Finally, and importantly, Pagani et al. show that the two proposed mechanisms lead to different exponents for the power law describing the average nanotube length as a function of time, thus potentially explaining the non-uniformity of experimental results.[134]

Here we expand on earlier work[126, 127, 130, 133, 134] and primarily investigate the mechanics of nanotube scission under tension in detail, by taking nanotube motion during bubble collapse explicitly into account. In doing so, we find that the kinetics of scission under tension are non-universal, potentially providing an alternative to the mechanism proposed by Pagani et al.[134] as responsible for the variety in experimentally determined scission kinetics that are reported in literature. In our model, we approximate a carbon nanotube as a rigid, inexstensible rod. We characterise the process of transient cavitation by two length scales, being the typical bubble radius before and after explosive growth. We model the collapse of a bubble using the empty cavity approximation,[145] because, unlike the Rayleigh-Plesset equation[40] it gives a universal analytical relation between the bubble radius and the velocity of the bubble wall, which allows for the derivation of a universal equation giving the stress exerted on a nanotube by the fluid as a function of bubble radius. Furthermore, we make plausible that it is a reasonable approximation for the mathematically more complicated but more realistic Rayleigh-Plesset equation.[40] To describe the interaction between the fluid and the nanotube we invoke first-order slender-body theory,[146, 147] and by assuming Stokesian dynamics, we derive the equations of motion for the temporal evolution of the translation and rotation of the nanotube. Using these equations of motion we investigate the scission mechanics for radially aligned nanotubes by taking the actual motion of nanotubes during bubble collapse explicitly into account.

By taking nanotube motion into account, we derive a length-dependent scission rate that is determined by the critical initial distance between nanotube and bubble below which scission occurs. We find that the scission rate depends on nanotube properties, such as their length and tensile strength, as well as on the sonication conditions. For nanotubes significantly longer than the terminal length, the scission rate scales with L^2, in agreement with earlier work.[126, 134] However, when approaching the terminal nanotube length, deviations from this scaling law arise. This gives rise to non-universal scission kinetics, where the mean nanotube length scales as $t^{-\alpha}$ with $\alpha \leq 0.5$ a non-universal exponent. This is in agreement with experimental results where exponents varying between 0.22 and 0.5 have been reported,[126, 130] but contrasts with earlier work where scission of radially aligned nanotubes under tension was thought to result in universal scission kinetics.[126, 127, 129, 130] We furthermore find that the minimum scission length, the nanotube length below which no scission can occur, scales as $\sigma_T^{1/1.16}$ when nanotube motion is taken into account instead of the previously predicted $\sigma_T^{1/2}$,[126, 127, 129, 130] where σ_T is the tensile strength of the nanotube. The terminal length, the shortest nanotube segments that can be produced by sonication, follows an identical scaling relation with tensile strength for it is equal to approximately half the minimum scission length. Finally, we briefly discuss the implications of our model for the competition between scission under tension and buckling mediated scission as proposed by Pagani et al.[134] and we make plausible that the mechanism responsible for scission can provide an explanation for the exfoliation of carbon nanotube bundles.

The remainder of this chapter is organised as follows, in section 6.2 we discuss the model that we invoke to describe a bubble undergoing transient cavitation. In section 6.3 we present our description of a nanotube and the interaction it has with a cavitating bubble. In section 6.4 we combine the models of section 6.2 and 6.3 to determine the motion of and the forces exerted on a radially oriented nanotube during bubble collapse. Subsequently, in section 6.5 we investigate the implications of the results from section 6.4 for scission kinetics. The chapter concludes with a discussion in section 6.6, where we propose a scission-mediated exfoliation mechanism.

6.2 Bubble dynamics

Any attempt to describe the mechanics of carbon nanotube scission under sonication requires three key ingredients: 1) a model describing fluid motion during transient cavitation, 2) a model for a carbon nanotube and 3) a model for the interaction between the nanotube and the fluid. In this section we discuss the first ingredient and give a brief and simple overview of the process of transient cavitation. We discuss relevant length scales and show how the assumption of incompressibility in combination with Rayleigh's model for the collapse of an empty cavity[145] provides a full description of the fluid flow following the transient collapse of a bubble. It is explained why we use the empty cavity approximation rather than the more accurate and more frequently used Rayleigh-Plesset equation.[40] We shall be using the results of this section in section 6.4, where we study the mechanics of scission under tension for radially aligned nanotubes. Before that, in section 6.3, we discuss our model of a nanotube and the interaction between a nanotube and a fluid flow.

During sonication an acoustic field is applied to a liquid, causing oscillations in the size of small bubbles present within the liquid. This is known as stable cavitation.[40, 135] Due to rectified diffusion,[42] i.e., the net diffusion of dissolved gas into an oscillating bubble, these small bubbles slowly grow over many pressure cycles up to a critical radius, the so-called Blake threshold, for a discussion of which we refer to the literature.[136, 138, 139] This threshold is determined by the amplitude of the applied acoustic field and the surface tension of the bubble surface. It separates stable and transient cavitation, the latter being initiated when the surface tension can no longer contain the growth of the bubble during the negative pressure peak or the rarefaction phase of the applied acoustic field. The bubble then undergoes explosive growth and, assuming it grows sufficiently much, it undergoes transient collapse during the next positive pressure peak of the acoustic field.[139] The maximum bubble radius is reached when growth eventually slows down as the rarefaction phase ends and the acoustic pressure becomes positive.[139] Collapse of the bubble is now initiated by the still increasing acoustic pressure.[40] A schematic overview of the various stages of a bubble in an acoustic field is shown in fig. 6.1. The bubble sizes as shown for the various stages are not drawn to scale.

To model transient cavitation, we consider a single spherical bubble within an incompressible liquid medium. To the liquid, a harmonic acoustic field, $p(t)$, with frequency ω and amplitude p_a is applied,

$$p(t) = -p_a \sin \omega t, \tag{6.1}$$

where $p_a = \sqrt{2P_{ac}\rho c/A_{son}}$ is the acoustic pressure amplitude with ρ the mass density and c the speed of sound in the liquid, while P_{ac} is the power of the applied acoustic field and A_{son} is a typical surface area through which the acoustic field passes. We approximate A_{son} by the surface area of the sonicator horn, which should be seen as a lower estimate for A_{son}. Using typical sonication conditions,[1] that is, a power of 40

---

[1] We define a typical sonication experiment as sonication at 40 W and a frequency of 20 kHz where the

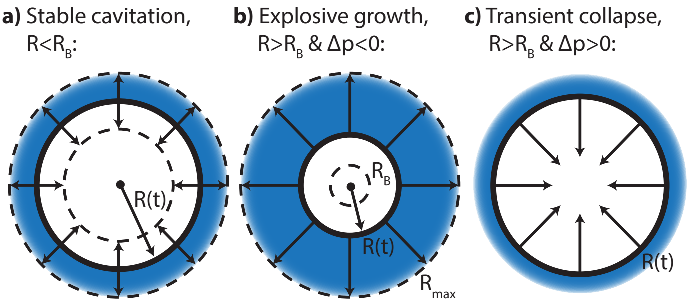

Figure 6.1: Overview of bubble dynamics, a) For bubbles with a radius $R(t)$ smaller than the Blake threshold, R_B, small amplitude oscillations in bubble radius, indicated schematically by double-pointed arrows, are induced by the acoustic field. The bubble slowly grows over many pressure cycles through rectified diffusion.[42] b) The bubble radius exceeds the Blake threshold and grows explosively so long as the pressure within the fluid is smaller than that in the bubble, $\Delta p < 0$. At the end of explosive growth the bubble has a maximum radius, R_{max}, given by eq. (6.3). c) The pressure difference between fluid and bubble becomes positive, $\Delta p > 0$, and the bubble collapses violently as described by eqs. (6.4) and (6.5). Note that the bubble sizes shown for the various stages are not to scale.

W, a frequency of 20 kHz and a sonicator horn of 15 mm diameter, we find a typical acoustic pressure amplitude of $p_a = 8.2 \cdot 10^5$ Pa for sonication in water under ambient conditions.

We can now turn to the following question: How does the size of a bubble prior to undergoing explosive growth compare to the mean size of a nanotube for a typical sonication experiment? We find by calculation of the Blake threshold,[136,138,139] that bubbles with a radius larger than 0.1 µm grow explosively while at higher sonication power this radius is even smaller. Hence, in most practical situations the length of a nanotube, which we assume to be of the order of a micron, exceeds the radius of a bubble undergoing stable cavitation by at least a factor 5.

This leads us to the following question: how large is a bubble after it has reached the Blake threshold and undergone explosive growth? To answer this question, it seems reasonable to presume that growth of the bubble occurs when the pressure in the surrounding liquid is lowered by the applied acoustic field to a value below the pressure within the bubble. If we follow Apfel,[139] then the average bubble-wall velocity during this period must be $v_g = \sqrt{4\left(p_a - p_0\right)/9\rho}$, where $2\left(p_a - p_0\right)/3$ is the average pressure difference between the interior of the bubble and the surrounding liquid during this period and p_0 is the ambient pressure in the liquid in the absence

---

sonicator horn has a diameter of 15 mm. Sonication takes place in water under ambient conditions. In the typical sonication experiment single wall nanotubes with a tensile strength of 30 GPa, a diameter of 1.3 nm and a wall thickness of 0.3 nm are sonicated.

of an applied acoustic field. This average velocity follows from Rayleigh's model for the collapse of an empty cavity which we will discuss shortly.[145] If we multiply this average velocity with the time that the interior bubble pressure, which we assume to be zero, exceeds the pressure in the surrounding liquid, that is, the time for which $p\left(t\right)+p_0<0$ where $p\left(t\right)$ is given by eq. (6.1), we obtain a first approximation for the maximum bubble radius. The time for which $p\left(t\right)+p_0<0$ holds is approximately equal to $t_g=2\sqrt{2\left(1-p_0/p_a\right)}/\omega$.[139] If we multiply this period of time with the average velocity of the bubble wall during this period, we obtain a first approximation for the maximum bubble radius,

$$R_1=\frac{4}{3\omega}\left(p_a-p_0\right)\sqrt{\frac{2}{p_a\rho}}. \tag{6.2}$$

Note that we neglected the radius the bubble has prior to undergoing explosive growth and assume R_1 to be equal to the amount by which the bubble radius increases. This is reasonable because the bubble radius typically grows by several orders of magnitude during explosive growth.

This approximation may be improved upon by taking into account that the bubble remains to grow even after the pressure in the surrounding liquid exceeds the pressure in the bubble. In this period the accumulated kinetic energy of the fluid flow is dissipated as pressure-volume work. By accounting for this Apfel obtained the following equation for the maximum bubble radius after explosive growth,[139]

$$R_{max}=\frac{4}{3\omega}\left(p_a-p_0\right)\sqrt{\frac{2}{p_a\rho}}\left[1+\frac{2\left(p_a-p_0\right)}{3p_0}\right]^{1/3}, \tag{6.3}$$

where the last factor of the equation is the correction to our first approximation. Eq. (6.3) allows us to estimate the maximum bubble radius after explosive growth for a typical sonication experiment, which turns out to be of the order of 0.7 mm. The actual maximum bubble radius is somewhat smaller than this, because viscous effects were neglected in the derivation of eq. (6.3). Interestingly, this implies that the correction factor included in eq. (6.3), which is typically of the order of unity, is not necessarily an improvement on eq. (6.2). Nonetheless, bubbles are, at the end of explosive growth, typically at least a factor 100 or more larger than the typical length of a carbon nanotube, which we again assume to be of the order of a micron.

After the bubble has reached a maximum radius, the acoustic pressure is positive and the final stage of transient cavitation is initiated, being the violent collapse of the bubble. It is during this stage of transient cavitation that nanotube scission occurs as the fluid flow subjects the nanotube to a high stress. We are interested in obtaining an expression for the fluid velocity as a function of time and distance from the center of the collapsing bubble. The radial dependence of the fluid velocity is fully determined if the bubble is assumed to remain spherical at all times and if the fluid is assumed to be incompressible. We presume both these assumptions to hold. Let the bubble radius be denoted as $R=R(t)$, the velocity of the bubble wall as $\dot{R}=\dot{R}(t)$ and the fluid velocity at a distance r from the center of the bubble as $\vec{v}(r,t)$. The radial dependence of the fluid velocity as a function of the radius of the bubble and the velocity of the bubble wall is then,

$$\vec{v}\left(r,t\right)=\frac{R^{2}\left(t\right)\dot{R}\left(t\right)}{r^{2}}\hat{e}_{r}, \tag{6.4}$$

where $\hat{e}_r$ is the radial unit vector.

Eq. (6.4) requires as input a model for the bubble radius as function of time. Even though the Rayleigh-Plesset equation[40] is a better and more frequently used model, we use the empty cavity approximation as proposed by Rayleigh[145] to model this, for it leads to a universal and mathematically tractable description of transient cavitation, which is easily applied. As we will see in section 6.4 and 6.5, it allows us to quantify the interaction between a nanotube and a collapsing bubble in terms of a few dimensionless numbers. Rayleigh derived the empty cavity approximation by modeling the bubble as an empty cavity that is filled up by fluid during its collapse, and by assuming that the energy released by pressure-volume work during collapse is converted into the kinetic energy of the fluid moving in to fill the cavity. This allowed him to derive a simple equation describing the transient collapse of a bubble. It takes the following dimensionless form,

$$\frac{dx}{d\tau}=-\sqrt{\frac{1-x^{3}}{x^{3}}}, \tag{6.5}$$

where $x=R\left(t\right)/R_{max}$ is the dimensionless bubble radius and $\tau=t/t_c$ the dimensionless time with $t_c=\sqrt{3\rho {R_{max}}^2/2p}$ a measure for the lifetime of the collapsing bubble, p is the (static) pressure difference between the inside and outside of the bubble and ρ is, as before, the fluid mass density. In the derivation of eq. (6.5) a static pressure difference between the bubble and the surrounding liquid, p, is assumed, in reality it is not static and the value of p must be approximated. We approximate p by the sum of the ambient pressure and the root-mean-square acoustic pressure, $p=p_a/\sqrt{2}+p_0$. For given sonication conditions, eqs. (6.3), (6.4) and (6.5) fully describe the fluid flow during the collapse of a bubble.

The question arises whether the description of transient cavitation as given by these equations is a good description. How do the results from eqs. (6.3), (6.4) and (6.5) compare to results of the more advanced Rayleigh-Plesset equation?[40] This equation is not reproduced here, but unlike eq. (6.5) it does include inertial and viscous effects as well as a time-dependent acoustic pressure. This question is in part answered by fig. 6.2, which shows the bubble radius and fluid strain rate at the surface of the bubble as a function of time during bubble collapse for a typical sonication experiment as determined by the empty cavity approximation (dashed blue line), the Rayleigh-Plesset equation (solid red line) as well as for the empty cavity approximation with length and time scales matched to the solution of the Rayleigh-Plesset equation (dotted blue line). The solution of the empty cavity approximation was obtained by numerically solving eq. (6.5) where R_{max} is determined by eq. (6.3)

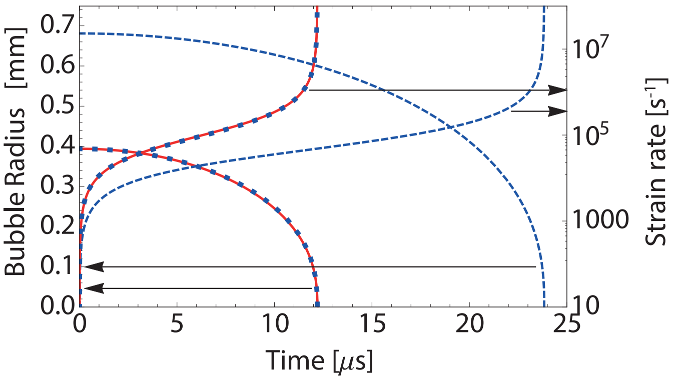

Figure 6.2: The bubble radius and strain rate at the bubble surface, $\dot{\epsilon} = \dot{R}(t)/R(t)$, as a function of time during the transient collapse of a bubble for a typical sonication experiment. Dashed blue lines represent the solution as obtained from the empty cavity approximation while the solid red line represents the solution obtained from the Rayleigh-Plesset equation. The solution of the empty cavity approximation, with length and time scales matched to the solution of the Rayleight-Plesset equation, is represented by the dotted blue line. Note that it is virtually identical to the solution of the Rayleigh-Plesset equation.

and the average pressure difference between bubble and the surrounding liquid, p, is approximated as $p_a/\sqrt{2}+p_0$. The Rayleigh-Plesset equation was solved for a full acoustic cycle, as given by eq. (6.1), using the methodology of Pagani et al.,[134] and by using an initial bubble radius of 0.1 μm, which equals the Blake radius for the given sonication conditions, only the collapse phase is shown here. From fig. 6.2 it is clear that solutions of the empty cavity approximation (dashed blue line) and the Rayleigh-Plesset equation (solid red line) do not match quantitatively even though the shapes of the curves are virtually identical. This is not so much the result of the poor quality of the empty cavity approximation but rather a result of a poor choice for the corresponding length and time scale, R_{max} and t_c.

How good is the empty cavity approximation if we rescale it to have it match time and length scales with the results from the Rayleigh-Plesset equation? In this case the agreement is excellent, the solution of the rescaled empty cavity approximation (dotted blue line) and the Rayleigh-Plesset equation (solid red line) are virtually identical. For typical sonication settings, the relative error in bubble radius and strain rate as given by the rescaled empty cavity approximation and as compared to the solution obtained from the Rayleigh-Plesset equation is less than 4 percent at all times. In an identical manner we compared the solution of the Rayleigh-Plesset equation and the rescaled empty cavity approximation for all combinations of acoustic powers of $P_{ac} = 10$ W, 40 W and 160 W, acoustic frequencies of 10, 20 and 40 kHz and initial bubble radii of 0.1 R_B, 1 R_B and 10 R_B. In doing so, we find the following, when a bubble has an initial radius of 0.1 R_B it undergoes stable cavitation as surface tension prevents the explosive growth of the bubble. For bubbles with an initial size of 1 R_B and 10 R_B we observe transient cavitation, in agreement with the definition of the Blake threshold. Here, we observe that the quality of the rescaled empty cavity approximation decreases with increasing acoustic power and increasing initial bubble radius, the relative error in bubble radius and strain rate reaches a maximum of approximately 35 and 45 percent respectively for an acoustic power of 160 W and an initial bubble radius of 10 R_B, while its quality appears to be independent of the acoustic frequency.

Note that even for a maximum relative error of 35 percent in the bubble radius and 45 percent in the strain rate, the disagreement is only quantitative. By matching the length and time scales of the empty cavity approximation to the solution of the Rayleigh-Plesset equation we assure that begin and end points of both curves are identical. Furthermore, an expansion of both the Rayleigh-Plesset equation and the empty cavity approximation yield identical behaviour for the initial stages of bubble collapse. In conclusion, the empty cavity approximation is typically very good but our approximation of the associated typical length and time scale of the transient collapse is poor. Fortunately, we can improve upon this poor approximation by determining the correct length and time scales directly from the solution of the Rayleigh-Plesset equation and use these values as input for the rescaled empty cavity approximation. Note that in the derivation of both the Rayleigh-Plesset equation and Rayleigh's model for the collapse of an empty cavity the fluid is presumed to be incompressible. As it is the assumption of incompressibility that leads to the strong gradient in the fluid velocity, which is responsible for nanotube scission, we feel confident in using Rayleigh's model for the collapse of an empty cavity because it captures the essential physics of the process.

Having described the process of transient cavitation, we can now investigate the interaction between a nanotube and the fluid flow generated by a bubble undergoing transient cavitation.

6.3 Fluid-Nanotube interaction

The motion of, and the forces exerted on a carbon nanotube near a transiently cavitating bubble are determined by the interaction between that nanotube and the fluid flow following the transiently cavitating bubble. We focus attention on defect-free carbon nanotubes with lengths well below their persistence length, determined to be in excess of 26 μm,[148,149] and model them as rigid rod-like particles with diameter d, length L and uniform tensile strength σ_T. Hence, in treating the nanotubes as rigid rod-like particles, we neglect any elastic bending and stretching of the nanotubes due to thermal fluctuations or the fluid flow. This is a reasonable approximation when studying the scission of radially aligned nanotubes under tension, because any bending of the nanotube is suppressed by the fluid flow. However, it does fail in the initial stages of bubble collapse, when a nanotube relaxes from a tangential orientation into either a stretched radially aligned or a highly bent conformation that can potentially lead to subsequent scission under tension or buckling-mediated scission respectively.[134] We return to this issue in our discussion, section 6.6.

We model the carbon nanotube as a rigid rod-like particle and invoke first-order slender-body theory to model the viscous drag forces exerted on the nanotube by the fluid flow, just as in previous work on nanotube scission under sonication.[126, 129, 130, 134] Slender-body theory[146, 147] describes the viscous drag forces exerted on an elongated particle in a Stokes flow. Stokes flows are characterized by a small Reynolds number, Re $\ll 1$,[2] implying that viscous effects are dominant over inertial effects. In our case, the Reynolds number is for most of the time typically small if we assume the typical length scale of interaction between the fluid flow and a nanotube to be the nanotube diameter. Intuitively this choice of length scale makes sense, because the fluid flow is ‘perturbed’ by the radially aligned nanotube over a length equal to its diameter. However, in the final stages of collapse of the bubble the relative fluid velocity at the tips of the nanotube becomes very large. Indeed, a simple scaling analysis shows that the Reynolds number must reach a maximum of the order of unity near the nanotube tips at the moment of scission[3] but is smaller than that in the central part of the nanotube and prior to the moment of scission. Even though the assumption of small Reynolds numbers does not quite hold at all times, it does hold for the majority of time and justifies our use of slender-body theory to model the fluid-nanotube interaction.

Before applying slender-body theory, we need to consider the geometry of the interaction between the bubble and the nanotube. Due to the presumed radial symmetry of bubble collapse and because the nanotube and the center of the bubble are always in a single plane, the fluid-nanotube interaction is reduced to a two-dimensional problem. The corresponding geometry is shown in fig. 6.3, where $\hat{e}_x$ is the direction perpendicular to the bubble surface while $\hat{e}_y$ is a direction tangential to the bubble surface. Although rotational motion of the nanotube around $\hat{e}_x$ and out of the $x-y$ plane is possible, we need not explicitly consider it. The reason is that the radial distance between any segment of the nanotube and the center of the bubble is invariant under any such rotation, that is, the geometry of the problem does not change as a result of this rotational motion. Furthermore, rotation around $\hat{e}_x$ affects neither translational nor rotational motion in the $x-y$ plane, as we show below.

Within first-order slender-body theory,[146, 147] the viscous drag force per unit length exerted by the fluid flow on the nanotube, $\vec{f}$, can be decomposed into a component

---

[2] The Reynolds number is defined as $Re = \rho v L/\mu$, where ρ is the mass density of the liquid, v the mean relative velocity of the fluid relative to the object, L is the characteristic length of the object and μ is the dynamic viscosity of the fluid.

[3] If we assume a linear flow profile and equate the stress on the nanotube to the tensile strength, σ_T of the nanotube we find $\sigma_T = \pi\mu\dot{\epsilon}L^2/2A$. The maximum relative fluid velocity occurs at the nanotube tips and is given by $v_{max} = \dot{\epsilon}L/2 = \sigma_T A/\pi\mu L$. Using this as the characteristic velocity and the nanotube diameter as the characteristic length-scale we find a maximum Reynolds number of the order of 1 for the fluid flow around around the nanotube.

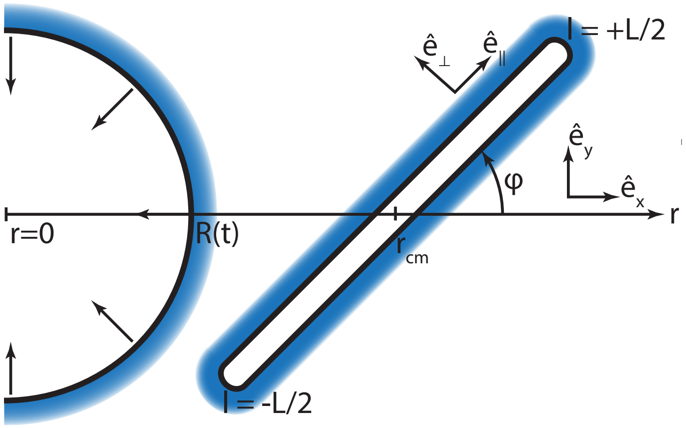

Figure 6.3: The spatial geometry of the nanotube bubble interaction. The bubble has radius $R(t)$, the center of the nanotube of length L is at a distance r_{cm} from the center of the bubble and at an angle φ from a radial orientation. The contour distance away from the center of mass of the nanotube is given by l. Two coordinate systems are shown: $\hat{e}_x$, $\hat{e}_y$ denote respectively the direction perpendicular and the direction tangential to the bubble surface. Coordinate system $\hat{e}_\perp$, $\hat{e}$ defines the directions parallel and perpendicular to the main axis of the nanotube.

parallel, f, and perpendicular, $f_\perp$, to the main axis of the nanotube,

$$f = 2\pi\mu v_{,rel}, \qquad f_\perp = 4\pi\mu \; v_{\perp,rel}, \tag{6.6}$$

where μ is the dynamic viscosity of the liquid, $v_{,rel}$ is the relative fluid velocity parallel to the axis of the nanotube, while $v_{\perp,rel}$ is the relative fluid velocity perpendicular to the axis of the nanotube. These velocities are relative ones, that is, relative to the translational and rotational motion of the nanotube. Here we neglect a logarithmic dependence of these forces on the aspect ratio of the nanotube, which is of the order of unity for experimentally relevant nanotube lengths.[126] The relative fluid velocity is given by,

$$\vec{v}_{rel} = \vec{v}\,(r) - \vec{v}_{cnt} - \dot{\varphi} l \hat{e}_\perp, \tag{6.7}$$

where $\vec{v}\,(r)$ is the local fluid velocity at a radial distance r from the center of the bubble as given by eqs. (6.4) and (6.5), $\vec{v}_{cnt}$ is the translational velocity of the nanotube, $\dot{\varphi}$ denotes the angular velocity of the nanotube around its center of mass, l is the contour distance away from the center of mass of the nanotube and $\hat{e}_\perp$ is a unit vector perpendicular to the main axis of the nanotube, all as shown in fig. 6.3.

As mentioned, the fluid flow along the nanotube is presumed to be characterised by a small Reynolds number. For small Reynolds numbers, viscous effects predominate over inertial effects, implying an overdamped limit in which inertial effects relax very fast relative to the time scale of nanotube motion. As a consequence the total force, $\sum \vec{F}$, and torque, $\sum \vec{\tau}$, exerted by the fluid on the nanotube must equal zero on this time scale. This leads to a set of equations of motion that are independent of the actual fluid viscosity. This is the case because the total force and torque exerted on the nanotube equals zero and only forces of a viscous origin, eq. (6.6), are exerted on the nanotube and these are all proportional to fluid viscosity.

Given a local fluid velocity, $\vec{v}(l)$, along the nanotube, where $l \in [-L/2, +L/2]$ denotes the contour distance away from its center, inertialess motion implies zero net force,

$$\sum \vec{F} = \int_{-L/2}^{+L/2} \vec{f}(l)\, dl = 0, \tag{6.8}$$

and zero net torque,

$$\sum \vec{\tau} = \int_{-L/2}^{+L/2} l\hat{e} \times \vec{f}(l)\, dl = 0, \tag{6.9}$$

where $\hat{e}$ is a unit vector along the axis of the nanotube. Substitution of eqs. (6.6) and (6.7) into eqs. (6.8) and (6.9) yields the equations of motion for the nanotube,

$$\vec{v}_{cnt} = \frac{1}{L} \int_{-L/2}^{+L/2} \vec{v}(l)\, dl, \tag{6.10}$$

and,

$$\dot{\varphi} = \frac{12}{L^3} \int_{-L/2}^{+L/2} l v_{\perp}(l)\, dl, \tag{6.11}$$

where $v_{\perp}(l)$ is the component of the local fluid velocity which is perpendicular to the main axis of the nanotube. See fig. 6.3. Note that the equations of motion, eqs. (6.10) and (6.11), for a rod-like particle in a Stokes flow have been derived previously.[147] These equations of motion are instantaneously decoupled, that is, the instantaneous rotational velocity, $\dot{\varphi}$, and translational velocity, $\vec{v}_{cnt}$, are independent of each other as is evident from eqs. (6.10) and (6.11). This is so because rotational motion around the center of mass of the nanotube produces a local drag force proportional to $-\dot{\varphi}l$ of which the integral along the nanotube is always zero, while the net torque resulting from any translational motion is always zero for the local torque due to translational motion is again anti-symmetric in l. Note that this decoupling only holds instantaneously, translational motion does depend on the orientation of the nanotube and rotational motion depends on the position of the nanotube.

Above we reduced the interaction between a nanotube and a bubble to a two-dimensional problem. We claimed to be able to do this because translational and rotational motion within the plane spanned by the nanotube and the center of the bubble, i.e., the $x - y$ plane as defined in fig. 6.3, is independent of any rotational motion out of the $x - y$ plane. We are now able to understand this. Indeed, the net drag force resulting from any rotational motion is zero and does not affect translational motion. Rotational motion in the $x-y$ plane, as given by $\dot{\varphi}$, is not affected by rotational motion out of this plane for the torque resulting from such motion is perpendicular to the torque responsible for rotational motion in the $x - y$ plane.

With the equations of motion as given by eqs. (6.10) and (6.11) combined with eqs. (6.4) and (6.5), which describe the fluid flow during bubble collapse, we are able to investigate the interaction between a nanotube and the fluid flow during various stages of transient cavitation. In the next section we evaluate the motion of and forces exerted on a radially aligned nanotube during the transient collapse of a bubble.

6.4 Mechanics for a radially aligned nanotube during bubble collapse

Let us assume that the nanotube has a fully stretched and perfect radial conformation throughout the process of bubble collapse, with angle $\varphi = 0$ as fig. 6.3. In assuming this, we neglect the relaxation of a nanotube from an unstable tangential orientation, $\varphi = \pi/2$ in fig. 6.3, in the initial stages of bubble collapse, which has been shown to occur by Pagani et al.[134] We return to this assumption and discuss the initial relaxation from a tangential orientation briefly in the discussion, section 6.6.

Let the nanotube have length L and let its tip closest to the bubble be at a initial distance r_0 from the center of a bubble with radius R_{max} that has just undergone explosive growth and is about to collapse. During bubble collapse the nanotube will be dragged along by the fluid and the distance between the center of the bubble and the nanotube will decrease. We denote the distance between the tip of nanotube closest to the bubble and the center of the bubble as $r_{cnt}(t)$ where $r_{cnt}(t = 0) = r_0$. See fig. 6.4.

Assuming incompressibility of the fluid and a spherically symmetric fluid flow, implicit in eq. (6.4), and substituting $\vec{r}(l) = (r_{cnt} + L/2 + l)\,\hat{e}_x$, we can calculate the velocity of the nanotube straightforwardly from eq. (6.10) to give,

$$\vec{v}_{cnt} = \frac{R^2\dot{R}}{r_{cnt}\left(r_{cnt} + L\right)}\hat{e}_x, \tag{6.12}$$

where we note that R, $\dot{R}$, r_{cnt} and v_{cnt} are functions of time and that v_{cnt} is the time derivative of the tip position, r_{cnt}, so $v_{cnt} = \dot{r}_{cnt}$. Integrating eq. (6.12) over time by separation of variables, gives the nanotube position as a function of time. After rescaling all distances to R_{max}, as given by eq. (6.3) or as obtained from a numerical solution of the full Raleigh-Plesset equation, see our earlier discussion in section 6.2, the dimensionless nanotube position $y\,(t) \equiv r_{cnt}\,(t)\,/R_{max}$ obeys,

$$y^3 - y_0^3 + \frac{3}{2}\tilde{L}\left(y^2 - y_0^2\right) = x^3 - x_0^3, \tag{6.13}$$

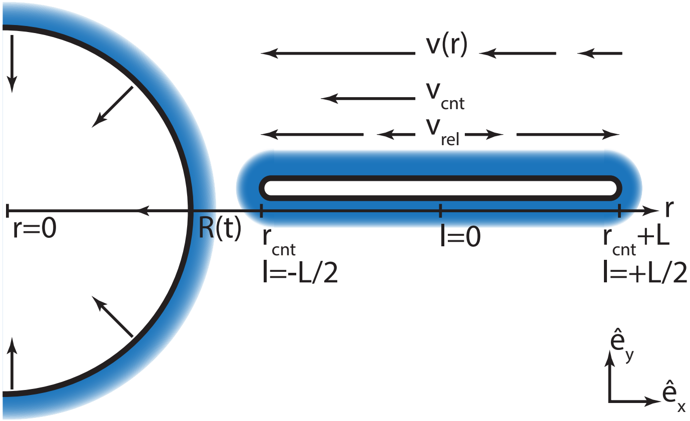

Figure 6.4: The geometry of the interaction between a radially oriented nanotube and the fluid flow following the transient collapse of a bubble with radius $R\,(t)$. The distance between the tip of the nanotube, of length L, closest to the bubble and the center of the bubble is denoted by $r_{cnt}(t)$. The directions as given by $\hat{e}_x$ and $\hat{e}_y$ and the parameter l are as defined in fig. 6.3. Above the nanotube the direction and magnitude of the actual fluid velocity $v\,(r)$, eqs. (6.4) and (6.5), the nanotube velocity, eq. (6.12), and the relative fluid velocity along the nanotube, eq. (6.7), are shown.

where $x = R\,(t)\,/R_{max}$ is the dimensionless bubble radius that we calculate from eq. (6.5), $x_0 = 1$ for it is the value of x at the start of bubble collapse, $y_0 = r_0/R_{max}$ is the dimensionless distance between the center of the bubble and the tip of the nanotube closest to the bubble at the start of bubble collapse and $\tilde{L} = L/R_{max}$ is the dimensionless nanotube length.

By way of illustration we have plotted in fig. 6.5 the motion of nanotubes of length $\tilde{L} = 0.05$ (dashed, red) and $\tilde{L} = 0.2$ (dot-dashed) for two different initial distances $y_0 = 1$ and $y_0 = 1.15$ as obtained from eq. (6.13). The values used for $\tilde{L}$ are unrealistically large but serve to highlight the dependence of nanotube motion on length and initial position. The dimensionless bubble radius, given by eq. (6.5), is depicted by the solid line. Note that for $\tilde{L} \to 0$ and $y_0 = 1$ the motion of nanotube equals the motion of the bubble wall. From fig. 6.5 it is clear that nanotubes cannot keep up with the wall of the collapsing bubble and that the nanotubes slow down as their length and/or initial distance from the bubble increases. This is easily understood from eq. (6.10) that equates the nanotube velocity to the average of the local fluid velocity along the nanotube. Because the local fluid velocity decreases with distance as r^{-2}, nanotubes become slower with increasing initial distance from the bubble *and* with increasing length.

Having established where the nanotube is relative to the bubble from the moment it starts to collapse, we are now able to evualuate the maximum stress it is subjected

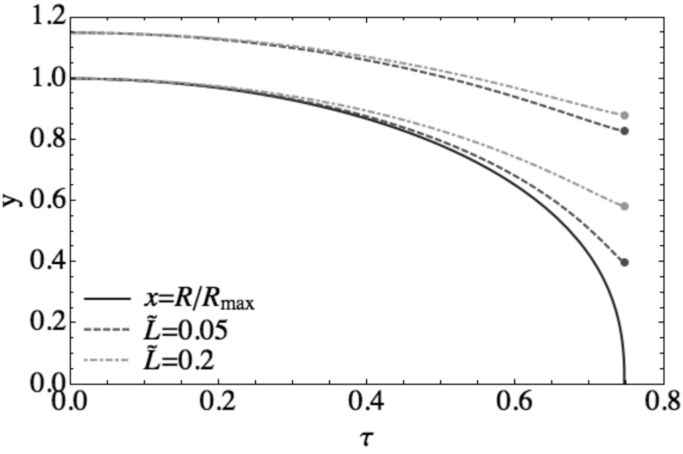

Figure 6.5: The position of the tip of a nanotube scaled to R_{max} as a function of dimensionless time, τ, during bubble collapse. The dimensionless bubble radius x, eq. (6.5), is indicated by the solid line. Nanotube motion as given by eq. (6.13) is shown for $\tilde{L} = 0.05$ (dashed) and $\tilde{L} = 0.2$ (dot-dashed) for an initial distance of $y_0 = 1$ and $y_0 = 1.15$.

to by the surrounding fluid as it is dragged along by the fluid during the collapse of the bubble. During bubble collapse the nanotube's velocity equals the average local fluid velocity along the nanotube because this ensures that the net force exerted on the nanotube equals zero. This is a consequence of inertialess motion that we used to derive the translational equation of motion, eq. (6.10) and eq. (6.13). Although the net drag force experienced by the nanotube vanishes, viscous friction does exert a large stress on the nanotube. The *relative* fluid velocity along the part of the nanotube closest to the bubble is directed radially inward while that furthest away is directed outward. See fig. 6.4. The stress exerted by the fluid is at a maximum at the point on the nanotube where the local fluid velocity, eq. (6.4), is equal to the nanotube velocity, eq. (6.12), and the relative fluid velocity is zero. Equating eqs. (6.4) and (6.12), we find that the relative fluid velocity is zero and the stress on the nanotube maximal at a distance $r^*(t)$ from the center of the bubble,

$$r^*\left(t\right) = \sqrt{r_{cnt}\left(t\right)\left(r_{cnt}\left(t\right) + L\right)}. \tag{6.14}$$

Note that r^* is time-dependent as we are following the nanotube as it is dragged along by the fluid flow following the collapsing bubble. In section 6.5 we show r^* corresponds to a point on the nanotube that is close to center of mass of the nanotube.

The maximum stress on the nanotube, i.e., that at r^*, where the relative fluid velocity equals zero, is given by the difference of the forces exerted by the fluid on the segment of the nanotube where the relative fluid velocity is directed radially inward and the segment where it is directed radially outward, divided by A, the cross sectional area of the nanotube. The force exerted on each of these two segments is equal in magnitude but opposite in direction, again, ensuring that the motion of the nanotube is inertialess. The magnitude of this force is then given by the absolute value of the integral of eq. (6.6) along one of these two segments, where $\vec{v}_{rel}$ is given by eqs. (6.7) and (6.12). In dimensionless form we find for the maximum stress on the nanotube at r^*,

$$\tilde{\sigma}_* = \sqrt{x - x^4}\left(\frac{1}{\sqrt{y}} - \frac{1}{\sqrt{y + \tilde{L}}}\right)^2, \tag{6.15}$$

where $\tilde{\sigma}_* = \sigma_*/\sigma_0$ is the dimensionless stress with σ_0 the characteristic stress scale as determined by experimental settings,

$$\sigma_0 = \frac{4\pi\mu R_{max}}{A}\sqrt{\frac{2p}{3\rho}}, \tag{6.16}$$

where μ is the dynamic viscosity of the liquid, R_{max} the bubble radius just before the start of the collapse of the bubble, A is the cross sectional area of the nanotube, p is the (static) pressure difference between the interior of the bubble and the surrounding liquid and ρ is the mass density of the liquid. Both y and $\tilde{\sigma}_*$ are functions of x, $\tilde{L}$ and y_0, so time enters implicitly. However, unlike eq. (6.13), which is independent of the time-dependence of $x(t)$, eq. (6.15) only holds for $x(t)$ as calculated from Rayleigh's model for the collapse of an empty cavity, eq. (6.5). Note that eq. (6.14) was derived previously by Ahir et al.,[127] who also derived an equation for the maximum stress on the nanotube. Their expression for the maximum stress exerted on the nanotube differs from our eq. (6.15) because we explicitly model the fluid velocity using Rayleigh's model for the collapse of an empty cavity and explicitly take nanotube motion into account through eq. (6.13).

Given the values of $\tilde{L}$ and y_0, nanotube motion is given as a function of x by eq. (6.13). Substitution of this into eq. (6.15) yields the stress at $r^*(t)$ as a function of $x(t)$. At some value of x the stress at r^* will be at a maximum, denote this value as $x = x_{max}$. Substitution of x_{max} into eq. (6.15) yields the maximum stress, $\tilde{\sigma}_*^{max}$, experienced by the nanotube during bubble collapse as a function of its dimensionless length and initial distance to the center of the bubble,

$$\tilde{\sigma}_*^{max}\left(\tilde{L}, y_0\right) = \max\left[\tilde{\sigma}_*\left(x; \tilde{L}, y_0\right), 0 < x < 1\right]. \tag{6.17}$$

We have not been able to obtain an analytic expression for $\tilde{\sigma}_*^{max}$, so we determine it numerically. In fig. 6.6, $\tilde{\sigma}_*^{max}$ is shown as a function of $\tilde{L}$ and y_0, the relation between the three parameters contains important information regarding the scission mechanics. A line over the surface at $y_0 = 1$ gives the dimensionless minimum nanotube length for which scission can occur as a function of dimensionless tensile strength, while lines at constant $\tilde{\sigma}_*^{max}$ give the dimensionless maximum initial distance between the nanotube and the bubble for which scission can occur as a function of dimensionless nanotube length. The scission rate is related to this maximum initial distance.

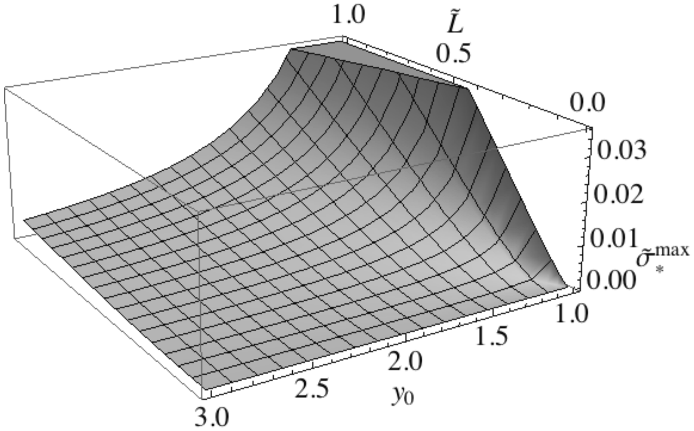

Figure 6.6: The maximum dimensionless stress exerted on a nanotube during bubble collapse, $\tilde{\sigma}_*^{max}$, as a function of the dimensionless nanotube length, $\tilde{L}$, and the dimensionless distance, y_0, between the nanotube and the center of the bubble at the time of the start of the bubble collapse.

In summary, we have shown that the motion of a stretched and radially aligned nanotube during bubble collapse is determined by its length and initial distance away from the center of the bubble. As the fluid strain rate around the nanotube depends on the nanotube's position, the maximum stress experienced by a nanotube is determind by, again, its length and initial position as well as the sonication conditions through the characteristic stress scale σ_0. In the next section we show how the minimum scission length and the scission rate can be determined from fig. 6.6.

6.5 Implications for scission kinetics

In the previous section the motion of a radially oriented nanotube and the forces exerted on it during bubble collapse were calculated. The analysis resulted in fig. 6.6, which gives the maximum stress exerted on the nanotube as a function of its length and of its initial distance away from the center of the bubble at the time of the start of the bubble collapse. From this figure it is clear that the maximum stress experienced by a nanotube increases with decreasing initial distance to the center of the bubble.

A nanotube of a given length then experiences a maximum stress when it starts out as close as possible to the surface of the bubble. The smallest initial distance between nanotube and bubble center allowed for in the model is $y_0 = 1$. Given $\tilde{L}$, the maximum dimensionless tensile strength, $\tilde{\sigma}_T$, of a nanotube of that length that will still break under sonication is given by $\tilde{\sigma}_T = \tilde{\sigma}_*^{max}\left(\tilde{L}, y_0 = 1\right)$, of which the value can be obtained by numerically solving eq. (6.17). The shortest nanotube segments produced by sonication, the so-called terminal length, then depends on sonication conditions and the tensile strength of the nanotube. As we show below, scission occurs very close to the center of the nanotube, so the dimensionless terminal length is in good approximation equal to $\tilde{L}_{min}/2$, where $\tilde{L}_{min}$ is the dimensionless minimum scission length. The relation between the minimum scission length and tensile strength, as numerically determined from eq. (6.17), can be fitted to a power law. The resulting power law in dimensionless form is,

$$\tilde{L}_{min} \approx 7.04\tilde{\sigma}_T^{1/1.16}, \tag{6.18}$$

where $\tilde{\sigma}_T = \sigma_T/\sigma_0$ is the dimensionless tensile strength of the nanotube, with σ_0 as given by eq. (6.16). The power law is an excellent fit, as is shown in fig. 6.7. The relative error of the power law to the numerically determined values is smaller than 5 percent over 7 orders of magnitude in $\tilde{L}$.

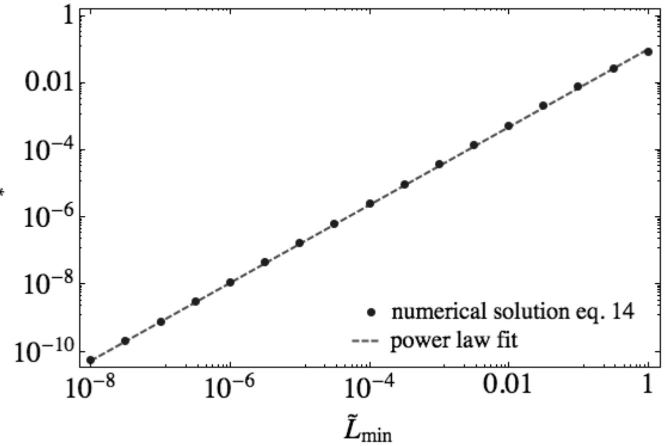

Figure 6.7: The dimensionless minimum scission length, $\tilde{L}_{min}$, as a function of the dimensionless tensile strength, $\tilde{\sigma}_T$. The dots represent numerical solutions of $\tilde{\sigma}_T = \tilde{\sigma}_*^{max}\left(\tilde{L}_{min}, y_0 = 1\right)$. The dashed curve represents the power law as given by eq. (6.18).

Eq. (6.18) shows a stronger dependence of the terminal length on tensile strength than the previously predicted scaling of $L_{min} \propto \sigma_T^{1/2}$, which was obtained by neglecting nanotube motion and assuming a constant fluid strain rate along the nanotube.[38,126,127,129,130] In this approximation, the average relative fluid velocity along the nanotube scales with L and the total length over which viscous drag forces are exerted scales with L resulting in an L^2 scaling for the stress exerted on the nanotube. The stronger dependence obtained from our calculations results from the dependence of the maximum fluid strain rate along the nanotube on the length of the nanotube. As is illustrated in fig. 6.5, the velocity of a nanotube decreases with increasing length. Longer nanotubes are not dragged along as easily as short ones during bubble collapse and their distance to the center of the bubble remains larger. Because the strain rate of the fluid flow scales with the reciprocal distance cubed, longer nanotubes experience smaller fluid strain rates. This results in a smaller increase in the maximum stress exerted on a nanotube with increasing nanotube length and thus a stronger increase of terminal length with increasing tensile strength.

When the dimensionless initial distance between a nanotube of length L_{min} and bubble increases beyond $y_0 = 1$, the maximum stress exerted on the nanotube decreases as is evident from fig. 6.6. An increase in nanotube length is required if the stress exerted on the nanotube is to exceed the tensile strength of the nanotube. As a result, there is a critical, length-dependent, maximum initial distance from the center of the bubble, $r_{max}(L)$, beyond which scission can not occur for nanotubes of length less than L.[134] For nanotubes of tensile strength σ_T, scission occurs when $\sigma_*^{max} \geq \sigma_T$. The dimensionless maximum initial distance for which scission of a nanotube of dimensionless tensile strength $\tilde{\sigma}_T$ occurs, y_{max}, can be read off from fig. 6.6 by taking the intersection of the horizontal plane of constant $\tilde{\sigma}_T = \tilde{\sigma}_*^{max}$ and the plotted surface. In fig. 6.8 the dimensionless critical initial distance, y_{max} is shown as a function of dimensionless nanotube length for various values of $\tilde{\sigma}_T$, as obtained by numerically solving $\tilde{\sigma}_*^{max}\left(\tilde{L}, y_{max}\right) = \tilde{\sigma}_T$ for y_{max} as a function of $\tilde{L}$. For nanotubes significantly longer than the minimum length a clear power law with slope $2/3$ is obtained for all values of $\tilde{\sigma}_T$. This is to be expected because when the nanotube starts out at a sufficiently large distance from the bubble it will not be dragged to region of high fluid strain rate during bubble collapse, and the strain rate of the fluid flow, $\dot{\epsilon}$, as experienced by the nanotube becomes independent of nanotube length and scales with distance as $\dot{\epsilon} \propto r^{-3}$. The stress experienced by the nanotube scales as $\dot{\epsilon}L^2$, so the critical distance must scale as $r_{max} \propto L^{2/3}$.

For very short nanotubes the strain rate must be significantly larger than the strain rate experienced by long nanotubes if scission is to occur. Such an increase in the strain rate occurs for short nanotubes that are close to the surface of the bubble at the point in time when bubble collapse commences. During bubble collapse these short nanotubes are easily dragged along by the fluid flow to distances typically less than $0.1R_{max}$ from the center of the bubble. This results in a significant increase in the experienced strain rate because the strain rate scales with distance as r^{-3}. If we consider a slightly longer nanotube, scission occurs at a lower strain rate of the fluid. However, the maximum strain rate experienced by a nanotube decreases with increasing nanotube length for longer nanotubes are not dragged along as easily. As a result, the allowed increase in the initial distance between nanotube and bubble

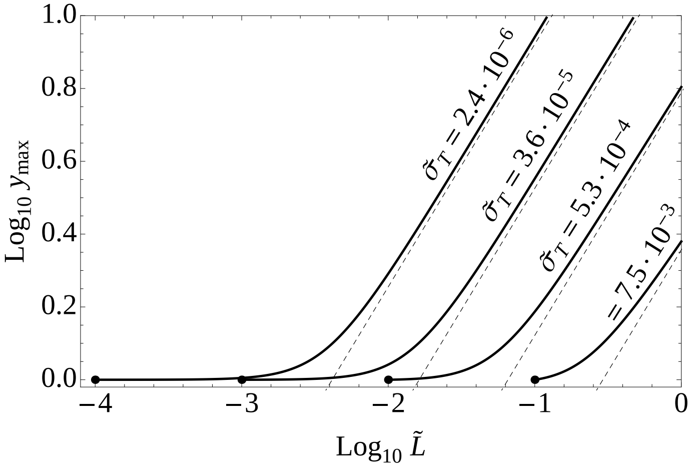

Figure 6.8: The dimensionless maximum initial distance, y_{max} for scission to occur as a function of dimensionless nanotube length $\tilde{L}$ for various values of dimensionless tensile strength, $\tilde{\sigma}_T$. Dots show the minimum nanotube length for scission to occur. Dashed lines indicate a power law with exponent $2/3$.

cannot increase as strongly as it would if the maximum strain rate of the fluid flow experienced by the nanotube is independent of the nanotube length. The critical distance remains close to $y_{max} = 1$ for a large range of nanotube lengths as shown in fig. 6.8 and deviates from a power law with slope $2/3$ as the maximum strain rate experienced by a nanotube becomes dependent on nanotube length. As we shall shortly see, this has an important consequence, the previously predicted L^2 scission rate[126, 134] breaks down near the terminal length, causing the scission kinetics to become non-universal.

Let us now consider how we can derive the scission rate of nanotubes in solution from these findings. If scission occurs when a nanotube of length L starts out at a distance less or equal to $r_{max}\left(L\right)$ away from the center of a bubble, then the scission rate, $k\left(L\right)$, of a nanotube of length L must be proportional to the probability that a nanotube is found within a distance $r_{max}\left(L\right)$ of the center of a bubble at the moment the bubble starts to collapse. Assuming a homogeneous spatial distribution of nanotubes, this probability is proportional to the 'scission volume' enclosed between spheres of radius R_{max} and $r_{max}\left(L\right)$. We surmise that the scission rate must then obey,

$$k(L) \propto \left(r_{max}\left(L\right)^3 - R_{max}^3\right), \tag{6.19}$$

where the proportionality constant is equal to the number of transiently collapsing bubbles per unit time per unit volume and the scission rate, $k\left(L\right)$, gives the fraction of nanotubes of length L that undergo scission per unit time. Note that Pagani et al. used similar arguments to derive a scission rate.[134] Let us now focus on the implications for scission kinetics. In fig. 6.9, the dimensionless scission rate, $\tilde{k}\left(\tilde{L}\right) \propto k\left(\tilde{L}\right) R_{max}^3$, is plotted as a function of dimensionless nanotube length for the same values of $\tilde{\sigma}_T$ as presented in fig. 6.8. Here, we have set the dimensionless proportionality constant equal to unity. We can do this, because using its actual value merely shifts the curves upward or downward in the double logarithmic plot.

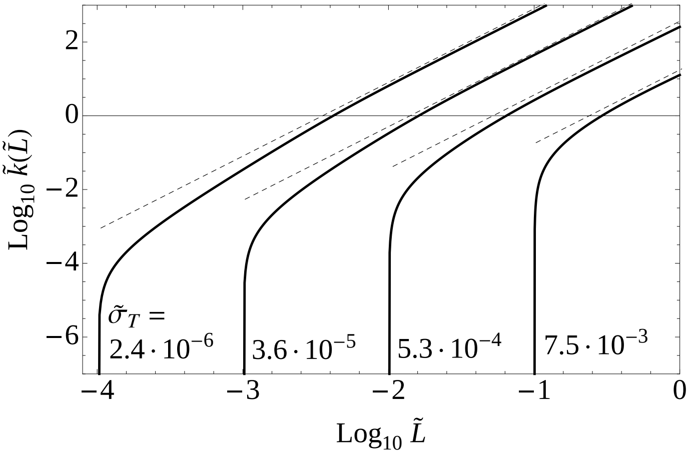

Figure 6.9: The dimensionless scission rate, $\tilde{k}\left(\tilde{L}\right)$ as a function of dimensionless nanotube length $\tilde{L}$ for the same values of dimensionless tensile strength $\tilde{\sigma}_T$ as presented in fig. 6.8. The dashed lines correspond to a power law with exponent 2.

Fig. 6.9 shows that the previously derived L^2 scission rate[126,134] breaks down for lengths within an order of magnitude above the minimum scission length while this power law still holds for sufficiently long nanotubes. This is indeed what we expect, because from fig. 6.8 we know that nanotube motion only affects the scission mechanics for sufficiently short nanotubes and hence that, the L^2 power law, derived by neglecting nanotube motion must hold for sufficiently long nanotubes. The break down of the universal L^2 power law scission rate for the last three or four scissions before the nanotube reaches a length below the minimum scission length has an important consequence, a non-power law scission rate will yield non-universal scission kinetics. In the discussion, section 6.6, we will see that this can potentially explain the non-universal scission kinetics as reported in literature.[122,126,130,132]

The scission rate, as shown in fig. 6.9, goes to zero at the minimum scission length within our approximation for the minimum scission length is obtained when $y_{max} = 1$, and hence $r_{max}\left(L_{min}\right) = R_{max}$. The assumption of a homogeneous nanotube distribution is however tenuous, because nanotubes tend to be concentrated near the surface of the bubble during explosive growth. This happens to be the case, because the nanotubes are slower than the expanding bubble for the same reasons as why the nanotubes cannot keep up with the bubble during bubble collapse. By taking this effect into account, one would arrive at a non-zero scission rate for nanotubes of a length equal to the minimum scission length, L_{min}. However, we choose not to take this into account as it does not qualititatively change the predicted scission rate, while it would require us to model nanotube motion during the explosive growth of the bubble.[4]

Fig. 6.9 shows that the nanotube properties and the experimental settings determine the length-dependent scission rate through the parameters R_{max} and σ_0 predicted by eqs. (6.3) and (6.16) respectively. Although that for nanotube lengths far larger than L_{min}, we do obtain a universal power law with exponent 2, the behaviour at lengths close to L_{min} is non-universal. Here scission only occurs because the nanotube is dragged along by the fluid to regions with high strain rate. Transport of the nanotube over a significant length is only possible if the nanotube is short compared to the bubble radius. The smaller $\tilde{L}_{min}$, the larger the length range over which transport is significant and the larger the region over which deviations from the universal power law are observed.

It is clear now that scission occurs only if the nanotube is sufficiently long and if it is sufficiently close to a bubble. To determine the time-evolution of the nanotube length distribution we need to know at which point on the nanotube scission will occur. In section 6.4 we saw that if the nanotube is at a distance of a bubble, the stress on the nanotube is at a maximum on the point on the nanotube that is at a distance r^* from the center of the bubble, where r^* is given by eq. (6.14). It is insightful to define a relative scission position, r_{cnt} from the center

$$r^*_{rel}(t) = \frac{r^*(t) - r_{cnt}(t)}{L}, \tag{6.20}$$

where we note that the position of the nanotube is time-dependent as it is dragged along by the fluid during bubble collapse, and as a consequence of that, the position of maximum stress, r^*, is also time-dependent. The relative scission position is 0.5 if scission occurs at the center of mass of the nanotube, it is 0 for scission at the tip closest to the bubble ($l = -L/2$) and 1 for scission at the far end of the nanotube ($l = L/2$).

To plot the relative scission position, r^*_{rel}, we solve eq. (6.17) numerically as a function of $\tilde{L}$ and y_0 to determine the bubble radius, x_{max} at which the stress exerted on the nanotube is at a maximum. Substitution of x_{max} into eq. (6.13) produces the corresponding value of r_{cnt}, which, after substitution into eq. (6.20) gives the relative scission position. This we plot in fig. 6.10 as a function of $\tilde{L}$ and y_0.

---

[4] We checked this by modelling nanotube motion during explosive growth of the bubble by calculating the motion of a nanotube with an orientation tangential to the bubble surface. The result allows us to calculate the distance away from the center of the bubble at the start of explosive growth, d_i, for which the nanotube will be at a distance r_{max} from the center of the bubble at the end of explosive growth. We calculate the scission rate by assuming it is proportional to d_i^3. The resulting scission rate has a non-zero value at the the minimum scission length, L_{min}, but is qualitatively identical to the scission rate as derived by neglecting nanotube motion during explosive growth of the bubble.

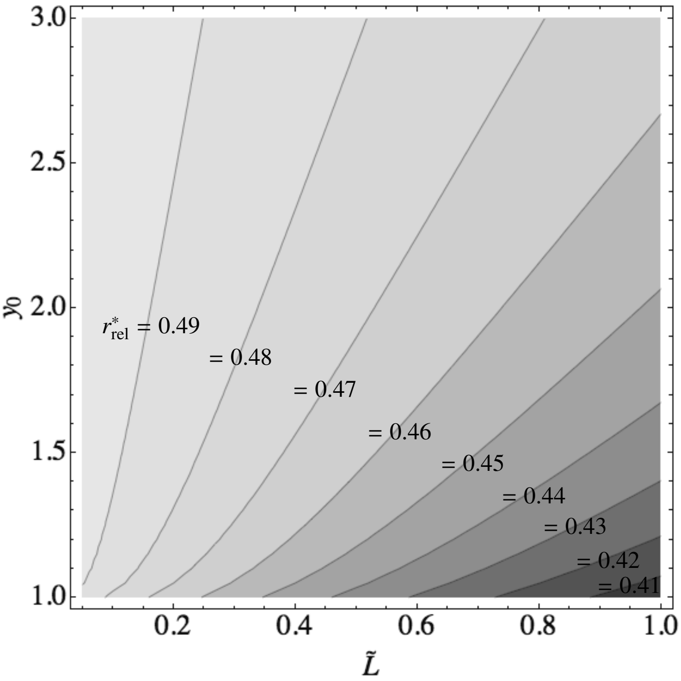

Figure 6.10: Contour plot of the relative scission position, r^*_{rel}, as a function of dimensionless nanotube length, $\tilde{L}$, and dimensionless initial distance between nanotube and bubble at the start of the collapse of the bubble, y_0.

Note that, a nanotube with a higher tensile strength will not break for these values of $\tilde{L}$ and y_0, while scission of a nanotube with a lower tensile strength will occur at an earlier moment and thus at a larger value of r_{cnt}. From eq. (6.20) follows that, the relative scission position, r^*_{rel}, increases with r_{cnt} up to a value of 0.5 for $L/r_{cnt} \to 0$. So, any nanotube with a tensile strength smaller than $\sigma^{max}_{*}\left(\tilde{L}, y_0\right)$ will undergo scission at a point closer to its center than indicated in fig. 6.10. As, for a typical sonication experiment, we have $\tilde{L} = 1.5 \cdot 10^{-3}$ corresponding to a nanotube of a length of approximately 1 μm, scission indeed occurs very close to the center of the nanotube.

6.6 Discussion

In the preceding two sections the mechanics of nanotube scission under tension has been investigated. Key results of the analysis are, 1) an expression for the terminal length, i.e., the length of the shortest nanotube segments that can be reached by means of sonication, 2) the derivation of a non-universal length-dependent scission rate which provides an explanation alternative to the one of Pagani et al.[134] for the experimentally observed non-universal scission kinetics, and 3) the determination of the scisson position. We showed that the motion of a nanotube during the collapse of a bubble leads to non-universal scission kinetics and affects the scaling of the terminal length with the tensile strength of the nanotube.

Let us first discuss the key assumption underlying our findings, being that nanotubes are oriented radially during bubble collapse. Simulations by Pagani et al.[134] indicate that a nanotube relaxes in the initial stages of bubble collapse from an unstable tangential orientation to either a stretched radial conformation through rotation or to a highly bent conformation after buckling. They showed that relaxation by reorientation is favoured by short nanotubes while longer ones bend and buckle. They argued that this is what one would expect, because the time scales at which relaxation by reorientation and by bending and subsequent buckling occurs, scale differently with the length of the nanotube. Indeed, reorientation of the nanotube requires the breaking of symmetry through rotational diffusion, for a perfectly straight and tangentially oriented nanotube in a perfectly radial fluid flow experiences a net torque of zero. While rotational diffusion slows down with increasing nanotube length and hence the probability of relaxation by reorientation, the propensity to buckle increases with length. This suggests that our model only holds for sufficiently short nanotubes.

We argue that this is not necessarily always the case. Indeed, neglected in the analysis by Pagani et al. is, firstly, the potential presence of defects in the nanotube structure, making them not quite straight and resulting in a break of symmetry. Secondly, fluctuations in the fluid flow, caused for example by other nearby bubbles, can cause a break in the spherical symmetry of the fluid flow. Both of these effects promote the relaxation of longer nanotubes into a stretched radial conformation through a break of symmetry as longer nanotubes arguably contain more defects and are more prone to interact with asymmetries in the fluid flow because they interact with a larger volume of the fluid. Note also that the time scale of both relaxation mechanisms is of the same order of magnitude, as the assumption of Stokesian dynamics ensures that it is the fluid flow that dictates the time scale of any type of motion. Because of this, we argue that short nanotubes reorient into a radial orientation and scission of these nanotubes is well described by our model, and that for long nanotubes both scission under tension and scission due to overbending can occur. The predominant mechanism is determined by the lack or presence and degree of symmetry breaking during bubble collapse, meaning that an understanding of both scission under tension and scission due to overbending is important for nanotubes of all lengths.

While an analysis of the competition between the two scission mechanisms is beyond the scope of this paper and most likely beyond the scope of analytical theory, it is tempting to speculate about combined breaking scenarios. For instance, even if the nanotube relaxes into a perfectly symmetric and highly bent conformation after buckling, there must still be a competition within the same nanotube between scission due to overbending and scission under tension. The scission under tension mechanism operates on the two highly bent halves of the nanotube, which are aligned nearly radially and thus under high tension. Scission under tension in one of these halves would now result in a segment of a length of a quarter and a segment of three quarters of the length of the nanotube prior to scission. This is of course no more than qualitative reasoning and in the next chapter we shall see that a nanotube which is significantly bent in a number of places will undergo scission under tension if the tensile strength is sufficiently small.

We return now to the question how the minimum scission length predicted by our theory and given by eq. (6.18) differs from earlier work. Firstly, because we take the previously neglected motion of a nanotube during bubble collapse explicitly into account, we find an exponent of $1/1.16$ that differs from the value of $1/2$ predicted earlier.[126, 127, 129, 130] Secondly, we explicitly relate the minimum scission length to the sonication settings and the tensile strength of the nanotube. Interestingly, the minimum scission length scales with the radius of a bubble just prior to it start to collapse as $L_{min} \propto {R_{max}}^{0.14}$. This weak dependence of the minimum scission length on R_{max} suggests that there is indeed a well-defined terminal length, which equals approximately half the minimum scission length, even if there is some spread in the size of the transiently collapsing bubbles.

It is however doubtful whether the terminal length is observed in experiments.[130] Experiments show a power law relation between the average length of nanotubes and the time for which they have been sonicated,[122, 126, 130, 132] suggesting that the terminal length has not been reached in these experiments. Indeed, when a significant number of the nanotubes have a length close to the minimum scission length, one would expect the number of nanotubes with a length above the minimum scission length to decrease exponentially over time. This is because scission of these nanotubes is essentially a first-order ‘reaction’ in which the nanotubes go from being able to undergo scission to being unable to undergo scission, for after scission the resulting segments have a length below the minimum scission length. Intuitively one would expect the power law relating average length to time to break down if the number of the nanotubes available to undergo scission starts to decrease exponentially. This discrepancy is possibly resolved by our work, which shows the scission rate to decrease by several orders of magnitude when the length of the nanotubes approaches the minimum scission length, see fig. 6.9. This suggests that experimental time scales might indeed be too short to observe the terminal length.

The experimentally observed power law relation between the average nanotube length and sonication time[122, 126, 130, 132] has been reproduced by a simple kinetic model for a power law scission rate.[130, 134] In this kinetic model the length-dependent scission rate is assumed to obey a simple power law, $k\left(L\right) \propto L^{1/\alpha}$, meaning that there is no terminal length below which scission stops in this kinetic model. By treating the scission of nanotubes as a first-order reaction, and by assuming an initially monodisperse length-distribution and finally by imposing conservation of carbon nanotube mass, one can derive that the average length must scale with sonication time as $\langle L\rangle \propto t^{-\alpha}$. This, in light of our discussion so far, is a remarkable result. By assuming that there is no terminal length the experimentally observed power law decrease of the average length over time is reproduced, which, again, suggests that the terminal length is not reached on experimental time scales.

We can use the same simple kinetic model to compare the results of our model with experimental results. Let us first consider the situation where all nanotubes have a length well above the minimum scission length. Here, our model predicts that the scission rate is a power law with exponent $\alpha^{-1} = 2$ and the kinetic model predicts the power law relating average length and sonication time to have an exponent of $\alpha = 0.5$, in agreement with some experimental results.[126] However, an experimentally determined value of $\alpha = 0.22$ has also been reported,[130] which corresponds to a slow down of the scission kinetics as compared to the situation where $\alpha = 0.5$.

This is potentially explained by our model, which predicts the scission kinetics to slow down significantly near the minimum scission length, as compared to the situation where the scission rate is an L^2 power law, for here our model predicts the scission rate to deviate from a pure power law with exponent $\alpha^{-1} = 2$. This deviation from a power law is significant in terms of scission kinetics. For a power law, the scission kinetics must be identical at all length scales while this is not necessarily true for a non-power law scission rate. This suggests that the scission kinetics depends on how many of the nanotubes are sufficiently close to the terminal length to have their scission governed by the non-power law region of the scission rate as predicted by our model. Interestingly, our model predicts that deviations from an 0.5 power law occur when close to the terminal length, this is in contradiction with the work by Pagani et al.[134] who predict that the scission rate of long nanotube that buckle and break deviates from an 0.5 power law and follows an 0.25 power law. Unfortunately, the current kinetic model is too simple to come to a sensible comparison of our model with experimental results. The kinetic model only allows for the analysis of a simple power law scission rate and does not take the existence of a terminal length into account and hence is not suited to the analysis of the results of our model. Although our model certainly predicts the scission kinetics to be slower than an 0.5 power law when close to the terminal length, we believe that a more thorough study of the scission kinetics, using a more advanced kinetic model, is required to see if our model can reproduce the experimentally observed exponent of 0.22. This, we intend to pursue in the near future.

We end this paper with a discussion of the connection between sonication and exfoliation, where we recall that scission is an unwanted by-effect of sonication. Any attempt to optimise the sonication process requires an understanding of both the mechanics and kinetics of exfoliation and scission. The exfoliation of single-wall carbon nanotubes bundles has been attributed to the diffusion of surfactant molecules into nanotube bundles after cracks are formed in these bundles by means of sonication. When a surfactant layer has formed between a nanotube and the bundle it is part of, this nanotube is separated from the bundle.[118,119] Here, we would like to propose a different mechanism. If nanotube bundles orient into a radial orientation during bubble collapse, just as individual nanotubes do, scission of a nanotube in the outer layer of the bundle can occur when the stress exerted by the fluid flow exceeds the tensile strength of the nanotube. After scission has occured, the fluid exerts large drag forces on each of the resulting nanotube halves. If these drag forces exceed the binding force between bundle and nanotube segment, the nanotube segments slide off the bundle and are separated from the bundle. In this scenario exfoliation relies on nanotube scission as is illustrated schematically in fig. 6.11. If this process is indeed responsible for the exfoliation of nanotube bundles, then the sonication process can be optimised. The sonication power should be just sufficient to cause scission of nanotube in the outer layer of the bundle, while it should be insufficient to cause the scission of the resulting nanotube segments that have a length approximately equal to half the length of the nanotubes in the bundle. Here, a more thorough analysis is required that we will pursue in the near future.

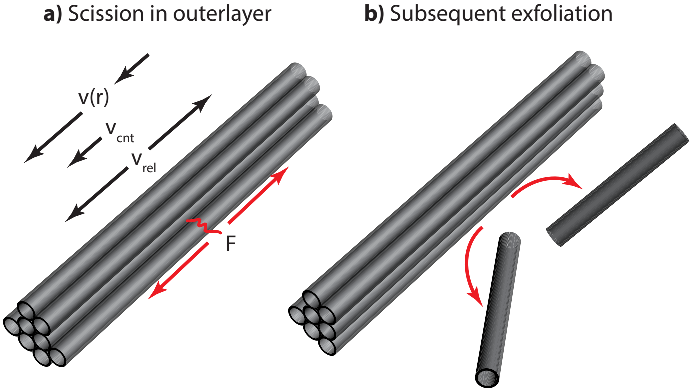

Figure 6.11: The exfoliation of a nanotube rope by scission of individual nanotubes in the outer layer. Nanotube ropes will be dragged along by the fluid flow following the transient collapse of a bubble just like a single nanotube. Strong gradient in the fluid velocity results in a large stress exerted on the nanotubes on the outer layer of the rope, possibly causing scission of these nanotube. After scission the two resulting segments will be ‘pulled of’ the bundle if the drag force exerted by the fluid flow exceeds the binding force between the nanotube segment and the bundle.

In conclusion, we have shown that scission of nanotubes under tension during bubble collapse does not result in universal scission kinetics. This can potentially explain the variety in the experimentally observed scission kinetics and is in contrast with previous work on scission under tension in which scission under tension was thought to result in universal kinetics. Given the length-dependent scission rate, eq. (6.19), the lengths of the segments resulting from scission, eq. (6.20), and the terminal scission length, eq. (6.18), the scission kinetics and the time-evolution of the length distribution are fully determined, allowing, in principle for controlled manipulation of the length distribution. Finally, if exfoliation is indeed scission-mediated, knowledge of both scission and exfoliation kinetics will allow for optimisation of the sonication process.

Chapter 7

Scission mechanics of carbon nanotubes by Brownian dynamics simulations

Summary

In this chapter we investigate the mechanics of carbon nanotube scission under sonication by means of Brownian dynamics simulations.[134] In the simulations the nanotubes are modeled as a bead-rod chain, while the fluid flow around a transiently cavitating bubble is described by the Rayleigh-Plesset equation. Scission of a nanotube can occur under tension or by bending and subsequent buckling, allowing for the simulation of multiple scissions of a nanotube during a single collapse phase of the bubble. The results of the simulation show that multiple scissions indeed occur in long nanotubes. Moreover, our results suggest that the scission mechanics depend on a rich interplay between the tensile strength, the persistence length, the length of the nanotube and the maximum curvature the nanotube can sustain without breaking.

7.1 Introduction

In the previous chapter we studied the mechanics of carbon nanotube scission under tension by an analytic model. While this approach allowed for the derivation of a number of analytical equations describing the motion and stresses on a nanotube, it did not include rotational motion of the nanotube nor scission caused by bending and buckling. In this chapter we study the interaction of a single nanotube with a single bubble undergoing transient cavitation by Brownian dynamics simulations. This approach does allow us to investigate the effects of bending and the rotation of the nanotube. That bending and subsequent scission by buckling are potentially an important scission mechanism is not a new idea. In fact, nanotubes with a highly bent conformation after sonication have been observed experimentally,[150] and a number of explanations for this have been offered. These include: 1) the trapping of a nanotube inside a collapsing bubble where in the final stages the interface of the bubble imposes a large compressive load on the nanotube causing buckling and scission,[150] 2) the expulsion of a nanotube from a bubble in the final stages of the collapse in an orientation tangential to the bubble surface, where the fluid flow imposes a large compressive load causing the buckling-mediated scission of the nanotube[133] and 3) a length-dependent competition of rotation to a radial orientation and scission under tension, and of the bending and buckling-induced scission of a nanotube, where scission by both mechanisms takes place in the fluid near a collapsing bubble.[134] Importantly, only the third mechanism does not rely on the nanotube getting (temporarily) trapped inside the bubble. As a consequence, this mechanism is not restricted to the negligibly small number of nanotubes that get sufficiently close to a cavitating bubble to get trapped into it. Rather, it affects a significantly larger number of nanotubes that are sufficiently close to the bubble to be exposed to some critical fluid strain rate above which buckling-mediated scission occurs.[134]

The work presented in this chapter is an extension to the work in which the length-dependent competition between scission under tension and buckling-mediated scission was proposed.[134] The Brownian dynamics simulation employed in that study is extended in this chapter to allow for the explicit scission of the nanotubes. An important advantage of this approach, that was already recognised in the previous work,[151] is that it allows for simulation of the motion of the nanotube fragments resulting from scission. If these fragments are exposed to stresses or degrees of bending that cause scission of these fragments themselves, scission occurs in our simulation. Hence, by allowing for explicit scission we can determine whether a nanotube will break more than once during the collapse of a single bubble.

We shall show that if the nanotube is sufficiently long this can indeed occur. This has important consequences for the scission kinetics, which are traditionally modeled by presuming that a single interaction between a nanotube and a collapsing bubble leads to a single scission of the nanotube at the most.[126,127,130,133,134] Moreover, we show and argue that the exact scission mechanics are determined by a rich interplay between 1) the length of the nanotube and its persistence length, determining the number of places in which it can buckle, and 2) the length of the nanotube and its tensile strength, dictating the minimum scission length for scission under tension, discussed in chapter 6, and hence the number of places in which it can break under tension, and 3) the length of segments that are free from significant bending relative to the minimum scission length for scission under tension, which determines if scission under tension can occur.

Before we can address this interplay between these properties of the nanotubes in detail, we must first discuss the simulation method. In section 7.2 we discuss the simulation of the dynamics of a bubble undergoing transient cavitation and the fluid flow generated by this. In contrast to the approach taken in the previous chapter, where the bubble dynamics are modeled by the (rescaled) empty cavity approximation,[145] we here use the full Rayleigh-Plesset equation[40] because it allows us to include the explosive growth phase of transient cavitation in the simulation and because it is more accurate. In section 7.3 we briefly discuss the Brownian dynamics simulation of the carbon nanotube, which is modeled by a bead-rod model,[152–154] and we discuss the criteria for which a nanotube undergoes scission and the implementation of explicit scission in the simulation. Finally, in section 7.4 we present the results of the simulations and in section 7.5 we discuss the implications of these results for the scission mechanics and kinetics.

7.2 Bubble dynamics & Rayleigh-Plesset equation

The method by which the bubble dynamics are simulated was previously developed and the implementation in the simulations we perform has remained unchanged.[134, 151] In this section, we give a brief overview of the implementation of the bubble dynamics and how the Rayleigh-Plesset equation is solved in the simulation. Here, we use the Rayleigh-Plesset equation[40] to model the bubble dynamics rather than the (rescaled) empty cavity approximation,[145] as introduced in chapter 6.2, because it allows for the simulation of the growth phase of the bubble. Moreover, the simulation is inherently numerical, so unlike for the work presented in chapter 6, it is not crucial to have an analytical relation between the bubble radius and the rate at which the bubble radius changes. Because of this, it is preferable to use the more accurate and physically more realistic Rayleigh-Plesset equation that unlike the empty cavity approximation does take viscous effects, a time-dependent acoustic field, surface tension and inertial effects into account.

The Rayleigh-Plesset equation is given by

$$\rho\left(R\ddot{R}+\frac{3}{2}\dot{R}^2\right)+\frac{2\sigma}{R}+4\mu\frac{\dot{R}}{R}+p_0-p(t)-p_{bubble}=0, \tag{7.1}$$

where $R=R(t)$ is the bubble radius, $\dot{R}(t)$ the velocity of the bubble wall, $\ddot{R}(t)$ the acceleration of the bubble wall, $\rho=10^3$ kg/m^3 the mass density, $\sigma=40.1$ mNm^{-1} its surface tension, $\mu=10^{-3}$ Pa s its viscosity and $p_0=101$ kPa the ambient pressure in the sonication liquid. These values correspond to the properties of water under ambient conditions, where a concentration of sodium dodecyl sulfate equal to the critical micelle concentration is added.[134] A surfactant such as sodium dodecyl sulfate is typically added in sonication experiments because it stabilises exfoliated carbon nanotubes and prevents them from rebundling.[39]

Eq. (7.1) involves two time dependent pressures, the first is the applied acoustic pressure,

$$p(t) = p_a \sin(\omega t), \tag{7.2}$$

where p_a is the acoustic pressure amplitude, introduced in chapter 6.2, and ω, the frequency of the applied acoustic field. The pressure inside the bubble, p_{bubble}, depends on the bubble radius and hence on time and is the sum of the vapour pressure in the bubble, $p_V = 1750$ Pa, and the gas pressure of other molecules present in the bubble, p_{gas}.[134,151] In the simulation a distinction between two regimes with different relations between p_{bubble} and the radius of the bubble, R is made.[134,151] In the first regime, during bubble growth and the initial stages of collapse, the dynamics is presumed to be quasistatic and isothermal and the vapour pressure remains constant as water molecules freely interchange between the vapour and the liquid phase, and

$$p_{gas} = p_{gas}^{0} \left(R_i/R\right)^{3\kappa}, \tag{7.3}$$

where $p_{gas}^{0} = p_0 - p_V + 2\sigma/R_i$ is the equilibrium gas pressure inside the bubble prior to explosive growth, R_i is the initial bubble radius at that moment and $\kappa = C_p/C_v = 1.4$ is the ratio of the isobaric to the isochoric heat capacity of an ideal diatomic gas (air mostly consists of diatomic molecules). In the final stages of bubble collapse eq. (7.3) no longer holds, the collapse is then so fast and violent that the process can no longer be presumed to be isothermal and quasistatic. Instead, the process is presumed to be adiabatic and there is no longer a free exchange of solvent molecules between the vapour and liquid phase, and

$$p_{bubble} = 2p_V \left(R_{crit}/R\right)^{3\kappa}, \tag{7.4}$$

where R_{crit} is a critical radius that separates the regimes where the gas pressure is presumed to follow either eq. (7.3) and (7.4). This critical radius is reached when the gas pressure given by eq. (7.3) equals the vapour pressure inside the bubble.

The Rayleigh-Plesset equation, eq. (7.1), is solved by a fourth order Runge-Kutta method in the simulation.[134] In our simulations we presume, just as in previous simulations,[134] an acoustic pressure amplitude of 1.5 MPa and an acoustic frequency of 20 kHz, while the initial bubble radius is presumed to be equal to 1 μm, which is larger than the critical Blake radius required for the explosive growth of the bubble.[136,138,139] The resulting relation between time, the acoustic pressure and the bubble radius is shown in fig. 7.1.

The solution of the Rayleigh-Plesset equation for the parameter values previously listed and shown in fig. 7.1 has several interesting features. Firstly, it shows that bubble remains to grow even after the acoustic pressure in the liquid becomes positive and hence larger than the pressure inside the bubble. In chapter 6.2 this effect was

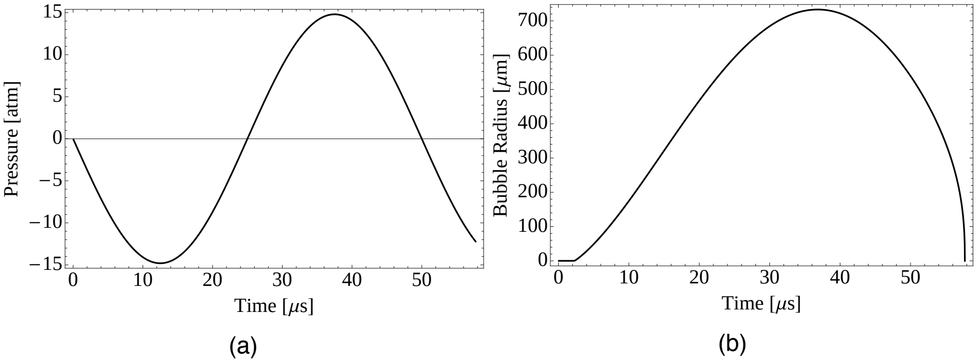

Figure 7.1: a) The applied acoustic pressure, $p(t)$, as a function of time. b) The solution of the Rayleigh-Plesset equation, eq. (7.1), for the radius of a bubble undergoing transient cavitation as a function of time for an applied acoustic field as shown in fig. 7.1a. The values of the various parameters in the Rayleigh-Plesset equation used to solve it are given in the main text.

taken into account in the calculations of the maximum radius the bubble attains at the end of its explosive growth.[139] In the final phase of bubble growth, the kinetic energy of the fluid flow that is generated by the expanding bubble is slowly dissipated by pressure-volume work.[139] Secondly, fig. 7.1 shows that the collapse of the bubble is insufficiently fast to have finished before the rarefaction phase of the applied acoustic field starts, i.e., in the final stages of collapse the applied acoustic pressure is negative. For a larger acoustic pressure amplitude, the bubble can grow to such a large size that it cannot manage to collapse within a single acoustic cycle and only partially collapses. This is then followed by another growth phase and finally ends by the full collapse of the bubble once the acoustic pressure becomes positive again.[134] We do not consider this type of bubble dynamics in the work presented in this chapter.

In the next section we discuss the implementation of a Brownian dynamics simulation of a carbon nanotube near a bubble undergoing transient cavitation. In this simulation, the bubble dynamics is presumed to follow those shown in fig. 7.1. The corresponding fluid flow is obtained by presuming incompressibility of the fluid and spherical symmetry of the bubble. In chapter 6.2 we showed that in this case the local fluid velocity, $v\,(r,t)$ at a distance r from the center of the bubble is given by

$$\vec{v}\,(r,t) = \frac{\dot{R}(t)R^2(t)}{r^2}\hat{e}_r, \tag{7.5}$$

where $\hat{e}_r$ is a radial unit vector and the origin of the coordinate system corresponds to the center of the bubble. In the Brownian dynamics simulation this fluid flow is incorporated as an “external field” that exerts a force proportional to the fluid viscosity on the nanotube. Hence, it is not perturbed by the presence of the nanotube.

7.3 Brownian dynamics of a bead-rod chain

In the Brownian dynamics simulation, the carbon nanotube is modeled as a bead-rod chain of N beads and $N-1$ inextensible rods linking the beads.[134] Stokesian dynamics are presumed in the simulation, meaning that inertial effects can be neglected. We discussed this presumption in detail in chapter 6.3. As a consequence, the total force on each of the $i = 1...N$ beads equals zero,

$$\vec{F}_i^{\text{potential}} + \vec{F}_i^{\text{Brownian}} + \vec{F}_i^{\text{drag}} + \vec{F}_i^{\text{metric}} + \vec{F}_i^{\text{constraint}} = 0, \tag{7.6}$$

where $\vec{F}_i^{\text{potential}}$ are forces caused by the bending of the nanotube,[152–154] $\vec{F}_i^{\text{Brownian}}$ is a random force on the bead caused by thermal fluctuations,[152] $\vec{F}_i^{\text{drag}}$ are viscous drag forces on the bead that are proportional to the relative fluid velocity along the bead,[152,153] $\vec{F}_i^{\text{metric}}$ are pseudo forces that must be included to retain the theoretical equilibrium conformation distribution of the chain[152,154] and finally $\vec{F}_i^{\text{constraint}}$ are the forces on the bead resulting from the tension in the extensible rods connected to the bead.[152]

The potential forces, $\vec{F}_i^{\text{potential}}$, caused by the bending of the nanotube are calculated from the discrete worm-like chain model and are proportional to the bending stiffness of the nanotube which is $L_p k_B T$, where L_p is the persistence length of the nanotube and $k_B T$ is the thermal energy.[154] The initial conformation of the nanotube prior to the explosive growth of the bubble is sampled from the equilibrium conformation distribution of a discrete worm-like chain and the center of mass of the nanotube is placed at a distance d_i from the center of the bubble.[134,153]

The viscous drag forces, $\vec{F}_i^{\text{drag}}$, are, just as in the analytical scission model, presented in chapter 6.3, calculated by application of first-order slender body theory.[146,147] In this approximation the viscous drag forces are proportional to the relative fluid velocity along the nanotube. The proportionality constant is itself proportional to the fluid viscosity and it is anisotropic due to hydrodynamic screening of the fluid flow along the (local) main axis of the nanotube. The component perpendicular to the main axis is twice as large as the component parallel to the main axis. In contrast to the work presented in the previous chapter a correction term that is proportional to the logarithm of the aspect ratio of the nanotube is included in the proportionality constants.[126,146,147,151]

By solving eq. (7.6) for $i = 1..N$ one finds the instantaneous velocity of each of the N beads. Due to the presumed Stokesian dynamics, these velocities are such that the viscous drag force resulting from the motion of each of the beads is such that it is equal but opposite to the sum of all other forces acting on the bead. These forces include but are not restricted to the viscous drag force imposed by the local fluid velocity at the position of the bead generated by the cavitating bubble, as well as a force resulting from the tension in the inextensible rods connecting the subsequent beads such that the length of the nanotube remains constant. Given the instantaneous velocities of all the beads calculated in this manner, the “new” position and conformation of the nanotube can be calculated by integration over a single time step and hence the time-dependent motion of a carbon nanotube near a cavitating bubble can be calculated.

By considering the conformation of the nanotube at each time step as well as the tension in each of the rods, we check if scission of the nanotube occurs at that point in time. In our simulations, scission under tension occurs if the tension in a rod exceeds the breaking strength of the nanotube, while scission due to bending and buckling occurs when the local radius of curvature of the nanotube falls below a critical value.[134, 151] In previous simulations,[134, 151] scission under tension occurred when the fluid strain rate at the center of mass of the nanotube exceeded a critical length-dependent value. This method has two important drawbacks. Firstly, in reality, scission only occurs at this critical strain rate when the nanotube is radially oriented relative to the bubble surface and fully stretched, clearly this is not always true in the simulations due to the bending of the nanotube. Secondly, the exact scission position remains unknown. Both of these issues are resolved when the tension in each of the rods is compared to the breaking strength of the nanotube at each time step to check for scission.

If at any time the tension in any of the rods exceeds the breaking strength of the nanotube, or if the local radius of curvature at any of the beads falls below the critical radius of curvature, the nanotube breaks at precisely that point. The simulation has been adapted to explicitly take this into account. If either of the scission criteria is met, the simulation is interrupted and continued for the two separate nanotube fragments that are formed by scission. That is, if a nanotube of N beads breaks at bead k then the simulation is continued for one bead-rod chain of k beads and one bead-rod chain of $N-k+1$ beads as to assure that the total length the nanotube fragments is conserved. The initial position of these fragments is identical to the position of them just prior to scission. Note that these fragments do not interact in any way in the remainder of the simulation. In the next section we use this simulation method to investigate under which circumstances multiple scissions can occur during a single collapse phase of the bubble and how changes in persistence length, tensile strength and the critical radius of curvature affect the scission mechanics.

7.4 Results

In this section we investigate the scission mechanics of carbon nanotubes by the Brownian dynamics simulation introduced in the previous two sections. While in previous work[134, 151] it was shown that there is a length-dependent competition between scission by bending and by buckling, it was not possible to study the explicit scission and hence, the possibility of multiple scissions in a single nanotube during a single collapse of a bubble. Here, we address two different types of scission scenarios: 1) a long (model) nanotube with a “small” persistence length and a “high” tensile strength, e.g., a single-wall nanotube, for which we expect multiple scissions to occur due to bending and subsequent buckling and 2) a long (model) nanotube with a “large” persistence length and a “low” tensile strength for which we expect multiple scissions to occur under tension.

For the first set of simulations we use parameter values representative of a single-wall carbon nanotube. The tensile strength of the model nanotube is set to $\sigma_T = 37$ GPa,[134, 144, 155] which corresponds to a $F_B = 20$ nN breaking force for a nanotube with 1.2 nm diameter. The persistence length is set equal to $L_p = 30$ μm, which corresponds to the lower boundary of values reported in literature for the persistence length of a single-wall carbon nanotubes.[148, 149] For the critical radius of curvature below which scission occurs we use $\xi_c = 40$ nm, which is the same value as used in previous simulations.[134] In the final section of this chapter, the discussion, we discuss this scission criterion in some detail.

Simulations were performed for a total of 40 nanotubes of a 4 μm length. The center of mass of each of these nanotubes is at a distance of $d_i = 50$ μm from the center of the bubble just prior to its explosive growth. We choose this value for the initial distance because it is sufficiently small to allow for the scission of the nanotube. The initial conformation of each of these nanotubes is randomly sampled from the discrete worm-like chain model. The results show that all of these nanotubes undergo scission at least once, while some nanotubes undergo scission up to six times, where scission always occurs due to buckling and the associated high degree of bending, i.e., the local radius of curvature falls below 40 nm. In fig. 7.2 the conformation of a) a nanotube at the moment at which the first of a total of six scissions occurs, b) the same nanotube at the moment of the fourth scission and c) at the moment of the sixth and final scission is shown.

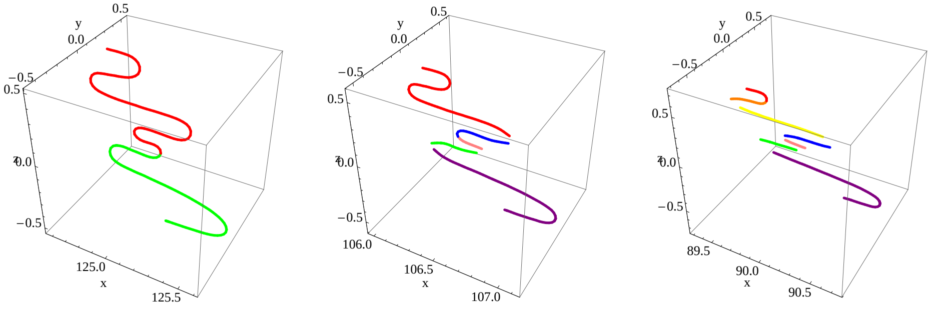

(a) (b) (c)

Figure 7.2: The conformation of a 4 μm long nanotube at three different moments in time. Different fragments are indicated by different colours. The origin of the coordinate system is at the center of the bubble and the unit of length is a micron. a) the conformation of the nanotube at the moment of the first of a total of six scissions, b) at the moment of the fourth scission, and c) at the moment of the sixth and final scission.

In fig. 7.3 the conformations of two identical nanotubes of 4 μm that undergo scission just once by bending and subsequent buckling during the collapse of the bubble are shown. Note that the initial conditions for these two nanotubes are identical to the one of which the scission is shown in fig. 7.2. From figs. 7.2 and 7.3 it is clear that a nanotube can attain significantly varying conformations during the collapse of the bubble even if the simulation settings are identical. These differences are created during the initial stages of collapse. Here the nanotube is aligned tangential to the bubble surface and fully stretched and thermal fluctuations determine where and in how many places this symmetry is broken and hence where the nanotube buckles under the compressive forces exerted on it by the fluid flow.[134, 151]

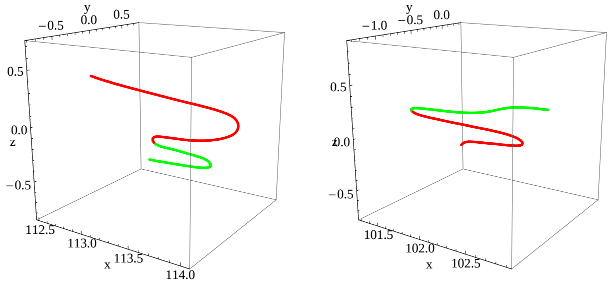

(a) (b)

Figure 7.3: a,b) The conformations of two 4 μm long nanotubes at the moment of the first and only scission it undergoes. Different fragments are indicated by different colours. The origin of the coordinate system is at the center of the bubble and the unit of length is a micron.

Another important finding from this simulation is that nanotubes of a length of 4 μm that start out at a distance of 50 μm from the center of a bubble never break under tension (0 out of 40 did break under tension). Out of the 40 nanotubes simulated, the maximum tension reached is 12 nN, which is below the 20 nN breaking strength of the nanotube. This can be understood using results from the previous chapter, and specifically by eq. (6.18) for the minimum length for which scission under tension can occur. By applying this equation to the simulation conditions, we find that the minimum scission length is 1.6 μm for a fully stretched nanotube. Note that this minimum length is valid only for nanotubes that are very close to the bubble and is larger for nanotubes that start out at a larger distance from the bubble.

From fig. 7.2 it is clear that the buckling and bending of the nanotube leads to segments that are free from significant bending, aligned approximately radially, that are shorter than 1.6 μm. While the conformation of the nanotubes in fig. 7.3 are close to 1.6 μm, the total stress to which they are exposed is simply insufficient to cause their scission. The persistence length of 30 μm is insufficient for any nanotube segment of sufficient length to undergo scission under tension to be formed during the collapse of the bubble. Or put differently, the tensile strength of the nanotube is too large for the segments that are formed during the buckling of the nanotube to undergo scission under tension.

However, scission under tension becomes the dominant scission mechanism when the persistence length of the model nanotubes is increased while their breaking strength is decreased. We have performed simulations for 40 nanotubes of again a length of 4 μm for this scenario by decreasing the breaking strength to 2 nN, by increasing the persistence length up to $L_p = 500$ μm and by decreasing the initial distance between the bubble and the nanotube to 20 μm. The simulations show that these nanotubes always break atleast once under tension and up to a maximum of three times, while scission due to bending and buckling never occurs for these nanotubes. Of course we realise that these values might not be very realistic for single wall nanotubes, however these value might be representative of other types of fibers and they allow us to explore different scenarios by which scission occurs.

In fig. 7.4 the conformation of a nanotube that undergoes scission a total of three times is shown at the moment of each of these three scissions. This figure shows that even though the persistence length is increased from 30 μm (figs. 7.2 and 7.3) up to 500 μm, the nanotube still bends and buckles, in this case in two places. All three of the segments that are aligned more or less radially and which are free from bending undergo scission under tension near the middle of each of these segments.

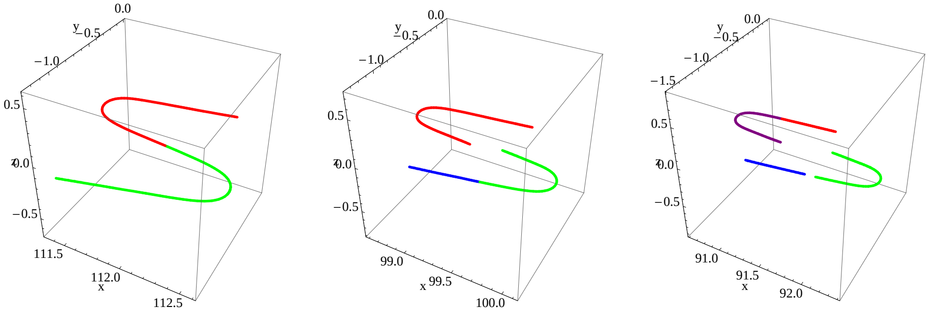

(a) (b) (c)

Figure 7.4: The conformation of a 4 μm long nanotube at three different moments in time. Different fragments are indicated by different colours. The origin of the coordinate system is at the center of the bubble and the unit of length is a micron. a) The conformation of the nanotube at the moment of the first of a total of three scissions, b) at the moment of the second scission, and c) at the moment of the third and final scission.

In fig. 7.5 the conformation at the moment of scission of two nanotubes that undergo scission only once is shown. These nanotubes have buckled and are bent in three places, rather than just two as in fig. 7.4. As a consequence only one of the radially oriented segments which is free of bending is sufficiently long to undergo scission under tension.

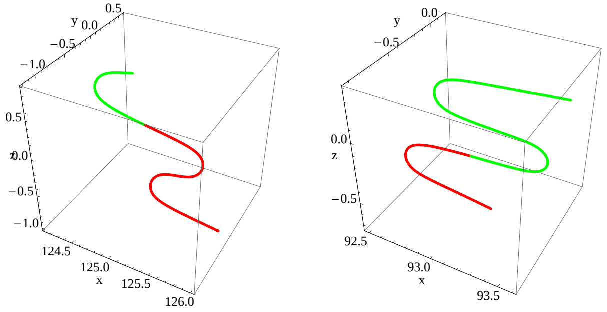

(a) (b)

Figure 7.5: a,b) The conformations of two $4\ \mu\mathrm{m}$ long nanotube at the moment of the first and only scission it undergoes during the collapse of a bubble. Different segments are indicated by different colours. The origin of the coordinate system is at the center of the bubble and the unit of length is a micron.

Clearly, the results shown in figs. 7.4 and 7.5 are opposite to the results as shown in figs. 7.2 and 7.3. In the scenario just discussed the nanotubes have a “large” persistence length and a “low” tensile strength and these nanotubes break under tension before any part of the nanotube undergoes scission due to bending and buckling. Presumably this is the case because for scission due to bending and buckling to occur the segments of the nanotube on either side of the highly bent part of the nanotube must be sufficiently long to be able to enforce a sufficiently high degree of bending for scission to occur. This suggests that there is also a minimum length of the nanotube segments that are free from bending, and which surround a highly bent part of the nanotube, for scission under bending to occur. Presumably, in this case this minimum length for which scission under bending and buckling can occur is larger than the minimum length for which scission under tension can occur. As a consequence, scission under tension occurs before scission due to buckling and bending can occur and the resulting segments of the nanotube surrounding highly bent parts of the nanotube are too short to force the local curvature in these points below the critical radius of curvature for which scission occurs.

We restrict our simulations to these two “types” of nanotube (or more generally, types of fiber), i.e., nanotubes with a “large” persistence length but “low” tensile strength and nanotubes for which the opposite holds true. In the next section we discuss the results that were presented in this section and specifically address how the explicit scission of the nanotubes in the simulation, previously not included in the simulations, affect the conclusions and results that were obtained from these simulations.[134,151]

7.5 Discussion

We have reported on results of Brownian dynamics simulations for the scission of carbon nanotubes near a transiently cavitating bubble. While this simulation was previously developed,[134,151] we extended it by allowing for explicit and multiple scissions within a single nanotube during the collapse of a single bubble. An important presumption in the simulations is that nanotubes undergo scission when the local radius of curvature falls below 40 nm. For thin single wall nanotubes this radius might actually be as small as 15 nm.[134] Moreover, both experiments and simulations suggest that the buckling of a nanotube does not necessarily always lead to its scission.[28,156–158] Experiments even show that multi-wall nanotubes can repeatedly buckle without any permanent deformation being formed.[158] Note that the nanotubes in these experiments are not subjected to the violent fluid flow generated by a collapsing bubble, it is well possible that the combination of buckling and the viscous drag forces exerted by the fluid flow does result in buckling-mediated scission. A possible mechanism for this is the previously proposed “atomic sheet-fracture” scission mechanism for single-wall nanotubes.[133]

The key result from the previous simulations is that long nanotubes break by bending and buckling while shorter nanotubes break under tension after reorientation to a fully stretched and radial alignment.[134,151] Our results show that the reality is slightly more complex and involves multiple competing length scales. Moreover, our results show that long nanotubes will break in multiple places during the collapse of a single bubble, contrasting with all previous models for carbon nanotube scission under sonication in which it is presumed that scission occurs at the most once during the collapse of a single bubble.[126,127,130,133,134]

The results from our simulations suggest that there are three key length scales involved in the scission of carbon nanotubes under sonication. These are: 1) The length of the segments of the nanotube that are free of significant bending and approximately radially oriented in the final stages of the collapse, presumably determined by the persistence length of the nanotube. The ratio of this length scale to the length of the nanotube determines the number of places in which the nanotube bends and buckles. See chapter 6, 2) The minimum length of a radially oriented and relatively straight segment of the nanotube for which it can undergo scission under tension, as determined by the tensile strength relative to the maximum strain rate of the fluid flow to which the nanotube is subjected. 3) The minimum length of the segments surrounding a highly bent part of the nanotube for which the local radius curvature can be forced below the critical radius of curvature for scission to occur. Presumably this length is set by a combination of this critical radius of curvature, the persistence length of the nanotube and the maximum strain rate of the fluid flow to which it is subjected.

These three length scales compete. If the minimum length for scission under tension to occur is larger than the length of the segments remaining free from significant bending then no scission under tension can occur. If the minimum length for scission due to bending and buckling to occur is smaller than the length of the segments that remain free of bending then buckling-mediated scission occurs. This situation is shown in figs. 7.2 and 7.3. Presumably, if the critical radius of curvature for scission due to bending and buckling to occur is decreased, the associated minimum length for buckling-mediated scission increases and if the critical radius of curvature is decreased sufficiently, this length becomes larger than the length of the nanotube segments that are free from bending, and no scission of the nanotube can occur.

This suggests that it is not so much the length of the nanotube itself that dictates the scission mechanism but rather that it is the length of the segments that remain free from significant bending, which given the length of the nanotube is directly proportional to the number of points at which the nanotube bends and buckles, that dictates the scission mechanism. If the length of these segments is larger than the length for scission under tension and for scission due to bending and buckling to occur, then scission by both mechanisms is possible. However, if the minimum length for scission under tension is significantly smaller than the minimum length for scission due to bending and buckling, then the nanotube will break under tension and the resulting fragments will be too short for scission due to bending and buckling to occur. This situation is shown in figs. 7.4 and 7.5.

On the other hand, if the minimum scission length for scission due to bending and buckling to occur is smaller than the minimum length for scission under tension, then it is presumably possible that the nanotube first breaks due to bending and buckling after which the resulting fragments, which are still sufficiently long to allow for scission under tension, undergo scission under tension. Clearly, the competition between the three length scales is complex and allows for a wide variety of scission mechanisms.

An important conclusion from this discussion is that unless both the minimum scission length for scission under tension and the minimum length for buckling-mediated scission are of similar magnitude, one of these scission mechanisms will predominate. For actual single wall carbon nanotubes, this indeed appears to be the case because simulations for a 4 μm long nanotube only show scission due to bending and buckling to occur, see figs. 7.2 and 7.3. This supports the previously proposed distinction of short nanotubes undergoing scission under tension and longer nanotubes undergoing scission due to bending and buckling.[134] Here, it should be noted that the length of relatively short nanotubes that reorient into a fully stretched radially aligned conformation is presumably longer than the length of the segments that remain free from significant bending in longer nanotubes that bend and buckle because their reorientation suppresses buckling. Hence, these nanotubes can be sufficiently long to undergo scission under tension even if longer nanotubes that buckle cannot.

We realise that the previous discussion is speculative and that it would benefit from additional simulations for nanotubes of different lengths. We plan to perform these simulations and in particular aim to use the results to statistically describe the length-dependent probability that nanotubes undergo scission once, twice, even more often or not at all. Given these probabilities the time evolution of the nanotube length distribution can be simulated, which allows for comparison with experiments in which the decrease of the average nanotube length during sonication has been measured.[122, 126, 130, 132] This makes a detailed investigation of the competition between scission under tension and buckling-mediated scission possible. Moreover, it allows for an investigation of the effects of multiple scissions in a long nanotube during its interaction with a single collapsing bubble. In principle, having multiple scissions within a single nanotube should significantly speed up the decrease of the average nanotube length relative to the situation where scission occurs at the most once.

While the number of times a nanotube undergoes scission varies discretely, this should presumably not give rise to discontinuous changes in the scission kinetics, i.e., in the time-dependent decrease of the average length, which experiments have shown to be non-universal.[122, 126, 130, 132] Rather, our results show that the number of times a $4\ \mu$m long nanotube undergoes scission varies and should be described statistically. Presumably, the resulting probability distribution varies continuously with length.

In summary, simulations of the scission of carbon nanotubes under sonication by Brownian dynamics simulations is a powerful tool to investigate the mechanics by which scission occurs. Our results suggest that depending on the properties of the nanotube or the fibre the mechanics can differ significantly and that long nanotubes can undergo scission in multiple places.

We would like to thank Matteo Pasquali for discussions and for making available the code of the Brownian dynamics simulation that was used to obtain the results presented in this chapter.

Part III

General discussion

Chapter 8

Discussion

8.1 Aim of the thesis

The aim of the work presented in this thesis is to uncover the non-universal aspects of the equilibrium and non-equilibrium behaviour of two different soft matter systems that appear when additional degrees of freedom, which are often neglected in models for these systems, are incorporated in the theory at a highly coarse-grained level. The first system is a model two-state protein dispersion in which the proteins can reversibly switch between two different conformations. For this system we have investigated the non-universal conditions under which phase separation occurs in the model dispersion and the manner by which the associated transition from a homogeneous to a heterogeneous phase separated state proceeds. To this end we presented a model two-state protein dispersion in which the proteins can reversibly switch between their native and a high-energy non-native state. The effective volumes of these two states are not necessarily equal. We investigated both the equilibrium and non-equilibrium properties of this model system. Furthermore we have shown that a two-state protein model is an excellent method to interpret the results of infrared spectroscopy measurements on an actual protein dispersion.

In the second system carbon nanotubes are dispersed in a liquid by ultrasound. The applied acoustic field leads to ultrasonic cavitation that allows for the dispersion and exfoliation of carbon nanotubes. For this system we investigated the mechanics by which scission occurs and in particular the aspects of the scission mechanics that give rise to non-universality in the scission kinetics. To this end, we developed an analytical model for the scission of nanotubes under tension, the results of this model suggest that the length-dependent motion of the nanotubes near a cavitating bubble lead to non-universal scission kinetics. Brownian dynamics simulations were performed to investigate the competition between scission under tension and buckling-mediated scission of the nanotubes. The results show that the precise scission mechanism depends on the properties of the nanotube and that sufficiently long nanotubes will undergo scission multiple times during their interaction with a single collapsing bubble.

In the following sections we review and discuss the most important results and conclusions from the work presented in this thesis. In section 8.2 we do so for the work related to the study of the consequences of the coupling of changes in protein conformation to their phase behaviour, while in section 8.4 we do so for the work on the mechanics of carbon nanotube scission under sonication. In sections 8.3 and 8.5 we give an outlook and suggestions for future work on each of the two topics.

8.2 The coupling of conformational in proteins to their phase behaviour

In the first part of this thesis we studied the coupling of changes in the conformation of a protein to the phase behaviour of the protein dispersion. In the following we briefly discuss and list the most important results of the work presented in chapters 2, 3, 4 and 5.

In chapter 2 we presented a two-state method to interpret measurements by attenuated total reflectance Fourier transform infrared (ATR FTIR) spectroscopy on beta-lactoglobulin (BLG). Under the conditions at which the measurements were performed, there is an equilibrium between the monomeric and dimeric state of this protein and the degree of dimerisation increases with increasing concentration due to mass action effects. The most important results and conclusions from the work presented in this chapter are:

- The IR spectra can be interpreted as a linear combination of the spectra of monomeric and dimeric BLG, allowing for determination of the degree of dimerisation at the protein concentration for which the measurement is performed.
- By repeating this procedure for measurements at different protein concentrations the concentration-dependent degree of dimerisation can be determined.
- A dimerisation model can be fitted to this experimentally determined relation between the protein concentration and the degree of dimerisation. Self-crowding effects, which relate to changes in the total free volume caused by the dimerisation of BLG, must be included in the dimerisation model if it is to successfully account for the degree of dimerisation at the highest concentrations for which experiments were performed.
- The dimerisation model which includes self-crowding effects gives a prediction for the effective hard-sphere radius of the protein which includes electrostatic interactions.
- The presented method is more widely applicable and can be used to quantitatively study the concentration-dependent equilibrium of any process in a protein dispersion that involves changes in the secondary structure of the protein.

In chapter 3 we presented a model two-state protein dispersion in which the proteins can reversibly switch between their native and a high-energy non-native state in which the model proteins can engage in an attractive interaction with other proteins that are also in the non-native state. For this model we studied the conditions under which phase separation occurs and based on the local curvature of the free energy landscape we determined the thermodynamic stability of the model dispersion. The most important results from this work are:

- The model shows a demarcation between a regime of weak-coupling and a regime of strong-coupling between changes in the conformation of the protein and the phase behaviour of the protein dispersion. We have argued that this demarcation is reminiscent of the distinction between the modeling of liquid-liquid phase separation in which proteins are presumed to remain in their native state and the modeling of amyloid fibrillation which hinges on changes in the conformation of proteins.

- In the weak-coupling regime the native and the non-native state of the protein are separated by a free energy difference of less than $2\ k_BT$ and changes in the conformation of the proteins are induced by changes in the local protein concentration.
- In the strong-coupling regime the native and non-native conformation of the protein are separated by a free energy difference of more than $2\ k_BT$ and there is a first-order conformational phase transition that underlies phase separation in the protein dispersion. This results in a strong coupling between the protein conformation and the phase behaviour. The kinetics by which phase separation occur become inherently dependent on the conformation of the protein and the underlying first-order conformational phase transition can give rise to nucleation phenomena even if the dispersion is thermodynamically unstable.
- At a fixed protein concentration of $\phi = 1$, the model system reduces to a mean-field Ising model system, which has a critical point at a free energy difference of $2\ k_BT$ between the two conformations and for attractive interactions between the non-native proteins of strength $4\ k_BT$. This critical point coincides with both the critical point of liquid-liquid phase separation for the case where the two conformations are separated by $2\ k_BT$, and the first appearance of the first-order conformational phase transition.
- In the strong-coupling regime there is no longer a real critical point for liquid-liquid phase separation. Instead, the regime in which liquid-liquid phase separation occurs terminates in an Ising-like coexistence of phases with a different average protein conformation at fixed concentration $\phi = 1$.
- The phase behaviour of the model dispersion is non-universal, no law of corresponding states has been found.
- For $\epsilon > 1.65$, the phase behaviour of the model dispersion becomes re-entrant, meaning that a continuous change in temperature leads to the transition from a homogeneous state, to a phase separated state, back to a homogeneous state and finally back to a phase separated state again.
- All of these conclusions hold true for both a Flory-Huggins-based model free energy and a Carnahan-Starling-based model free energy.

In chapter 4 we extended the model that was first presented in chapter 3 to include differences in the effective volume between the two conformations. In this work we presumed that upon transition to the non-native state, the effective volume of the protein increases. The reversible switching between these two conformations allows for the regulation of the free volume in the dispersion. The regulation of the amount of free volume in the dispersion is in direct competition with the tendency of the proteins to switch to their non-native state of non-minimum volume in which they can engage in attractive interactions with other proteins in the same state. The most important results from this work are:

- Self-crowding effects significantly affect the predicted phase behaviour even if the difference in the effective volume between the two conformations is small.
- At high protein concentrations self-crowding effects stabilise a homogeneous phase of proteins in their native conformation.
- At intermediate concentrations a homogeneous phase of proteins in the non-native state is stabilised.
- The equilibrium phase at an intermediate concentration and the equilibrium phase at a high concentration as described in the above are separated by a first-order conformational phase transition. At lower concentrations a second first-order conformational phase transition can occur. This latter transition is also observed in the model dispersion where both conformations are of equal size.
- Both first-order conformational phase transitions are associated with a regime of phase separation. Hence, when the conformations are not of equal size there are two distinct concentration intervals within which phase separation of the protein dispersion occurs. The regime of phase separation at high concentrations is caused by self-crowding effects.
- The phase diagram of the model protein dispersion falls in either of two categories depending on the free energy difference and size difference between the two conformations of the protein. In the first category both regimes of phase separation end in separate critical points. In the latter category this does not hold true and both regimes of phase separation end in a joint non-standard "critical point" at which the two regimes of phase separation can no longer be distinguished and there is a coexistence between two phases of different average protein conformation at an equal protein number density.
- The model system is of theoretical interest because protein concentration is no longer a conserved order parameter.

In chapter 5 the kinetics by which phase separation occur in the model protein dispersion, first introduced in chapter 3, were investigated. To this end, a set of model-C-like kinetic equations and a square-gradient-based free energy functional were presented. We performed a stability analysis on these equations and uncovered three distinct modes by which instabilities in the model dispersion grow. The most important results from this work are:

- The kinetics of phase separation involve changes in both the local protein concentration and conformation in this model. Changes in concentration occur at a time scale proportional to the protein diffusion time, while changes in the protein conformation occur at a time scale proportional to the conformational relaxation time of the protein.

- The kinetics by which non-equilibrium processes occur are a function of both the local geometry of the free energy landscape and the relative magnitudes of these two time scales.
- A linear stability analysis reveals three distinct modes by which instabilities in the dispersion can grow, being, 1) the global relaxation of the protein conformation while the protein concentration remains unchanged, 2) a spinodal mode where differences in both the local protein concentration and conformation are established at a well defined length scale, and 3) the scale-free relaxation of both protein concentration and conformation in a manner in which the local concentration of proteins in the non-native state is conserved. Presumably this last mode is an artifact of our model.
- The dominant mode by which an instability grows depends strongly, and presumably in a non-universal manner, on the initial average conformation of the proteins.
- In both the weak-coupling and strong-coupling regime the relaxation from a homogeneous non-equilibrium state to a homogeneous equilibrium state can involve temporary phase separation in the protein dispersion.
- In the strong-coupling regime the underlying first-order conformational phase transition greatly complicates the kinetics by which phase separation occurs and evaluation of the full non-linear kinetic equations is necessary to obtain a more thorough understanding of this process.

In the next section we give a brief overview of areas where additional research is required and areas where this is possible.

8.3 Outlook (part I)

In this section we give a point-by-point overview of future research that is required to strengthen the work presented in this thesis and give suggestions for areas in which interesting new research can be performed based on the work presented in this thesis. However, before this we give some general remarks on the research on the phase behaviour of protein dispersions.

Theoretical investigations of the phase behaviour of proteins have focused on various properties of the protein. The most important of these are the anisotropic interactions between proteins that result from their chemically heterogeneous surface, which is covered by theoretical work on patchy colloids. A second important property of proteins is that they interact over a length scale that is small relative to their own size, by now it is well established that this leads to meta-stability of liquid-liquid phase separation with respect to crystallization of the proteins. Finally, some work has focused on the “softness” of the proteins and how it influences their crystallization. Importantly, in the theoretical modeling on all of these aspects of the proteins phase behaviour, the proteins are presumed to remain in their native state. In contrast to this is the theoretical work on the aggregation of proteins in their non-native state, for example in amyloid fibrils, in which changes in the conformation of the proteins are explicitly considered. As we have previously argued, there is no reason to exclude the possibility of reversible changes in the conformation of proteins from the modeling of their phase behaviour.

The work presented in this thesis is a first step to theoretically investigate the consequences of the coupling of changes in the conformation of proteins to their phase behaviour. However, we focused on liquid-liquid phase separation only. To obtain an understanding of the effects of conformational changes in a protein on the full phase behaviour exhibited by a protein disperision, our model must be extended to also include a model for a transition to a crystalline phase and a gel state. This will facilitate the comparison with actual experiments, and show which aspects of the liquid-liquid phase separation in the model two-state protein dispersion are hidden behind the transition to a gel state and a crystalline phase.

In a next step, the two-state free energy model could be refined by the introduction of a more realistic protein-protein interaction potential. Presumably this is especially important in the development of a model for crystallisation for which it is already known that the small interaction length of the proteins relative to their size results in the meta stability of liquid-liquid phase separation with respect to crystallization. In a final step, our model in which the conformation of proteins is not conserved can be coupled to a patchy colloid model, allowing for changes in the anisotropic interactions between the proteins due to changes in the conformation of the protein.

The development of these ever more sophisticated models for the phase behaviour of proteins should be accompanied by experimental validation of the predictions made by these models. Of especial importance for the work presented in this thesis is that conformation of proteins is monitored in experiments in which this is not standard practice at the moment, e.g., experiments on liquid-liquid phase separation. The final aim of all of this, is of course to obtain an as complete as possible theoretical framework that describes the phase behaviour of proteins. This framework should be helpful in interpreting the results of experiments on protein phase behaviour and identify and understand problems that occur in the development of practical applications that involve the handling and manipulation of protein dispersions.

Besides a more general outlook on the research of protein phase behaviour, we next give a number of topics and areas that are directly related to the results presented in this thesis for which additional research is required. These are,

- The two-state method by which the concentration-dependent degree of dimerisation was determined from the infrared spectra of beta-lactoglobulin proteins in chapter 2 needs validation by a direct comparison of the predicted dimerisation constant to the dimerisation constant as determined by other, more established, experimental techniques. Due to the extreme sensitivity of the dimerisation constant on the solution conditions, this requires experiments by different experimental methods to be performed on identical protein solutions.

- The theoretical investigation of the model two-state protein dispersion as presented in chapters 3, 4 and 5 would also benefit from a direct comparison with experiments on the phase behaviour of protein dispersions. Such experiments must include a method to experimentally determine and monitor the conformation of the proteins as a function of the solution conditions even and especially for experiments for which such measurements are usually not performed. Furthermore it is important to realise that some of the effects that are predicted by our model are subtle and difficult to observe, for example it is not straightforward to experimentally observe a heterogeneous distribution of proteins in the native and non-native state when the protein concentration is identical in both phases.

- The nature of the "critical point" in the strong-coupling regime is as of yet not fully understood, at this critical point the composition of the coexisting phases is not identical and presumably this affects the critical behaviour at this "critical point". Additional research to understand the properties of this type of "critical point" would be very interesting.

- The Ising-like conformational demixing at a protein concentration $\phi = 1$ as observed in the model dispersion when both conformation are of equal size appears to "develop" into a fluid-fluid coexistence at unequal concentrations $\phi < 1$ for the situation where the effective volumes of the two conformations are not equal. For a more thorough understanding of this process additional research is required.

- In this thesis the coupling of conformational changes to liquid-liquid phase separation was studied. To understand the coupling to the full phase behaviour of a protein dispersion, models must be developed that also include crystalline phases and gel states.

- To understand the kinetics by which phase separation occurs in the model two-state protein dispersion numerical evaluation of the full non-linear kinetic equations is required. The comparision of these results to actual experimental results is again necessary to bridge the gap between theory and the actual behaviour of protein dispersions.

- A particular problem with the model that was presented in chapters 3 and 4 is that it implicitly presumes changes in the local protein concentration and conformation to occur on a similar time scale. While we discussed the situation where conformational changes are fast as compared to changes in the local protein concentration in detail in chapter 3, we have not addressed the situation where changes in the conformation occur at a larger time scale than changes in local protein concentration. Additional work to uncover the consequences of a large discrepancy between these two time scales is both relevant and important.

8.4 The scission and exfoliation of carbon nanotubes under sonication

In the second part of this thesis, we studied the mechanics by which scission of nanotubes under sonication occurs. In the following we briefly list and discuss the most important results of the work presented in chapters 6 and 7.

In chapter 6 we presented an analytical model for the scission of carbon nanotubes during sonication. In the model it was presumed that the nanotubes are fully stretched and aligned radially in the fluid flow generated by a collapsing bubble. In the model we explicitly included the length-dependent motion of the nanotubes and calculated under which conditions scission of the nanotubes occurs. The most important results and conclusions from the work presented in this chapter are:

- The empty cavity approximation is a very good approximation to solutions of the full Rayleigh-Plesset equation, which offers a more realistic mathematical description of ultrasonic cavitation, if the length and time scale associated with the empty cavity approximation are rescaled to match those of the solution obtained for the full Rayleigh-Plesset equation.

- The length-dependent motion of nanotubes is an important factor in determining the scission mechanics and kinetics of the nanotubes. Short nanotubes are dragged along more easily by the fluid flow and are as a consequence exposed to a fluid flow with a higher shear rate than to which longer nanotubes are exposed.

- This leads to a different scaling relation between the tensile strength and the terminal length of the nanotube fragments that can be obtained by sonication than previously thought. The terminal length of the nanotubes that can be reached by sonication scales with the tensile strength to a power $1/1.16$ instead of to a power $1/2$.

- The length-dependent motion of the nanotubes leads to a breakdown of the power-law dependence of the scission rate on the nanotube length for the situation where the nanotube length is close to the terminal length that can be reached by sonication. This should result in non-universal scission kinetics that depend on the initial length distribution of the nanotubes and on the sonication settings.

- The model allows for calculation of the position on the nanotube at which scission will occur. Typically this is near the center of the nanotube. The length of the resulting fragments is approximately equal to half the length the nanotube had prior to undergoing scission.

- By combining the length-dependent scission rate and the prediction for the point on the nanotube at which scission occurs, a full description of the scission process is obtained that fully dictates the kinetics by which scission occurs during sonication.

- It is plausible that exfoliation of nanotubes under sonication occurs by a scission-mediated process.

In chapter 7 we presented the results of Brownian dynamics simulations on the scission of carbon nanotubes under sonication. In the simulations the nanotubes can undergo scission either under tension or by a buckling-mediated process. Furthermore, in the simulations the nanotubes can undergo scission in multiple places during their interaction with a single collapsing bubble. The most important results and conclusions from the work presented in this chapter are:

- The precise mechanics by which scission occurs, being either scission under tension or scission by bending and subsequent buckling, is determined by the interplay of a number of length scales that depend on the tensile strength of the nanotube, the persistence length of the nanotube, the maximum degree of bending the nanotube can withstand without breaking, and finally the sonication settings.
- In general, a fiber with a large persistence length and low tensile strength will undergo scission under tension, while a fiber with a small persistence length and high tensile strength will undergo scission due to bending and subsequent buckling.
- Sufficiently long nanotubes can undergo multiple scissions during their interaction with a single collapsing bubble. This has not been considered in any of the previous model for the scission mechanics and kinetics of carbon nanotubes under sonication. Presumably this affects the scission kinetics.

8.5 Outlook (part II)

Experiments on the kinetics by which scission of nanotubes occur under sonication have revealed that these kinetics are non-universal. There has been some theoretical effort to understand the origin of this non-universality. In this thesis two new mechanisms that can lead to non-universality were uncovered. These are, the length-dependent motion of nanotubes of a length close to their terminal length, which leads to a non-power law scission rate with corresponding non-universal scission mechanics. Secondly, we have shown that depending on the length of the nanotube and the properties of the nanotube, a nanotube can undergo more than a single scission during the interaction with a single collapsing bubble. Presumably the scission kinetics depend on the number of scissions the nanotubes undergo per interaction with a collapsing bubble, which suggests that this could give rise to non-universal aspects.

Furthermore, in work by Pagani et al. it was suggested that scission under tension and buckling-mediated scission gives rise to different scission rates. Changes in the dominant scission mode then lead to non-universal scission kinetics. Moreover, in work that is currently in progress, we have seen that even a simple power law scission rate, which has previously been presumed to result in universal scission kinetics, does in reality not result in universal scission kinetics. In summary, there is currently a multitude of possible explanations for the observed non-universal scission kinetics and a careful analysis of the kinetics corresponding to each of these explanations is required to understand which of these explanations modes are important and dominant in determining the non-universal scission kinetics as observed by experiment.

At the same time, research on the sonication of carbon nanotubes should focus on the actual practical problem at hand. That is, how does sonication lead to the exfoliation of nanotubes, and how can the highest degree of exfoliation be obtained at a minimum degree of scission? If exfoliation of nanotubes indeed occurs by a scission-mediated process as proposed in chapter 7, is it possible to have sonication settings that do allow for scission-mediated exfoliation while the sonication is sufficiently mild to prevent further scission of the resulting nanotube fragments? A second practically relevant question is whether sonication can be used to manipulate the length-distribution of exfoliated nanotubes in a controlled manner. In order to answer both of these questions there are three areas in which more research is required, these are, 1) the bubble dynamics, 2) the scission kinetics and 3) the exfoliation mechanics. We discuss each of these three points in the following,

- Can a mapping of the time and length scales associated with the solution of the full Rayleigh-Plesset equation for different solution conditions be made? If this is the case, the rescaled empty cavity approximation can be applied without having to solve the full Rayleigh-Plesset equation for each set of sonication settings. This would greatly increase the usability of the rescaled empty cavity approximation.

- What are the consequences of more complicated bubble dynamics for the mechanics of nanotube scission? For example, what happens if two bubbles are sufficiently nearby to both affect a single nanotube or possibly even each other? What are the consequences of an asymmetrical bubble collapse?

- What is the spatial distribution of transiently cavitating bubbles in an actual sonication device? Does the shape of this distribution affect the scission kinetics?

- Does a very high degree of bending of a nanotube under sonication lead to the scission of the nanotube? If yes, what is the precise mechanism by which scission occurs at the atomic length scale?

- What are the precise scission kinetics corresponding to the different models that have been proposed to explain the non-universality as observed in experiments? Are there models that fail to reproduce the experimentally observed scission kinetics?

- Is there a terminal scission length? While all theories for the scission of nanotubes indicate that a terminal length should exist, it has not been observed experimentally.
- Is the proposed mechanism of scission-mediated exfoliation realistic? This question can be answered both by development of an analytical model similar to the one presented in chapter 6, as well as by the Brownian dynamics simulations as introduced in chapter 7 if nanotube-nanotube interactions are included in these simulations.

Bibliography

[1] L.D. Landau and E.M. Lifshitz. *Statistical Physics. Part 1: Course of Theoretical Physics*. Butterworth-Heinemann, 1980.

[2] Daderot. Photo of the grave of Ludwig Boltzmann, retrieved March 2015. `http://commons.wikimedia.org/wiki/File:Zentralfriedhof_Vienna_-_Boltzmann.JPG`.

[3] P-G. de Gennes. *Angew. Chem. Int. Ed. Engl.*, 31:842, 1992.

[4] R.A.L. Jones. *Soft Condensed Matter*. Oxford University Press, 2002.

[5] F. Chiti and C.M. Dobson. *Annu. Rev. Biochem.*, 75:333, 2006.

[6] R. Mezzenga, P. Schurtenberger, A. Burbidge, and M. Michel. *Nat. Mater.*, 4:729, 2005.

[7] J. Ubbink, A. Burbidge, and R. Mezzenga. *Soft Matter*, 4:1569, 2008.

[8] C. Koning, N. Grossiord, and M.C. Hermant. *Polymer Carbon Nanotube Composites: The Polymer Latex Concept*. Pan Stanford Publishing, 2012.

[9] Z. Wu, Z. Chen, X. Du, J.M. Logan, J. Sippel, M. Nikolou, K. Kamaras, J.R. Reynolds, D.B. Tanner, A.F. Hebard, and A.G. Rinzler. *Science*, page 1273, 2004.

[10] A.V. Kyrylyuk, M.C. Hermant, T. Schilling, B. Klumperman, C. Koning, and P. van der Schoot. *Nat. Nano.*, 6:364, 2011.

[11] R. Phillips, J. Kondev, and J. Theriot. *Physical Biology of the Cell*. Garland Science, 2008.

[12] O. Ptitsyn A.V. Finkelstein. *Protein Physics: A Course of Lectures*. Academic Press, 2002.

[13] A.J. Engler, S. Sen, H.L. Sweeney, and D.E. Discher. *Cell*, 126:677, 2006.

[14] H.F. Lodish, A. Berk, S.L. Zipursky, P. Matsudaira, D. Baltimore, J. Darnell, et al. *Molecular cell biology*, volume 4. WH Freeman New York, 2000.

[15] Mariana Ruiz Villarreal. Main protein structures levels, retrieved March 2015. `http://commons.wikimedia.org/wiki/File:Main_protein_structure_levels_en.svg`.

[16] J.E. Gillam and C.E. MacPhee. *J. Phys. Condens. Mat.*, 25:373101, 2013.

[17] S.B. Zimmerman and A.P. Minton. . *Annu. Rev. Biophys. Biomol. Struct.*, 22:27, 1993.

[18] R.J. Ellis. *Trends Biochem. Sci*, 26:597, 2001.

[19] Y. Phillip and G. Schreiber. *FEBS Lett.*, 587:1046, 2013.

[20] A.C. Dumetz, A.M. Chockla, E.W. Kaler, and A.M. Lenhoff. *Biophys. J.*, 94:570, 2008.

[21] M.H.J. Hagen and D. Frenkel. *J. Chem. Phys.*, 101, 1994.

[22] G. Foffi, G. McCullagh, A. Lawlor, E. Zaccarelli, K. Dawson, F. Sciortino, P. Tartaglia, D. Pini, and G. Stell. *Phys. Rev. E*, 65:031407, 2002.

[23] P.G. Vekilov. *J. Phys. Condens. Mat.*, 24:193101, 2012.

[24] M.R.H. Krebs, G.L. Devlin, and A.M. Donald. *Biophys. J.*, 92:1336, 2007.

[25] E. Bianchi, R. Blaak, and C.N. Likos. *Phys. Chem. Chem. Phys.*, 13:6397, 2011.

[26] T. M. Rogers, K. R. Elder, and Rashmi C. Desai. *Phys. Rev. B*, 37:9638, Jun 1988.

[27] M.S. Dresselhaus, G. Dresselhaus, and P. Avouris. *Carbon Nanotubes: Synthesis, Structure, Properties and Applications*. Springer, 2001.

[28] P.J.F. Harris. *Carbon Nanotube Science: Synthesis, Properties and Applications*. Cambridge University Press, 2009.

[29] X. Wang, Q. Li, J. Xie, Z. Jin, J. Wang, Y. Li, K. Jiang, and S. Fan. *Nano Lett.*, 9:3137, 2009.

[30] R.E. Smalley. *Angew. Chem. Int. Ed. Engl.*, 36:1594, 1997.

[31] S. Iijima et al. *Nature*, 354:56, 1991.

[32] Andre K Geim. *Angew. Chem. Int. Ed. Engl.*, 50:6966, 2011.

[33] S.J. Tans, A.R.M. Verschueren, and C. Dekker. *Nature*, 393:49, 1998.

[34] M.-F Yu, O. Lourie, M.J. Dyer, K. Moloni, T.F. Kelly, and R.S. Ruoff. *Science*, 287:637, 2000.

[35] N. Behabtu, C.C. Young, D.E. Tsentalovich, O. Kleinerman, X. Wang, A.W.K. Ma, E.A. Bengio, R.F. ter Waarbeek, J.J. de Jong, R.E. Hoogerwerf, S.B. Fairchild, J.B. Ferguson, B. Maruyama, J. Kono, Y. Talmon, Y. Cohen, M.J. Otto, and M. Pasquali. *Science*, (6116):182, 2013.

[36] J.N. Coleman, U. Khan, W.J. Blau, and Y.K. Gunko. *Carbon*, 44:1624, 2006.

[37] V.A. Davis, L.M. Ericson, A.N.G. Parra-Vasquez, H. Fan, Y. Wang, V. Prieto, J.A. Longoria, S. Ramesh, R.K. Saini, C. Kittrell, W.E. Billups, W.W. Adams, R.H. Hauge, R.E. Smalley, and M. Pasquali. *Macromolecules*, 37:154, 2004.

[38] Y.Y. Huang and E.M. Terentjev. *Polymers*, 4:275, 2012.

[39] M.F. Islam, E. Rojas, D.M. Bergey, A.T. Johnson, and A.G. Yodh. *Nano Lett.*, 3:269, 2003.

[40] T.G. Leighton. *The Acoustic Bubble*. Academic Press, 1994.

[41] M. Ashokkumar, J. Lee, S. Kentish, and F. Grieser. *Ultrason. Sonochem.*, 14:470, 2007.

[42] L.A. Crum. *Ultrasonics*, 22:215, 1984.

[43] C.M. Bryant and D.J. McClements. *Trends Food Sci. Tech.*, 9:143, 1998.

[44] D. Zhu, S. Damodaran, and J.A. Lucey. *J. Agr. Food Chem.*, 56:7113, 2008.

[45] S.G. Hambling, A.S. McAlpine, and L. Sawyer. *Advanced Dairy Chemistry: 1. Proteins*. Elsevier Applied Science, 1992.

[46] G. Kontopidis, C. Holt, and L. Sawyer. *J. of Dairy Sci.*, 87:785, 2004.

[47] E.W. Blanch, L. Hecht, and L.D. Barron. *Protein Sci.*, 8:1362, 1999.

[48] C. Bhattacharjee and K.P. Das. *Eur. J. Biochem.*, 267:3957, 2000.

[49] C. Bhattacharjee, S. Saha, A. Biswas, M. Kundu, L. Ghosh, and K. P. Das. *Protein J.*, 24:27, 2005.

[50] J.J. Adams, B.F. Anderson, G.E. Norris, L.K. Creamer, and G.B. Jameson. *J. Struct. Biol.*, 154:246, 2006.

[51] D. Mercadante, L.D. Melton, G.E. Norris, T.S. Loo, M.A. Williams, R.C. Dobson, and G.B. Jameson. *Biophys. J.*, 103:303, 2012.

[52] M. Gottschalk, H. Nilsson, H. Roos, and B. Halle. *Protein Sci.*, 12:2404, 2003.

[53] M. Verheul, J.S. Pedersen, S.P.F.M. Roefs, and K.G. de Kruif. *Biopolymers*, 49:11, 1999.

[54] J.C. Ioannou, A.M. Donald, and R.H. Tromp. *Food Hydrocolloid.*, 46:216, 2015.

[55] J.L. Koenig and D.L. Tabb. Infrared spectra of globular proteins in aqueous solution. In *Analytical Applications of FT-IR to Molecular and Biological Systems*, volume 57 of *NATO Advanced Study Institutes Series*, pages 241–255. Springer Netherlands, 1980.

[56] A. Barth. 1767:1073, 2007.

[57] Lars Onsager. *Ann. NY Acad. Sci.*, 51:627, 1949.

[58] H. Fischer, I. Polikarpov, and A.F. Craievich. *Protein Sci.*, 13:2825, 2004.

[59] J. Xie and H. Huang. *Colloid Surf., B*, 85:97, 2011.

[60] A. Barth and C. Zscherp. *Q. Rev. Biophys.*, 35:369, 2002.

[61] K. Sakurai, M. Oobatake, and Y. Goto. *Protein Sci.*, 10:2325, 2001.

[62] D.F. Evans and H. Wennerstrom. *The Colloidal Domain: Where Physics, Chemistry and Biology Meet*. John Wiley and Sons Ltd, 1999.

[63] A. Syrbe, W.J. Bauer, and H. Klostermeyer. *Int. Dairy J.*, 8:179, 1998.

[64] E. van der Linden and P. Venema. *Curr. Opin. Colloid Interface Sci.*, 12:158, 2007.

[65] A.M. Donald. *Soft Matter*, 4:1147, 2008.

[66] R. Mezzenga and P. Fischer. *Rep. Prog. Phys.*, 76:046601, 2013.

[67] E.Y. Chi, S. Krishnan, T.W. Randolph, and J.F. Carpenter. *Pharmaceut. Res.*, 20:1325, 2003.

[68] A. Saluja and D.S. Kalonia. *Int. J. Pharm.*, 358:1, 2008.

[69] J.C. Kendrew, H.M. Dintzis G. Bodo, R.G. Parrish, and H. Wyckoff. *Nature*, 181:662, 1958.

[70] S. Zhang. *Nat. Biotechnol.*, 21:1171, October 2003.

[71] R.P. Sear. *J. Chem. Phys.*, 111:4800, 1999.

[72] A. Lomakin, N. Asherie, and G.B. Benedek. *Proc. Natl. Acad. Sci. USA*, 96:9465, 1999.

[73] N. Kern and D. Frenkel. *J. Chem. Phys.*, 118:9882, 2003.

[74] D.E. Kuehner, H.W. Blanch, and J.M. Prausnitz. *Fluid Phase Equilib.*, 116:140, 1996.

[75] M.L. Broide, T.M. Tominc, and M.D. Saxowsky. *Phys. Rev. E*, 53:6325, 1996.

[76] M. Muschol and F. Rosenberger. *J. Chem. Phys.*, 107:1953, 1997.

[77] P. Prinsen and T. Odijk. *J. Chem. Phys.*, 121:6525, 2004.

[78] V.G. Taratuta, A. Holschbach, G.M. Thurston, D. Blankschtein, and G.B. Benedek. *J. Chem. Phys.*, 94:2140, 1990.

[79] V.M.O. Batista and M.A. Miller. *Phys. Rev. Lett.*, 105:088305, 2010.

[80] C.M. Dobson. *Nature*, 426:884, 2003.

[81] T.R. Jahn and S.E. Radford. *Arch. Biochem. Biophys.*, 469:100, 2008.

[82] S. Auer and D. Kashchiev. *Phys. Rev. Lett.*, 104:168105, 2010.

[83] A. Aggeli, M. Bell, L.M. Carrick, C.W.G. Fishwick, R. Harding, P.J. Mawer, S.E. Radford, A.E. Strong, and N. Boden. *J. Am. Chem. Soc.*, 125:9619, 2003.

[84] G. Karlstroem. *J. Phys. Chem.*, 89:4962, 1985.

[85] R. Jaenicke. *J. Biotechnol.*, 79:193, 2000.

[86] K.A. et al. Henzler-Wildman. *Nature*, 450:838, 2007.

[87] L. Hong, D.C. Glass, J.D. Nickels, S. Perticaroli, Z. Yi, M. Tyagi, H. O'Neill, Q. Zhang, A.P. Sokolov, and J.C. Smith. *Phys. Rev. Lett.*, 110:028104, 2013.

[88] L. Day, J. Zhai, M. Xu, N.C. Jones, S.V. Hoffmann, and T.J. Wooster. *Food Hydrocolloid.*, 34:78, 2014.

[89] P.J. Flory. *J. Chem. Phys.*, 10:51, 1942.

[90] M.L. Huggins. *J. Chem. Phys.*, 46:151, 1942.

[91] N.F. Carnahan and K.E. Starling. *J. Chem. Phys.*, 51:635, 1969.

[92] P. Hohenberg and B. Halperin. *Rev. Mod. Phys.*, 49:435, 1977.

[93] R. Ludwig. *Angew. Chem. Int. Edit.*, 40:1808, 2001.

[94] A. Daanoun, C.F. Tejero, and M. Baus. *Phys. Rev. E*, 50:2913, 1994.

[95] D.L Caspar. *Biophys. J.*, 32:103, 1980.

[96] P.G. Stockley, R. Twarock, S.E. Bakker, A.M. Barker, A. Borodavka, E. Dykeman, R.J. Ford, A.R. Pearson, S.E.V. Phillips, N.A. Ranson, et al. *J. Biol. Phys.*, 39:277, 2013.

[97] Jamoliddin R., S. Naderi, and P. van der Schoot. *Soft Matter*, 10:5362, 2014.

[98] J. Guo, N. Harn, A. Robbins, R. Dougherty, and C.R. Middaugh. . *Biochemistry*, 45:8686, 2006.

[99] A.B. Fulton. *Cell*, 30:345, 1982.

[100] S.B. Zimmerman and S.O. Trach. *J. Mol. Biol.*, 222:599, 1991.

[101] B. van den Berg, R.J. Ellis, and C.M. Dobson. *EMBO J.*, 18:6927, 1999.

[102] R.J. Ellis and A.P. Minton. . *Biol. Chem.*, 387:485, 2006.

[103] H.X. Zhou, G. Rivas, and A.P. Minton. . *Annu. Rev. Biophys.*, 37:375, 2008.

[104] A.H. Elcock. *Curr. Opin. Chem. Biol.*, 20:196, 2010.

[105] Y.vQu and D.W. Bolen. *Biophys. Chem.*, 101-102:155, 2002.

[106] A.P. Minton. . *Biophys. J.*, 88:971, 2005.

[107] J. Aden and P. Wittung-Stafshede. *Biochemistry*, 53:2271, 2014.

[108] R.J. Ellis. *Trends Biochem. Sci.*, 26:597, 2001.

[109] J. Herzfeld. *J. Mol. Recog.*, 17:376, 2004.

[110] R.P Sear. *Faraday discuss.*, 139:21, 2008.

[111] H.N.W. Lekkerkerker and R. Tuinier. *Colloids and the depletion interaction*, volume 833. Springer, 2011.

[112] T. Boublik. *J. Chem. Phys.*, 53:471, 1970.

[113] G.A. Mansoori, N.F. Carnahan, K.E. Starling, and T.W. Leland. *J. Chem. Phys.*, 54:1523, 1971.

[114] Jean-Pierre Hansen and Ian R McDonald. *Theory of simple liquids*. Elsevier, 1990.

[115] J.W. Cahn and J.E. Hilliard. *J. Chem. Phys.*, 28:258, 1958.

[116] R. Evans. Marcel Dekker: New York, 1992.

[117] C.B. Anfinsen et al. *Science*, 181:223, 1973.

[118] R. Bandyopadhyaya, E. Nativ-Roth, O. Regev, and R. Yerushalmi-Rozen. *Nano Lett.*, 2:25, 2002.

[119] M.S. Strano, V.C. Moore, M.K. Miller, M.J. Allen, E.H. Haroz, C. Kittrell, R.H. Hauge, and R.E. Smalley. *J. Nanosci. Nanotechnol.*, 3:81, 2003.

[120] N. Grossiord, O. Regev, J. Loos, J. Meuldijk, and C. Koning. *Anal. Chem.*, 77:5135, 2005.

[121] J. Yu, N. Grossiord, C. Koning, and J. Loos. *Carbon*, 45:618, 2007.

[122] T. Liu, S. Luo, Z. Xiao, C. Zhang, and B. Wang. *J. Phys. Chem. C*, 112:19193, 2008.

[123] T. Liu, Z. Xiao, and B. Wang. *Carbon*, 47:3529, 2009.

[124] R.H.J. Otten and P. van der Schoot. *J. Chem. Phys.*, 134:094902, 2011.

[125] D.A. Heller, R.M. Mayrhofer, S. Baik, Y.V. Grinkova, M.L. Usrey, and M.S. Strano. *J. Am. Chem. Soc.*, 126:14567, 2004.

[126] F. Hennrich, R. Krupke, K. Arnold, J. Rojas Stutz, S. Lebedkin, T. Koch, T. Schimmel, and M. Kappes. *J. Phys. Chem. B*, 111:1932, 2007.

[127] S.V. Ahir, Y.Y. Huang, and E.M. Terentjev. *Polymer*, 49:3841, 2008.

[128] H.J. Park, M. Park, J.Y. Chang, and H. Lee. *Nanotechnology*, 19:335702, 2008.

[129] Y.Y. Huang, T.P.J. Knowles, and E.M. Terentjev. *Adv. Mater.*, 21:3945, 2009.

[130] A. Lucas, C. Zakri, M. Maugey, M. Pasquali, P. van der Schoot, and P. Poulin. *J. Phys. Chem. C*, 113:20599, 2009.

[131] Q. Cheng, S. Debnath, E. Gregan, and H.J. Byrne. *J. Phys. Chem. C*, 114:8821, 2010.

[132] A.J. Blanch, C.E. Lenehan, and J.S. Quinton. *Carbon*, 49:5213, 2011.

[133] H.B. Chew, M.W. Moon, K.R. Lee, and K.S. Kim. *Proc. R. Soc. A*, 467:1270, 2011.

[134] G. Pagani, M.J. Green, P. Poulin, and M. Pasquali. *Proc. Nat. Acad. of Sci. USA*, 109:11599, 2012.

[135] E.A. Neppiras. *Ultrasonics*, 22:25, 1984.

[136] A. Prosperetti. *Ultrasonics*, 22:69, 1984.

[137] A. Prosperetti. *Ultrasonics*, 22:115, 1984.

[138] R.E. Apfel. *Ultrasonics*, 22:167, 1984.

[139] R.E. Apfel. *J. Acoust. Soc. Am.*, 69:1624, 1981.

[140] M.W.A. Kuijpers, P.D. Iedema, M.F. Kemmere, and J.T.F. Keurentjes. *Polymer*, 45:6461, 2004.

[141] A. Akyuz, H. Catalgil-Giz, and A.T. Giz. *Macromol. Chem. Phys.*, 209:801, 2008.

[142] H.I. Elsner and E.B. Lindblad. *DNA*, 8:697, 1989.

[143] G. Guerin, H. Wang, I. Manners, and M.A. Winnik. *J. Am. Chem. Soc.*, 130:14763, 2008.

[144] M-F Yu, B.S. Files, S. Arepalli, and R.S. Ruoff. *Phys. Rev. Lett.*, 84:5552, 2000.

[145] J.W. Rayleigh. *Philos. Mag.*, 34:94, 1917.

[146] J.B. Keller and S.I. Rubinow. *J. Fluid Mech.*, 75:705, 5 1976.

[147] J.F.T. Pittman and N. Kasiri. *Int. J. Multiphase Flow*, 18:1077, 1992.

[148] R. Duggal and M. Pasquali. *Phys. Rev. Lett.*, 96:246104, 2006.

[149] N. Fakhri, D.A. Tsyboulski, L. Cognet, R.B. Weisman, and M. Pasquali. *Proc. Natl. Acad. Sci. USA*, 106:14219, 2009.

[150] A.E. Cohen and L. Mahadevan. . *Proc. Natl. Acad. Sci. U.S.A.*, 100:12141, 2003.

[151] G. Pagani. Modeling the dynamics of carbon nanotubes in sonicated fluids. Master's thesis, University of Bologna, 2008.

[152] P Grassia and E.J. Hinch. *J. Fluid Mech.*, 308:255, 1996.

[153] A. Montesi, D.C. Morse, and M. Pasquali. . *J. Chem. Phys.*, 122:84903, 2005.

[154] M. Pasquali and D.C. Morse. *J. Chem. Phys.*, 116:1834, 2002.

[155] N. Behabtu, M.J. Green, and M. Pasquali. *Nano Today*, 3:24, 2008.

[156] B.I. Yakobson, C.J. Brabec, and J. Berhnolc. . *Phys. Rev. Lett.*, 76:2511, 1996.

[157] S. Iijima, C. Brabec, A. Maiti, and J. Bernholc. *J. Chem. Phys.*, 104:2089, 1996.

[158] M.R. Falvo, G.J. Clary, R.M. Taylor, V. Chi, F.P. Brooks, S. Washburn, and R. Superfine. *Nature*, 389:582, 1997.

Summary

Non universality and kinetics in soft matter systems: phase separation of proteins and sonication of carbon nanotubes

Soft matter systems are often modelled at a highly coarse-grained level. For example, globular proteins can be modelled as attractive hard-sphere particles and carbon nanotubes as rigid rod-like particles. In both instances, aside from the geometric properties, the underlying atomic structure is glossed over in the highly coarse-grained description. The corresponding macroscopic properties of such model systems are often highly universal. In this thesis, it is shown that the inclusion of additional degrees of freedom beyond the standard translational and rotational degrees of freedom can lead to non universality in the equilibrium and non-equilibrium behaviour of the model systems, even if these additional degrees of freedom are incorporated at a highly coarse-grained level.

In the first part of this thesis, the liquid-liquid phase separation of a type of model globular proteins that can reversibly interconvert between a native and a non-native conformation is studied. The effective volume, the conformational free energy, and the interactions between the model proteins are presumed to change upon transition to the non-native state. The conditions under which the model two-state protein dispersion phase separates is highly non-universal, exhibits re-entrance and strongly depends on the difference in the effective volumes of the two conformations. Depending on the solution conditions and properties of the model proteins, there is either a weak or strong coupling of the phase behaviour to the conformation of the proteins. The strong coupling results from a first-order conformational phase transition that underlies the liquid- liquid phase separation transition. When the two conformations are not of equal size, the resulting self-crowding effects can give rise to a second first-order conformational phase transition, with an associated second regime of liquid-liquid phase separation.

The model dispersion initially relaxes from non-equilibrium states by any of three different modes. In the first mode, fluctuations in protein concentration and conformation spontaneously grow at a well-defined length and time scale. In the second mode, global relaxation of the conformation of the proteins occurs while the local protein concentration remains. The third mode involves the scale- free relaxation of both protein conformation and concentration in a manner that conserves the lo-

cal concentration of proteins in the non-native state. The conditions for which the model dispersion relaxes towards equilibrium by any of these three modes depend in a non-universal manner on protein concentration, conformation and the solution conditions.

These results suggest that proteins cannot be modelled as simple colloidal particles with no internal structure. Proteins do have an internal structure and the predictions by our model indicate that the coupling of changes in the conformation of the proteins to their liquid-liquid phase separation profoundly affect the phase behaviour, especially when the difference between the native and non-native state is significant.

Finally, it is shown that changes in the conformation of proteins resulting from a reversible reaction can be measured and can be used to quantify the equilibrium constant of this reaction. Specifically, it is shown that the dimerisation constant of beta-lactoglobulin can be determined by the interpretation of a number of IR spectra measured at a variety of protein concentrations in terms of a two-state model.

In the second part of this thesis, the scission of carbon nanotubes under sonication is studied. In particular, the efforts focus on explaining the non- universal scission kinetics as observed in experiments. While it is well established that scission of the nanotubes occurs during the transient collapse of small bubbles, the precise scission mechanism remains debated and a full understanding of the non-universal aspects of it remains to be obtained.

Previously, it has been shown that nanotubes near a collapsing bubble are subjected to high stresses that can lead to their scission. This model is extended by taking the motion of nanotubes during the collapse of the bubble into account. The motion of the nanotubes depends on their length; short nanotubes are “fast” while long nanotubes are “slow” relative to the receding surface of the collapsing bubble. Because of this, short nanotubes are transported to areas closer to the centre of the bubble where they are subjected to fluid flows with a higher shear rate than longer nanotubes. This length- dependence of the maximum shear rate to which nanotubes are subjected during sonication leads to non-universal scission kinetics.

To account for the bending and possible buckling-mediated scission of the carbon nanotubes, Brownian dynamics simulations are performed. While the simulation was previously developed, it was extended to allow for multiple scissions of the nanotubes during its interaction with a single collapsing bubble. The results of the simulations suggest that, depending on the properties of the nanotube, scission either occurs under tension or by bending and subsequent buckling. Furthermore, the simulations show that long nanotubes undergo multiple scissions during their interaction with a single collapsing bubble. The occurrence of multiple scissions in long nanotubes should strongly affect the scission kinetics.

In summary, it is shown that differences in the length of the nanotube give rise to non-universal scission kinetics, both because the maximum strain rate of the fluid flow to which the nanotubes are subjected depends on their length and also because sufficiently long nanotubes will undergo multiple scissions during their interactions with a single collapsing bubble.

List of publications

1. J. Stegen, *Mechanics of carbon nanotube scission under sonication*, J. Chem. Phys. **140**, 244908 (2014).

2. J. Stegen and P. van der Schoot, *Implications of protein polymorphism on protein phase behaviour*, Soft Matter **11**, 2036 (2015).

3. J. Stegen, J.C. Ioannou, R.H. Tromp, A.M. Donald and P. van der Schoot, *Mass-action driven conformational switching of proteins: investigation of beta-lactoglobulin dimerisation by infrared spectroscopy*, submitted.

4. J. Stegen and P. van der Schoot, *Self-crowding induced phase separation in protein dispersions*, submitted.

Dankwoord

Dit proefschrift is het resultaat van het onderzoek dat ik de afgelopen vier jaar heb gedaan. In die vier jaar, hebben een heel aantal van jullie een waardevolle en in sommige gevallen zelfs cruciale bijdrage aan de totstandkoming van dit proefschrift geleverd. Om jullie rol hierin niet onderbelicht te laten wijd ik de volgende paar pagina's graag aan een kort dankwoord.

In de eerste plaats wil ik Paul van der Schoot, mijn tweede promotor en dagelijks begeleider, bedanken. Paul, je enthousiasme voor het theoretisch onderzoek in de zachte materie lijkt haast onbegrensd en dat maakt het aanstekelijk! Met je grondige kennis van het vakgebied heb je altijd richting kunnen geven aan mijn onderzoek en tal van mogelijk interessante richtingen belicht. Ik ben je enorm dankbaar voor het geduld waarmee je mij het schrijven van wetenschappelijke artikelen hebt bijgebracht. Hiervan, evenals van al het ander dat je mij hebt bijgebracht, zal ik in de toekomst dankbaar gebruik maken.

Het houden van het overzicht over de verschillende projecten tijdens mijn promotie was niet altijd even eenvoudig. Daarom wil ik Herman Clercx, mijn eerste promotor, graag bedanken voor zijn hulp bij het managen en plannen van mijn promotietraject.

Matteo, I would like to thank you for giving me the opportunity to visit your group at Rice University, Houston. I thoroughly enjoyed the three months I spent in your group and found it very inspiring to work right alongside experimentalists who were sonicating carbon nanotube while I worked on a model to better understand this process.

John, Hans and Athene, over the past four years we have collaborated on a study of the behaviour of dense protein dispersions. The discussions we have had on this topic have been instrumental in connecting my theoretical work to the practical reality of experiments and industrial applications. I am glad that our collaboration has resulted in a very nice article on the dimerisation of beta-lactoglobulin.

I have had the pleasure to have worked with colleagues at Eindhoven University of Technology, Utrecht University and Rice University. Many of you have contributed in one way or another to this thesis! In particular I would like to thank Helmi, you have been a great help in organising all the paper work involved in a PhD project.

Joost, Stijn, Franz and all the other people with whom I have had the pleasure to go climbing over the past four years, thank you! All the evenings of climbing, and especially the days we have spent climbing outside have been very enjoyable and a great way to recharge for another day or week of work.

Sjors, Wouter, Nick, Tim, Erik, Adrie, Frank en Sander, het is ondertussen al bijna 12 jaar geleden dat wij aan onze studie natuurkunde zijn begonnen. Met dit proefschrift rond ik een even lange periode aan de TU/e af. De avonden waarop we elkaar met regelmaat zien zijn altijd als vanouds gezellig en ik hoop dat er nog vele van deze avonden mogen volgen!

Pap, mam, jullie wil ik in de eerste plaats bedanken voor jullie oprechte interesse in mijn werk, maar daarnaast ook voor jullie betrokkenheid en steun bij mijn promotie. Carcia en Nick, ook jullie wil ik voor jullie interesse bedanken, evenals voor de pittige sportieve ondernemingen die wij in de afgelopen vier jaar samen zijn aangegaan! Siri, jou ook wil ook bedanken, ook jij hebt op je eigen manier aan de totstandkoming van dit proefschrift bijgedragen.

Bastiaan, jou wil ik bedanken voor de vele weekenden in Maastricht en onze vakanties in de alpen. Onze rondjes door het heuvelland waren een uitstekende uitlaatklep om bij te komen na een week werk en onze fiets en wandelvakanties in de alpen een uitstekende uitlaatklep om bij te komen van een jaar werken!

Sanne, jou wil ik tot slot in het bijzonder bedanken. Je hebt de afgelopen vier jaar op alle mogelijke manieren aan mijn promotie bijgedragen. Met je nuchtere en realistische kijk was het eenvoudig om de tegenslag, die soms ook bij een promotie hoort, te relativeren. Bovenal was het samen met jou eenvoudig om naast mijn onderzoek van de wereld en het leven te genieten!

Curriculum vitae

Joris Stegen was born on 23 May 1985 in Venray, The Netherlands. After finishing his pre-university education (gymnasium) at het Raayland College in Venray in 2003, he started studying applied physics at Eindhoven University of Technology. During his studies he conducted a research internship at San Diego State University, United States of America, in the group of Dr. Arlette Baljon where he worked on the analysis of computer simulations on the rheology of telechelic associating polymers. His Master's project was conducted under the supervision of Prof. Paul van der Schoot and in his Master's thesis he discussed a model for the scission of carbon nanotube under sonication. In 2011 he obtained his Master's degree in applied physics and started his PhD under the supervision of Prof. Paul van der Schoot and Prof. Herman Clercx in the group of Theory of Polymers and Soft matter. In 2014 he spent three months as a visiting PhD-student at Rice University, Houston, United States of America, in the group of Prof. Matteo Pasquali where he worked on a Brownian dynamics simulation for the scission of carbon nanotubes under sonication. The main results of the research performed during his PhD are presented in this thesis.